

Air Force Institute of Technology

AFIT Scholar

Theses and Dissertations

Student Graduate Works

3-2000

The Air Force Institute of Technology (AFIT) Micro Electro-Mechanical Systems (MEMS) Interferometric Gyroscope (MiG)

Jeremy P. Stringer

Follow this and additional works at: <https://scholar.afit.edu/etd>



Part of the [Electro-Mechanical Systems Commons](#)

Recommended Citation

Stringer, Jeremy P., "The Air Force Institute of Technology (AFIT) Micro Electro-Mechanical Systems (MEMS) Interferometric Gyroscope (MiG)" (2000). *Theses and Dissertations*. 4866.
<https://scholar.afit.edu/etd/4866>

This Thesis is brought to you for free and open access by the Student Graduate Works at AFIT Scholar. It has been accepted for inclusion in Theses and Dissertations by an authorized administrator of AFIT Scholar. For more information, please contact richard.mansfield@afit.edu.



**THE AIR FORCE INSTITUTE OF
TECHNOLOGY (AFIT) MICRO ELECTRO-
MECHANICAL SYSYEMS (MEMS)
INTERFEROMETRIC GYROSCOPE (MiG)**

THESIS

Jeremy P. Stringer, 2Lt, USAF

AFIT/GE/ENG/00M-18

**DEPARTMENT OF THE AIR FORCE
AIR UNIVERSITY**

AIR FORCE INSTITUTE OF TECHNOLOGY

Wright-Patterson Air Force Base, Ohio

APPROVED FOR PUBLIC RELEASE; DISTRIBUTION UNLIMITED.

20000815 170

REF ID: A70104

THE AFIT
MEMS INTEROFERRMETRIC GYROSCOPE (MIG)

THESIS

Presented to the Faculty of the Graduate School of Engineering and Management

of the Air Force Institute of Technology

In Partial Fulfillment of the

Requirements for the Degree of

Master of Science in Electrical Engineering

Jeremy Paul Stringer, B.S.E.E.

Second Lieutenant, United States Air Force

21 March 2000


Approved for public release; distribution unlimited

The views expressed in this thesis are those of the author and do not reflect the official policy or position of the Department of Defense or the U. S. Government.

THE AFIT MIG
(MEMS INTERFERROMETRIC GYROSCOPE)

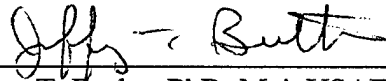
Jeremy Paul Stringer, B.S.E.E.
Second Lieutenant, United States Air Force

Approved:



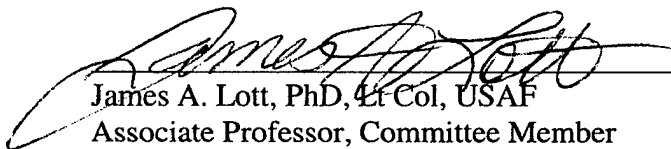
Mikel M. Miller, PhD, Lt Col, USAF
Assistant Professor, Thesis Advisor

13 Mar 00
Date



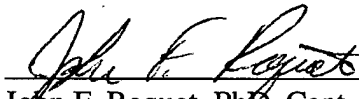
Jeffery T. Butler, PhD, Maj, USAF
Adjunct Assistant Professor, Committee Member

13 MAR 00
Date



James A. Lott, PhD, Lt Col, USAF
Associate Professor, Committee Member

13 MAR 00
Date



John F. Raquet, PhD, Capt, USAF
Assistant Professor, Committee Member

13 MAR 00
Date

Acknowledgments

First and foremost, I would like to thank God the creator of all things, omnipotent and omniscient, and not a bad guy either. Without him, I would not have even made it to AFIT, much less through AFIT.

I would like to thank Dr. Jim Leonard from AFRL Sensors Directorate, Wright-Patterson AFB, Ohio for funding my MUMPS run. I would also like to thank my thesis committee for their encouragement and guidance. Thanks also go to Maj Bill Cowan (AFRL/ML) for all the advice and help he gave me, although he had far more important things to do. Further thanks goes to Mr Bill Trop (AFIT/EN) for helping with the MUMPS devices and the SEM photographs.

My friends were also of great import. I would like to thank Phil and Kristi Corbell, and Monica Anderson for dragging me, kicking and screaming, out of my apartment on those Friday nights when I planned to do homework.

Lastly, I would like to thank PepsiCo Inc. for manufacturing the “elixir of life” which served to fuel all of my late night activities.

Jeremy P. Stringer

Table of Contents

	Page
Acknowledgments	i
List of Figures	viii
List of Tables	xii
Abstract	xiii
1. Introduction	1-1
1.1. Background	1-1
1.2. Problem Statement	1-3
1.3. Scope	1-4
1.4. Approach	1-5
1.5. Summary of Results	1-6
1.6. Overview of Thesis	1-7
1.7. Summary	1-7
2. Literature Review	2-1
2.1. Overview	2-1
2.2. Micro Electro-Mechanical Systems (MEMS)	2-2
2.2.1. Bulk Micromachining	2-2
2.2.1.1. Isotropic Etching	2-3
2.2.1.2. Anisotropic Etching	2-4

	Page
2.2.2. Surface Micromachining	2-5
2.2.2.1. Multi User MEMS Processes (MUMPS)	2-5
2.2.2.2. Lithographie, Galvanoformung Abformung (LIGA)	2-7
2.3. Inertial Sensor Development	2-8
2.3.1. Accelerometers	2-8
2.3.1.1. New Sensing and Tuning	2-9
2.3.1.2. Radiation Studies	2-12
2.3.2. Gyroscopes	2-13
2.3.3. The Prototype Integrated Optics Rotation Sensor	2-15
2.4. Multiple Sensor Integration	2-16
2.5. Inertial Navigation Systems	2-17
2.5.1. DARPA Project	2-17
2.5.2. μ SCIRAS TM	2-19
2.6. Sagnac Effect	2-20
2.6.1. Ring Laser Gyroscopes (RLG)	2-23
2.6.2. Fiber-Optic Gyroscopes (FOG)	2-23
2.6.2.1. Resonant Fiber-Optic Gyroscope (R-FOG)	2-24
2.6.2.2. The Interferometric Fiber-Optic Gyroscope (I-FOG)	2-24
2.7. Lasers	2-26
2.8. Summary	2-29

	Page
3. Theory	3-1
3.1. Sagnac Effect	3-1
3.2. Sensitivity of The AFIT MiG	3-4
3.3. Non-Reciprocal Case	3-9
3.4. Fundamental Detection Limit	3-12
3.5. Summary	3-15
4. Simulation Results and Analysis	4-1
4.1. Gyroscope Equation	4-1
4.2. Noise Level	4-3
4.2.1. Reciprocal Case	4-3
4.2.2. Non-Reciprocal Case	4-3
4.2.3. Additional Equation Terms	4-4
4.2.3.1. Additional Terms: Reciprocal Case	4-4
4.2.3.2. Additional Terms: Non-Reciprocal Case	4-6
4.3. Wavelength Dependency	4-7
4.3.1. Scale Factor Sensitivity	4-7
4.3.2. Detection Limit Sensitivity	4-10
4.4. Flight Profile Simulation	4-11

	Page
4.5. Summary	4-28
5. Proof of Concept Test Device Design	5-1
5.1. Conceptualization	5-1
5.2. MUMPS Mirrors	5-4
5.2.1. Mirror Overview	5-4
5.2.2. MUMPS Hinges	5-5
5.2.3. MUMPS Latches	5-7
5.2.4. MUMPS Mirror Plate	5-9
5.2.5. MUMPS Help Hlips	5-10
5.2.6. Final Mirror Design	5-11
5.3. MUMPS Bond Pads	5-12
5.3.1. Overview	5-12
5.3.2. Power Pad	5-13
5.3.3. Ground Pad	5-14
5.4. MUMPS Octal Mirrors	5-15
5.5. Summary	5-16
6. Prototype AFIT MiG Device Testing and Results	6-1
6.1. MUMPS Processing	6-1
6.2. Release Procedure	6-1
6.2.1. Photoresist Removal	6-1

	Page
6.2.2. Oxide Removal	6-2
6.3. Device Assembly	6-3
6.4. Hinge Failure	6-6
6.4.1. Hinge Fix 1	6-6
6.4.2. Hinge Fix 2	6-7
6.5. Device Testing	6-9
6.6. Octal Mirrors	6-11
6.7. Summary	6-12
7. Conclusions and Recommendations	7-1
7.1. Conclusions	7-1
7.2. Further Research Recommendations	7-2
7.2.1. Micromachining Techniques	7-2
7.2.2. Sensing of The AFIT MiG	7-3
7.2.3. Powering The AFIT MiG	7-4
7.2.4. Mirror Phase Shifts and Losses	7-4
Appendix A. The Sagnac Effect	A-1
Appendix B. LASERS	B-1
Appendix C AFIT MiG Equation	C-1
Appendix D. Acronym List	D-1
Bibliography	Bib-1

	Page
Vita	Vit-1

List of Figures

	Page
1. The AFIT MiG	1-6
2. Isotropic Undercutting	2-3
3. Crystallagraphic Planes	2-4
4. MUMPS Mirror	2-7
5. MIDOS Operation	2-10
6. Tunneling Accelerometer	2-11
7. MAMOS Sensing Technique	2-12
8. Sketch of Vibrating Ring Gyroscope	2-13
9. Vibratory Gyroscope	2-15
10. IORS Model No. RS-001	2-16
11. Honeywell Z axis Accelerometer	2-18
12. Sagnac Interferometer	2-22
13. Sagnac Time Propagation	2-22
14. Sketch of a Ring Laser Gyroscope	2-24
15. Interference Pattern	2-25
16. Edge Emitting Laser Geometry	2-28
17. VCSEL Geometry	2-28
18. The AFIT MiG	3-2

	Page
19. Photon Propagation	3-4
20. Circumscribed Interferometer Leg With Details	3-5
21. Clockwise Laser Path With Geometry	3-8
22. Non-Reciprocal AFIT MiG	3-10
23. Law of Diminishing Returns for the AFIT MiG	4-5
24. Law Of Diminishing Returns for the Non-Reciprocal AFIT MiG	4-8
25. Scale Factor Sensitivity To Wavelength	4-9
26. Reference Frames	4-12
27. Piezoresistive Moduation of the AFIT MiG	4-15
28. Simulated C-12 ENU Flight Profile	4-16
29. Simulated C-12 Body Rates	4-17
30. Simulated AFIT MiG C-12 Pitch Rate Output	4-18
31. Enlargement of Section of Simulated AFIT MiG C-12 Pitch Rate Output	4-19
32. Simulated AFIT MiG C-12 Roll Rate Output	4-19
33. Enlargement of Section of Simulated AFIT MiG C-12 Roll Rate Output	4-20
34. Simulated AFIT MiG C-12 Yaw Rare Output	4-21
35. Simulated Fighter Aircraft ENU Flight Profile	4-22
36. Simulated Fighter Aircraft Body Rates	4-22
37. Simulated AFIT MiG Fighter Roll Rate Output	4-23
38. Simulated AFIT MiG Fighter Pitch Rate Output	4-23

	Page
38. Simulated AFIT MiG Fighter Pitch Rate Output	4-23
39. Simulated AFIT MiG Fighter Yaw Rate Output	4-24
40. Simulated Third Profile ENU Track	4-25
41. Simulated Third Profile Aircraft Body Rates	4-26
42. Simulated AFIT MiG Third Profile Roll Rate Output	4-26
43. Simulated AFIT MiG Third Profile Pitch Rate Output	4-27
44. AFIT MUMPS 34 Layout	5-3
45. CADENCE Layout Editor	5-4
46. CADENCE Layout of MUMPS Hinge	5-6
47. Cross Section of a MUMPS Hinge	5-6
48. CADENCE Layout of MUMPS Latch Clasp	5-8
49. CADENCE Layout of MUMPS Latch Pin	5-8
50. CADENCE Layout of MUMPS Mirror Plate	5-10
51. CADENCE Layout of MUMPS Help Flip	5-11
52. CADENCE Layout of Complete MUMPS Mirror	5-11
53. CADENCE Layout of MUMPS Power Pad	5-13
54. CADENCE Layout of MUMPS Ground Pad	5-14
55. CADENCE Layout of Large Octal Mirror	5-15
56. Unassembled MUMPS Mirrors	6-4
57. Assembled MUMPS Mirrors	6-5

	Page
58. Microprobe	6-5
59. Mirror with Locking Mechanism	6-6
60. MUMPS Bond Pads	6-6
61. MUMPS Hinge Close-up	6-8
62. MUMPS Mirror With Broken Hinge	6-9
63. Hinge with Broken Bracket	6-10
64. MUMPS Mirror Sites	6-11
65. Multiple MUMPS Mirrors	6-12
66. Octal Mirrors	6-13
67. Sagnac Interferometer	A-1
68. Circular Interferometer	A-3
69. Rotated Circular Interferometer	A-3

List of Tables

	Page
1. MUMPS Layers	2-6
2. Detection Limit	4-4
3. Non-Reciprocal Detection Limit	4-6
4. Reciprocal/Non-Reciprocal Differences	4-8
5. Fundamental Detection Limit Wavelength Sensitivity	4-10
6. Release Procedures	6-3

Abstract

With the invention of Micro Electro-Mechanical Systems (MEMS) it has become possible to fabricate micro-inertial sensors. These new sensors have application in creating autonomous guided weapons systems. New technologies like Micro Unmanned Aerial Vehicles (UAVs), which cannot use conventional inertial sensors, rely on technologies like micro-inertial sensors to operate. Also, such sensors have the capability to reduce both power and space consumption on conventional aircraft. This technology is not yet mature, and current micro-inertial sensors do not have the accuracy required for highly precise navigation.

To try to increase the accuracy of micro-inertial sensors, researchers are turning toward micro-optical gyroscopes. Creating a working micro-optical gyroscope is a difficult proposition as their small size precludes micro-optical gyroscopes from having large enough path lengths to sense useful rotation rates. Techniques need to be developed to create micro-optical gyroscopes with path lengths long enough to sense navigation grade rotation rates.

This research proposes a new type of MEMS optical gyroscope. The device, called the AFIT MiG is an open loop Sagnac interferometer on a MEMS die. Mirrors are placed on the die to spiral light inward from the outside to the center of the die thereby increasing the optical pathlength of the device.

When the AFIT MiG was simulated using flight profiles generated in MATLAB™, the optical path length of the device was long enough to measure rotation rates, which were greater in strength than the noise inherent in the measurement.

This research also shows the ability to propagate light around an open loop MEMS interferometer with enough signal strength at the detector to measure.

Putting the two parts of the research together proves the feasibility of a MEMS open loop interferometer as an optical gyroscope. The impact of this research is that it creates a new way to create a micro-optical gyroscope. Further research along this topic could provide a working micro-optical gyroscope capable of providing navigation quality measurements. This micro-optical gyroscope could be mass produced and used in military and civilian navigation systems.

THE AIR FORCE INSTITUTE OF TECHNOLOGY (AFIT) MEMS
INTERFEROMETRIC GYROSCOPE (MIG)

1 Introduction

1.1. Background

The American Heritage College Dictionary defines navigate as “to follow a planned course on, across, or through.” It gives an alternate definition as “to make ones way.” Thus navigation, the process of navigating, is more than knowing where you are and where you want to be. Navigation encompasses the whole process of getting from here to there, that is, making one’s way as you follow a planned course on, across, or through.

The earliest form of navigation may well have been wandering around aimlessly until one got to where he/she was going. Fortunately, man has developed better means of navigating throughout the years. Celestial navigation (navigation using the stars) has long been a primary form of navigation. By studying the night skies, man could tell where he was and what he needed to do to get where he was going. By following a certain star, or constellation of stars, ships could track straight courses across oceans.

Once the magnetic fields of the earth were understood the compass was born. The compass gave man a better tool to guide him to his final location. Now all man had to do was to determine a course and use the compass to follow this predetermined course; a task that was much easier than following the stars.

Some uses of celestial navigation, and navigation using a compass are forms of dead reckoning. That is, one knows the direction he needs to go and approximately how far he needs to go. He then sets a heading and travels the appropriate distance in that direction,

thus navigating. For centuries, this form of navigation was “good enough.” It was accurate enough to get sailors within reasonable distances of known harbors, and land travelers within a reasonable distance of a known landmark. With the advent of the airplane, however, a more accurate form of navigation was needed. It was proven that by knowing the starting location of an aircraft and by tracking accelerations and rotations, the end position of the aircraft, to a high degree of accuracy, could be determined. To get to a known location an aviator would follow a set pattern of rotations and accelerations to end up at a specific destination.

To utilize this form of navigation, sensors had to be developed to sense the accelerations and rotations of an aircraft. The accelerometer was developed to sense accelerations and the gyroscope was developed to determine the rotations of the aircraft. In the beginning accelerometers and gyroscopes were large, bulky mechanical instruments that used a lot of power, took up a lot of space, and were not very reliable. In the 1970s two new types of gyroscopes were developed. Both new gyroscopes used lasers and the Sagnac effect to measure rotation [5, 22]. These new optical gyroscopes were more reliable, but they were still bulky and used a fair amount of power.

In parallel with the development of these new optical navigation sensors, an entirely new sensor manufacturing technology emerged. This new technology is now called Micro-Electro-Mechanical Systems and referred to simply as MEMS. MEMS is an enabling technology in that it allows for entirely new devices to be built that were not previously possible [20]. It is a way of building devices at the microscopic level that are smaller, cheaper, and faster than their macroscopic counterparts. With MEMS navigation

sensors, small portable navigation units are envisioned with many applications ranging from general civilian usage to numerous military usages [3, 14, 16].

1.2. Problem Statement

Current MEMS gyroscopes are mechanical devices that vibrate cantilever beams or polysilicate rings to sense rotation. These sensors have high sensitivity factor errors and also have large drifts. Besides the sensitivity factor errors, the actual sensitivity of the devices is limited. All this leads to gyroscopes with poor accuracy.

With the lack of accuracy in mechanical MEMS gyroscopes new alternatives need to be developed. As in the macroscopic arena, optical MEMS gyroscopes are the logical next step. MEMS optical sensors and actuators are readily constructed on semiconductor wafers [31]. The next step is to integrate the technology into a working interferometric gyroscope.

The main concern for MEMS optical gyroscopes is path length and enclosed area. The Sagnac effect, through which the gyroscopes measure rotation, is a flux integral, the larger the area the larger the flux. The Sagnac effect is further described in Appendix A. Large path lengths of up to 1 km are used for macroscopic fiber-optic gyroscopes (FOG). Such large path lengths are achieved by winding the fiber into a multiple layered coil. Ring laser gyroscopes (RLG), which use a different application of the Sagnac effect, can have path lengths of a meter or more. Some RLGs, however, have path lengths as small as 8 cm. None the less, large path lengths are not possible using silicon micro-technology. Thus if a working MEMS optical gyroscope is to be fabricated, a way to increase the path length of the device is required.

The second biggest problem with optical gyroscopes is that of optical losses. The best fiber-optic gyroscopes are still length limited by the amount of fiber loss. To develop a working MEMS optical gyroscope, methods must be developed to overcome any loss problems that may be encountered. The chief loss concern for the AFIT MiG will be light lost from multiple reflections off of multiple mirrors [7].

The problem then comes to this: to build a MEMS optical gyroscope with a path length long enough to accurately measure low rotations, while at the same time keeping losses low enough to sense any rotation at all.

1.3. Scope

This research covers the design and simulation of a MEMS interferometric gyroscope that uses MEMS mirrors on a silicon substrate to spiral the beam path length inward toward the center, creating a longer path length. The transmission medium is air and the laser beam only interacts with mirrors on the corners of the beam spiral. This design limits the contact the beam has with any dispersive medium, keeping losses to a minimum. The research also covers the design, fabrication, and testing of a MEMS interferometer. Due to the lack of a feasible manufacturing process, the test interferometer will be a scaled down version of the AFIT MiG used for modeling. The testing has been scaled down to only test the concept of moving the beam around the interferometer.

The design and simulation of the actual gyroscope was performed on MATLAB software [25]. The MEMS interferometer was designed using the CADENCE layout software [5]. CADENCE is computer aided design software used for microstructures and

is located in the Air Force Institute of Technology (AFIT) Center For Advance VLSI Research's computer network (AFIT VLSI Lab).

The CRONOS Microsystems Inc. foundry, using a process called MUMPS (Multi-User MEMS Processes), fabricated the test devices. The Air Force Research Laboratory (AFRL) Sensors Directorate, located on Wright-Patterson Air Force Base (WPAFB), Provided the laser diodes for the system.

The assembly and testing of the interferometers was done using equipment located in both the AFIT Microelectronics Laboratory (Building 125, Area B, WPAFB), and the AFIT Photonics Research Laboratory (Building 194, Area B, WPAFB).

1.4. Approach

The following research integrates the concept of MEMS with the concepts of the Interferometric Fiber-Optic Gyroscope (I-FOG). The designed gyroscope, the AFIT MiG (MEMS interferometric Gyroscope) uses a spiral pattern constructed out of MEMS mirrors to increase the path length of the device. The laser is placed on the outside of the device and the beams spiral inward to the center of the device where the interference pattern is detected, (see Figure 1). The losses are kept low by using free space as the propagating medium and using only the minimum number of mirrors required to propagate the laser around the interferometer.

The number of mirrors is kept to a minimum by using a non-circular beam path. Mirrors are only placed at the edges of the device, and then offset to spiral the beam inward towards the center of the device. As the number of mirrors grows so do the losses. The AFIT MiG can be designed to use a number of mirrors sufficient to increase the path length, but small enough to keep mirror losses within reason.

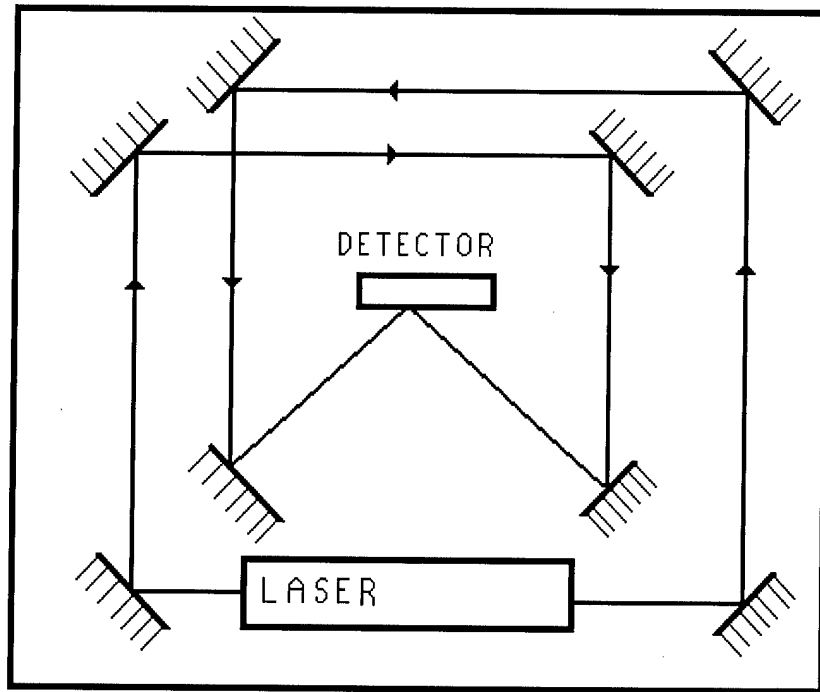


Figure 1. The AFIT MiG

1.5. Summary of Results

Through simulation using MATLAB™ [25], the AFIT MiG was shown to have an optical path length long enough to sense low rotations. The AFIT MiG was simulated for three flight profiles by measuring the roll, pitch, and yaw rates of the body frame for the different profiles. In all three cases studied the rotation rate signal level was greater than the noise of the measurement.

The concept of propagating light around an open loop MEMS interferometer was also proven. Test interferometers with a single optical leg were built and light propagated

around them. The devices were not designed to measure rotation rate but serve as a proof-of-concept for the potential AFIT MiG layout.

1.6. Overview of Thesis

Chapter 2 provides a literature review of previous MEMS research on inertial navigation devices. The review provides the different types of devices developed along with further topics of interest pertaining to those devices. Chapter 3 gives the theory behind the AFIT MiG along with a development of models to portray the device in operation. Chapter 4 gives the simulation results and analysis of the model created in Chapter 3. This chapter is devoted to different cases of operation of the AFIT MiG. Chapter 5 gives the design of an actual AFIT MiG along with the design of the test structure developed during the research. Chapter 6 gives the test procedures and the results from the tests described in chapter 5. Chapter 7 summarizes the research and provides recommendations for future research.

1.7. Summary

This research will focus on the design and simulation of a new type of interferometric gyroscope, the AFIT MiG. Theories of fiber-optic gyroscopes will be applied and adapted to this new type of optical gyroscope. This research also covers the design, fabrication, and successful testing of a test device that investigates the concept of propagating light around an open loop MEMS interferometer.

2 *Literature Review*

2.1. *Overview*

Even before there was a big push to fabricate an entire MEMS navigation system, there were many uses for MEMS inertial sensors. Micro-inertial sensors such as accelerometers have been reported in micromachining literature as far back as 1972 [31]. While micro inertial sensors have a long and venerable history, the majority of the research work has occurred within the last decade as advances in micromachining technology have allowed for better and more accurate sensors to be fabricated. The automotive industry has had the biggest affect on the advancement of micro inertial sensors [20]. For example, micro-sensors are now used extensively in airbag deployment systems and antilock brake systems. The most recent push toward the advancement of micro-inertial sensors has come from the Department of Defense in their pursuit of a low cost, miniaturized navigation and guidance system. Both Sandia National Laboratories and the Charles Draper laboratory have been actively developing low cost inertial systems [2, 3, 19, 30]. The Defense Advanced Research Projects Agency (DARPA) is currently sponsoring a competition between Litton, Intellisense, Kearfott, Honeywell, and the Charles Draper Laboratory to produce a prototype MEMS inertial navigation system (INS). Of the five designs, two will be selected during FY00 to continue development with a final selection to be made at the end of FY01 [14]. Most of the information on these systems is proprietary, and it is not available to the public.

2.2. *Micro Electro-Mechanical Systems (MEMS)*

MEMS is often confused with the development of a certain kind of device or a certain way of manufacturing devices. In reality MEMS is much more than that. MEMS is an enabling technology that allows for the fabrication of eletro-optical mechanical sensors and structures at the microscopic level. Structures from a simple etched pit to a model automobile have been fabricated [20]. MEMS originated from the semiconductor industry. As the semiconductor industry became more advanced, the industry standards changed. Minimum feature sizes went from 20 μm to 1 μm (from the 1970s to the 1990s), and the current standard is a 0.18 μm minimum feature size. At the same time the minimum feature size decreased, the wafer size increased from the 3 inch diameter wafers to 4 inch diameter with current standards using up to 12 inch diameter wafers. All of this has happened within the past twenty years. Every advancement leaves behind a large infrastructure from the previous technology. This is where MEMS comes in. Device engineers found they could use the older lithography and deposition methods to build electro-mechanical devices on silicon wafers. Not only was the overhead reduced because the infrastructure was already in place, but the devices could potentially be mass produced, meaning they could be made cheaply [20].

As the semiconductor industry used two main types of manufacturing, so did the early MEMS manufacturing processes. These two main types of manufacturing are bulk and surface micromaching. The current MEMS manufacturing processes still fall into one of these two broad categories [20].

2.2.1. *Bulk Micromachining.* Bulk micromachining involves removing silicon from the wafer; from now on referred to as the substrate. The process of removing

material from the substrate is called etching. There are different types of etches, and each uses a different type of etchant. Etches can be broken down into two different types: isotropic etches and anisotropic etches.

2.2.1.1. Isotropic Etching. Isotropic etching etches at the same rate in all directions and thus forms circular pits in the substrate. Isotropic etches are usually wet etches. They are accomplished by placing a masked substrate in a bath of acid and corresponding oxidizer for a given amount of time. The amount of time determines how deep the etch will be. Different etchants have different etch rates. The depth of the etch is controlled by precisely controlling the etch time. [20, 32]

Since isotropic etchants etch at the same rate in all directions a large amount of undercutting may occur. Undercutting is where the substrate is etched out from underneath the mask layer. Mask patterns must then be chosen accordingly to create the desired effect from the etch. The undercutting of an isotropic etch is shown in Figure 2.

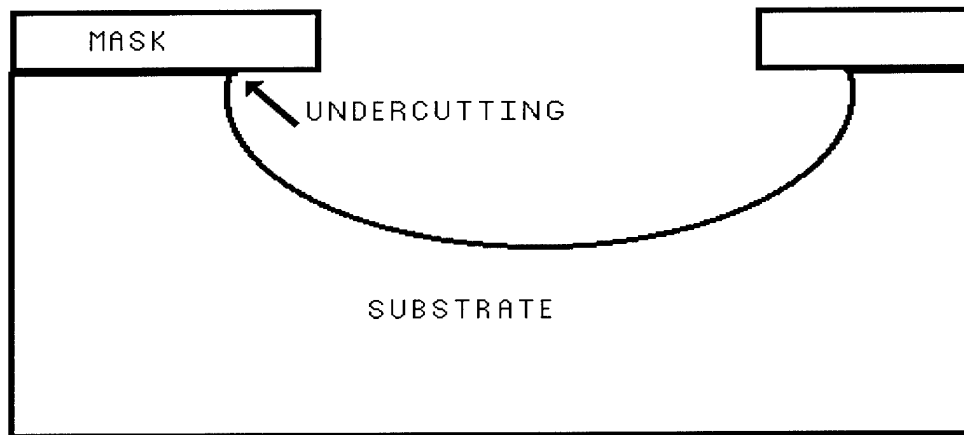


Figure 2. Isotropic Undercutting from [20]

2.2.1.2. Anisotropic Etching. Anisotropic etches etch in different directions at different rates. The differences in direction are determined by the crystalline structure of the substrate. The structure of the substrate determines different crystallographic directions upon which the atoms of the substrate crystal form. There are many different directions in a semiconductor crystal, where each direction is perpendicular to a specific crystallographic plane. Figure 3 shows some of the most common directions for a silicon substrate. The planes that correspond to these directions are perpendicular to their same numbered direction. The majority of anisotropic etches etch the slowest along the $\langle 111 \rangle$ direction and thus expose the $\{111\}$ planes. Etch ratios as high as 1:1:100 for the $\{100\}:\{110\}:\{111\}$ planes have been achieved [20].

As in the case of isotropic etches, mask placement is important. The mask must be aligned with the proper crystallographic direction or unwanted undercutting will happen. If the wafer is oriented correctly and the mask aligned correctly, it is possible to obtain nearly perpendicular sidewalls. This type of side wall

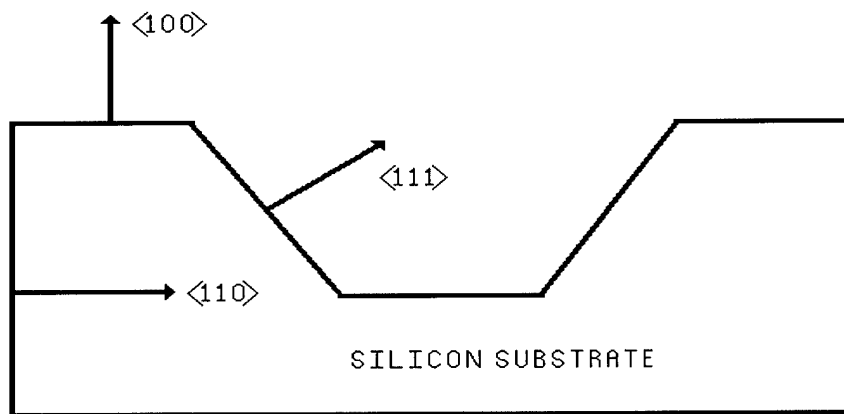


Figure 3. Crystalllographic Planes from [20]

is referred to as a vertical sidewall and is an important feature in many types of devices.

Anisotropic etches can be performed either wet or dry. There are acidic based solutions that selectively etch different crystallographic directions. Dry etches use a reactive ion plasma to etch the substrate. Such reactive ion etches are usually capable of creating near perpendicular sidewalls. The edges of the etch, however, may be rough, and this could be detrimental for some devices.

2.2.2. Surface Micromachining. The second main type of micromachining is surface micromachining. Surface micromachining involves growing layers of material on top of the substrate to form devices. Surface micromachining uses semiconductor deposition techniques such as molecular beam epitaxy (MBE), metal-organic vapor-phase epitaxy (MOVPE), and chemical vapor deposition (CVD) to deposit the materials onto the substrate [32]. In some processes, solid structures are placed on the substrate, while others use oxides as releasable layers to allow for moving structures on the substrate. Such surface micromachining processes often allow for the growth of electronic circuitry on the substrate along with the devices creating fully integrated microsystems.

2.2.2.1. Multi User MEMS Processes (MUMPS). MUMPS is a foundry process offered by CRONOS™ Microsystems [18] to users in both the academic community and industry. A standard foundry process is one where a company or a consortium of companies manufactures MEMS devices for multiple research groups or corporations. The corporation or consortium of corporations specifies standard design rules along with layer thickness and compositions for the offered process. The fabricating corporation or consortium of corporations offers the process for a nominal fee

and ships completed MEMS die to the user. For a fee of \$2900.00 (US, 1999 price) CRONOS delivers 15, 1 cm x 1 cm dice [18].

MUMPS gives two releasable polysilicon layers that can be freed from the substrate to create moving devices. The actual MUMPS process is a seven-layer process [1]. The seven layers and their respective thicknesses are shown in Table 1. The layers are all placed on a silicon substrate in the order they appear on the table; first the Nitride, then Poly0, then First Oxide, then Poly1, then Second Oxide, then Poly2, and finally a layer of gold. The releasable layers are Poly1 and Poly2. The Poly0 layer is used for electrical contacts and ground planes for capacitive devices. The nitride layer is used to keep the MEMS devices electrically isolated from the substrate. This is especially useful if electronic circuitry is to be monolithically integrated with the MUMPS devices. [18]

Table 1: MUMPS Layers

Material Layer	Thickness (μm)
Substrate	500
Nitride	0.6
Poly 0	0.5
First Oxide (sacrificial)	2.0
Poly 1 (releasable)	2.0
Second Oxide (sacrificial)	0.75
Poly 2 (releasable)	1.5
Metal	0.5

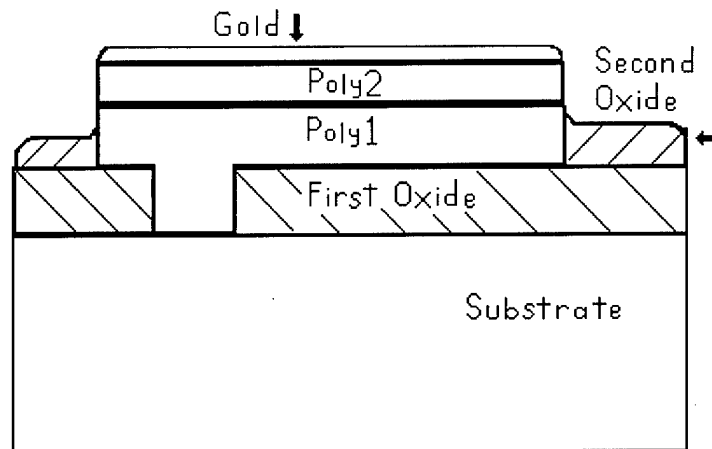


Figure 4. MUMPS Mirror

The two oxide layers, First Oxide and Second Oxide, are sacrificial layers. These two layers are etched away in a releasing etch to free the polysilicon layers. The last layer, Metal, is a thin layer of gold that increases conductivity and provides a highly reflective surface for mirrors. A cross section of a MUMPS mirror is shown in Figure 4.

2.2.2.2. Lithographie, Galvanoformung Abformung (LIGA). LIGA is another surface micromachining technique [20]. LIGA uses molding and electroplating to form high aspect ratio structures on the substrate of a MEMS device. LIGA is much like plastic injection molding. A thick layer of photoresist is placed on the substrate and patterned using a reactive ion etch to create straight perpendicular sidewalls. Metal is then electroplated onto the substrate, filling the patterned substrate. The photoresist is then lifted off leaving the freestanding structures. Electroplating is a technique that uses the substrate as an electrode and the metal source as an oppositely charged electrode. The metal moves from one electrode to the other, plating the substrate [20].

LIGA structures are free standing but are not directly releasable. Different processes can be used in conjunction with LIGA to form releasable structures. LIGA structures have rough edges from the reactive ion etching. There are currently no reliable cost-effective ways to perform LIGA, as an industrial use has not yet been found. If a viable application is found, LIGA techniques should improve.

2.3. *Inertial Sensor Development*

Initial work on micro-inertial sensors was done by different research groups. The different groups spent their time each researching a specific type of device ranging from capacitive accelerometers to vibrating ring gyroscopes. The trend was to develop a new type of gyroscope or a new type of accelerometer. Following the rush to publish a new type of device, the focus of research changed to either researching a different aspect of a design already created or creating a new method of device fabrication. One such new fabrication technique was Step Electrochemical Etching for Micro Structures (SEEMS) [27], a wet chemical etch process.

2.3.1. *Accelerometers.* Yazdi, Ayazi, and Najafi et al. have provided an overview of the different types of MEMS accelerometers and gyroscopes that have been produced [31]. Their paper discusses five different types of accelerometers and two different types of gyroscopes. The types of accelerometers are piezoresistive, capacitive, tunneling, resonant, and thermal. The different types of accelerometers are each classified by their sensing mechanism. Since their work was published in August of 1998, a new type of sensing mechanism has arisen. The new type of sensing employs Modulated Integrative Differential Optical Sensing (MIDOS) [4].

Piezoresistive devices were produced first because of their simple sensing structure, which only requires the reading of resistance from small piezoresistors on the accelerometer [31]. The majority of devices in production are capacitive devices due to their high sensitivities and simple sensing structure.

2.3.1.1. New Sensing and Tuning. The method of sensing employing MIDOS is an entirely new concept. Two photodiodes are partially covered by a proof mass. When acceleration is sensed the proof mass shifts causing a change in the amount each photodiode is covered. When the device is illuminated, the photodiodes each detect a certain amount of light. When the proof mass shifts, the amount of light each photodiode detects changes. This allows for the shift of the proof mass, and thus the acceleration, to be detected [4]. Figure 5 gives a picture of how the MIDOS detection works.

Another experimental device reported is the presetable accelerometer. In an actual operational environment, accelerometers are typically subjected to environmental noise. Under such a noise environment, the detection range of the device is limited. To overcome the noise, the accelerometer is preset. To preset the accelerometer the proof mass is physically set into a position of maximum sensitivity [29].

A single mask lateral tunneling accelerometer has been reported by Cornell University [10]. Tunneling current is current that flows across a gap between a contact and the substrate. Figure 6 shows a tunneling accelerometer. At rest a steady state current flows through the contact and into the substrate of the device. As the device accelerates, the cantilever moves either towards or away from the substrate causing a change in the tunneling current. The acceleration is determined by the change in current. In actual

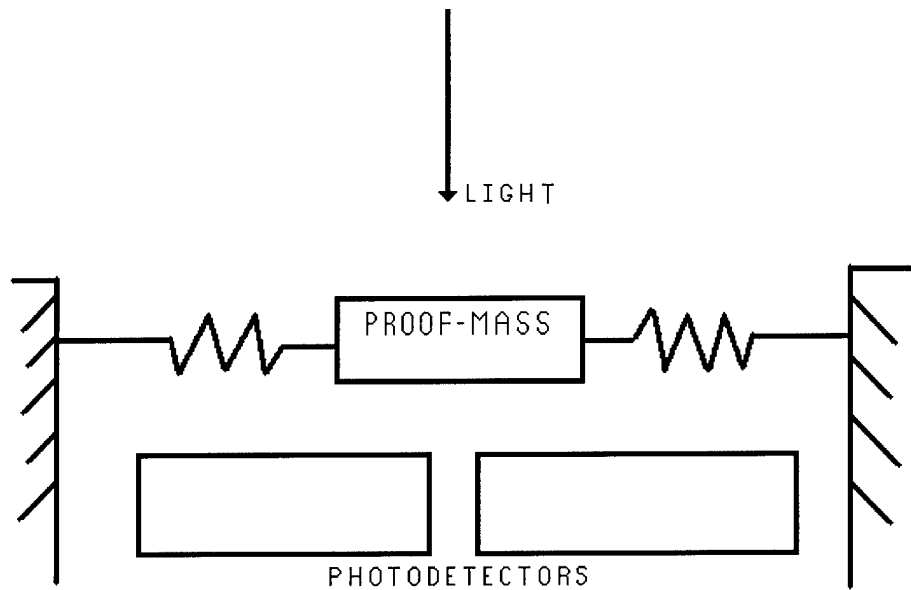


Figure 5. MIDOS Operation

operation the devices are operated in a closed loop feedback configuration. Maintaining a steady state current through actuating the cantilever does this. The voltage required to actuate the cantilever then serves as the output signal, and from it the acceleration is determined. Closed loop is the only practical means of operation for the device.

Operated in open loop large accelerations would either cause the device to short out or to become an open circuit. The extremes happen when the contact contacts the substrate or deflects too far away from the substrate.

The fact that it is a single mask step is also worth mentioning. One of the greatest expenses in MEMS manufacturing is the construction of masks. A single mask can cost over \$10k. Each additional mask not only adds cost but also adds complexity to the device as masks have to be aligned to the previous masks. A single mask step reduces both the cost and complexity of fabrication.

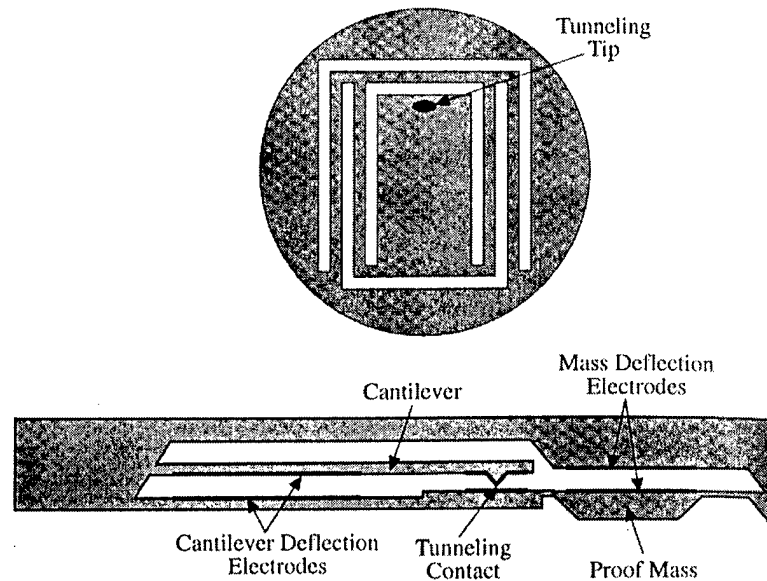


Figure 6. Tunneling Accelerometer [20]

Seoul National University reported a fully digital integrated accelerometer [31]. The accelerometer uses floating gate Metal Oxide Field Effect Transistors (MOSFETs) as the sensing device. The amount of current through MOSFETs is controlled by the voltage at the gate of the transistor [31]. Acceleration applied to the device shifts the air gap between the gate and the channel, and thus changes the voltage on the floating gate. By measuring the changing currents through the transistors the acceleration can be determined. The sensing technique is called MAMOS. Figure 7 is a sketch showing the MAMOS sensing technique

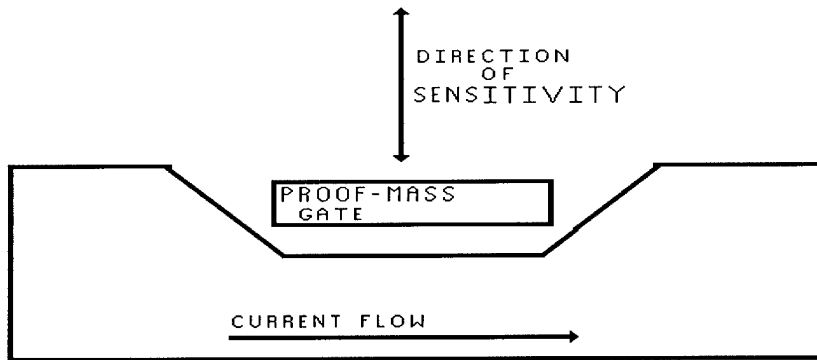


Figure 7. MAMOS Sensing Technique

2.3.1.2. Radiation Studies. Because of their small size, MEMS inertial sensors have a potential for space applications. In space, devices are subject to radiation from the sun and also gamma radiation from other objects in space. Satellites located in the Van Allen belts, or other such regions of high particle concentration, need special protection from the extra radiation. Research has been conducted on commercially available accelerometers to determine their susceptibility to different types of radiation. Studies over long-term effects of MEMS devices subjected to radiation [22] , along with studies of how any radiation affects MEMS devices have been conducted [17]. Both studies reported used devices commercially available from Analog Devices Inc. [17]. The total dose radiation study also included tests done on devices commercially available from Motorola Inc. [22].

Both studies performed indicated that commercially available MEMS accelerometers are susceptible to radiation. All accelerometers had degraded performance due to exposure to radiation [17, 22]. Results indicated that the longer the duration of the radiation the poorer performance achieved [17]. The total dose studies showed that after

a moderate amount of radiation the devices could fail [22]. The failure modes in some accelerometers turned out to be quite complex [22].

2.3.2. Gyroscopes. The literature on MEMS gyroscopes is not as rich as that on accelerometers. The majority of research in gyroscopes involved creating different types of gyroscopes or improving the types already reported. The majority of MEMS gyroscopes are vibratory in nature. The most sensitive type of MEMS gyroscope is the Ring-vibrating gyroscope. Figure 8 shows just such a gyroscope.

Different methods for fabricating such a structure have been reported in [1, 6, 8, 9, 13, 27, 29]. The main sensing technique employed is capacitively sensing the change in vibrational modes caused by the coriolis acceleration during rotation. Rotation causes a shift in the vibrational modes of objects. Ring gyroscopes can be designed so that the

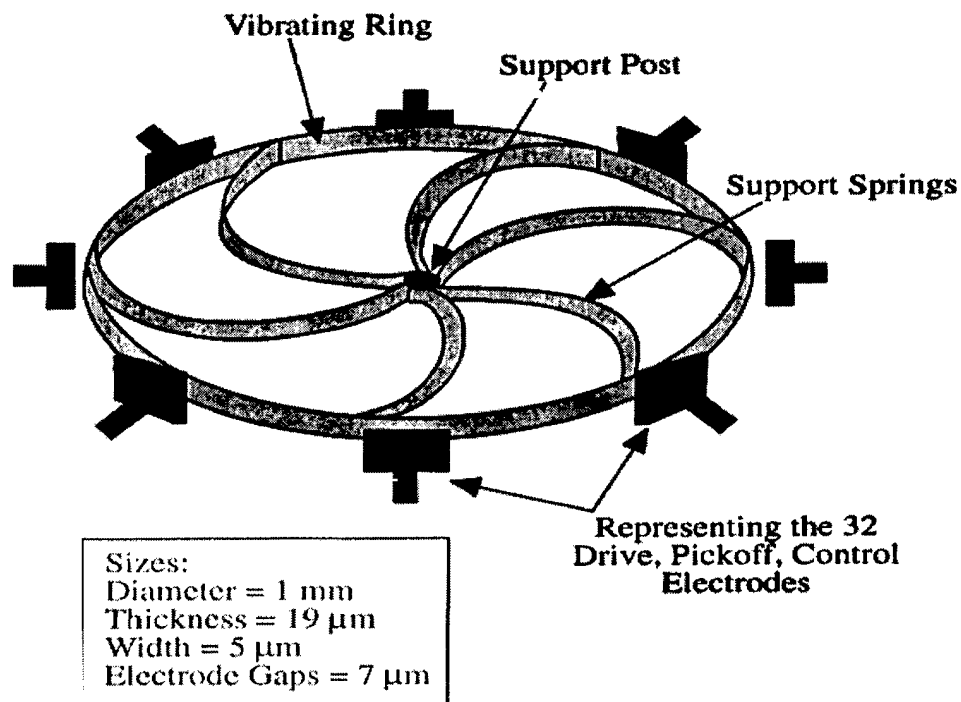


Figure 8. Sketch of Vibrating Ring Gyroscope [1]

rotational mode is exactly 45° out of phase with the non-rotational vibratory mode.

Capacitive sensing nodes are placed to sense the two modes of vibration. The amount of vibration that has been transferred to the rotational mode is a measure of how much the device has been rotated. Vibrating ring gyroscopes have been surface and bulk micromachined.

Another type of vibrating gyroscope uses the difference in vibration across a proof mass caused by the coriolis acceleration to sense the rotation. Three different types of such gyroscopes have been reported in [1, 26, 29]. The different gyroscopes employ different techniques in sensing and actuation. A joint effort by the R&D center for Samsung Electro-Mechanics, the Korea Advanced Institute of Science and Technology, and the Samsung Advanced Institute of Technology created a device that uses special fishhook shaped springs [29]. The MicroDevices Laboratory at the California Institute of Technology and the Department of Electrical Engineering at the University of California, Los Angeles created a packaged design for use in microspacecraft [31]. Samsung Advanced Institute of Technology created a tunable vibratory gyroscope design using a difference in drive and sensing direction resonant frequencies to tune the gyroscope [26]. Figure 9 is a general vibrating mass gyroscope.

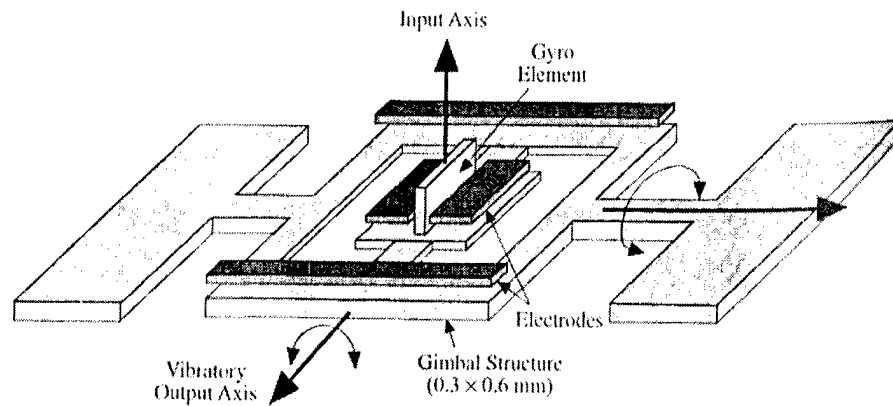


Figure 9. Vibratory Gyroscope [20]

2.3.3. The Prototype Integrated Optics Rotation Sensor. The Integrated Optics Rotation Sensor (IORS) is a DARPA funded project. The IORS is a single axis optical gyroscope. The design consists of a spiral wave-guide etched into polysilicate glass. The device is an open loop Sagnac interferometric rate sensor. The device was fabricated by Lucent Technologies using silica-on-silicon optical bench (SiOB) technology. The reported sensitivity of the device is 0.8 deg/sec [7]. The device weighs approximately 3 oz. and consumes less than 1 Watt of power [7].

Two different models of the device were reported. Model No. RS-001 uses a standard Lucent aluminum package while Model No. RS-010 uses a Kovar package. The Kovar has a lower coefficient of thermal expansion and is mechanically stiffer than the aluminum providing for a more robust package [7]. Figure 10 shows the Model No. RS-001.

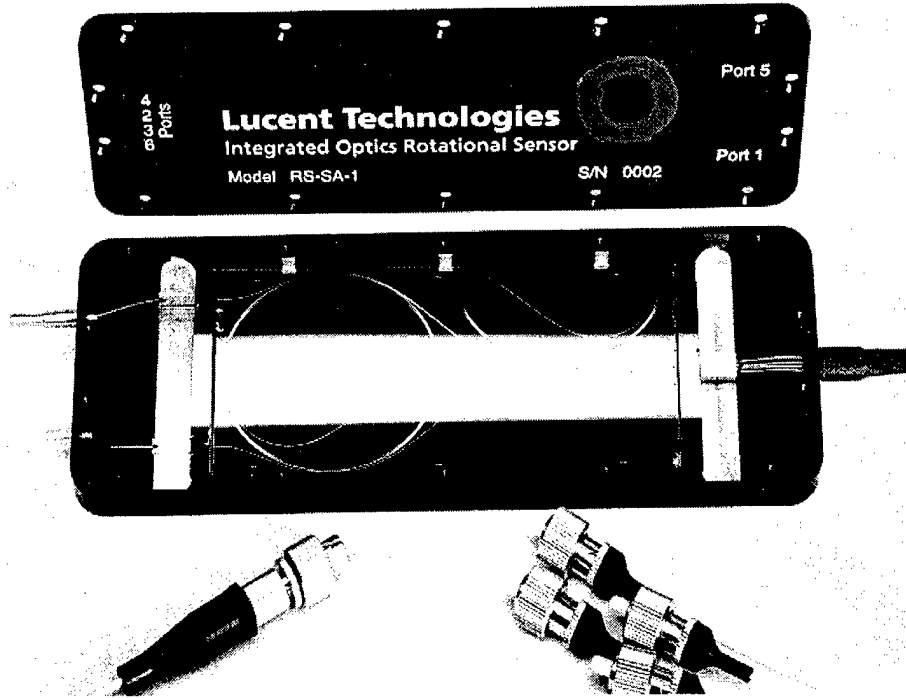


Figure 10. IORS Model No. RS-001 [6]

2.4. *Multiple Sensor Integration*

Once the difficulty in producing working sensors was overcome, the next logical step in inertial sensor technology was to integrate multiple sensors. Accelerometers were the first inertial sensors to be integrated. First, two accelerometers were placed on a single chip to form a two-degree of freedom accelerometer. Once two accelerometers were successfully integrated, the next step was to integrate a third accelerometer forming a three-degree of freedom accelerometer device. This was successfully done and commercial three degree of freedom accelerometers are available [21].

Other techniques besides using separate sensors to achieve a multiple degree of freedom accelerometer were studied. Two degree of freedom accelerometers were developed that utilized a single sensor and different sensing mechanisms to measure the acceleration data [28].

Multiple degree of freedom gyroscopes were harder to perfect than accelerometers. The major challenge faced was of planarity. The ring gyroscopes were the most accurate but they were constructed in the plane of the device with the axis of sensitivity perpendicular to the device. As such, a planar multiple degree of freedom device could not be built. The early solution was to use vibrating beam gyroscopes. Vibrating beam gyroscopes could be fabricated in plane for different sensing axes of sensitivity. It was not until the concept of one-plane devices was discarded that three degree of freedom vibrating ring gyroscopes were developed [28].

2.5. *Inertial Navigation Systems*

With the capability of fabricating multiple degree of freedom sensors, the next step was to place both accelerometers and gyroscopes onto the same device thus forming an inertial measurement unit. Three such projects are discussed below.

2.5.1. *DARPA Project.* The DARPA Sensor Technology Office (STO) is developing a less than 10 cubic inch, less than 1 Watt, 1 to 10 degrees/hr drift rate, MEMS-based system. The system will have multiple capabilities over the entire military specified temperature range of -54 to 85°C [14].

DARPA is funding four different projects. The projects include an integrated optical gyroscope by Intellisense Corporation, and three coriolis force MEMS INS approaches by Kearfott, Litton, and Honeywell [14]. It should be noted that in the Honeywell research the University of California at Berkeley is performing the design work and the Massachusetts Institute of Technology (MIT) is performing the chip fabrication [14].

The Honeywell design uses a comb drive to form a Z axis accelerometer. A Z axis accelerometer is one where the sensing direction is perpendicular to the plane of the

substrate. A comb drive is a form of capacitively sensed accelerometer. Fingers from the proof mass are interwoven with fingers from the frame. When acceleration is applied the proof mass shifts changing the capacitance sensed between the fingers. Honeywell is making the device with a high aspect ratio dry etch process. They currently plan on integrating part of the electronics on the chip [14]. The Honeywell Z axis accelerometer is shown in Figure 11.

The Litton design is a gyroscope driver stack employing a radial tooth drive. Most of the information about the radial tooth drive is proprietary and has not been disclosed. The gyroscope stack is formed from two chips that are bonded together at the central hub. The driver stack is mated to a sense unit consisting of a rate sensing element and two covers containing the pick off and torqing plates. The torsion bar in the rate-sensing element constrains the sensitivity of the device to a single input axis as desired. The unit

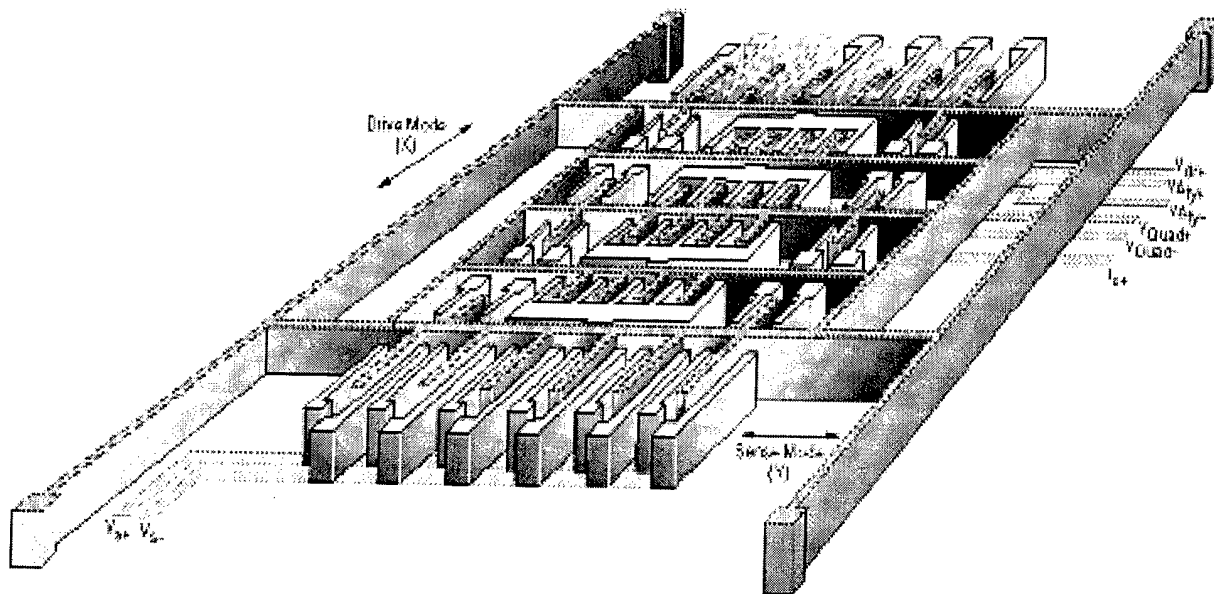


Figure 11. Honeywell Z Axis Accelerometer [12]

will be packaged with a similar element, which can be mounted in parallel for common mode rejection or at 90° to each other for a two-axes device [14].

The Intellisense design is highly proprietary and little is know about the device. Intellisense reports using integrated optics principles.

The Kearfott design is called the Miniature Vibrating Beam Multisensor. The acceleration and rotation along a single axis are measured at the same time with the same device. A resonator is used to sense the tensions imposed on the proof mass due to rotation or acceleration. The two different measurements are separated by phase between the two resonating elements. As most information about this device is also proprietary, not much else can be discerned at this time [14].

The DARPA project will reduce the number of competitors from five to two near the end of Fiscal Year 1999 or the beginning of Fiscal Year 2000. Two parallel designs will then be further developed with an expected completion near the end of Fiscal Year 2001 [14].

2.5.2. μ SCIRAS.™ The μ SCIRAS project was a development of Allied Signal Inc.. An Inertial Measurement Unit (IMU) with less than 100 deg/hr drift rate performance was reported. The μ SCIRAS Inertial Sensor Assembly (ISA) is housed in a 2 cubic inch package weighing less than 5 ounces and requires less than 0.8 Watts of power [13].

The μ SCIRAS IMU uses the same sensing elements to sense both acceleration and rotation. The device uses proof masses constrained by resonant beams. When the device is subjected to accelerations one beam goes into tension while the other beam goes into compression. This causes a difference in the resonance of the beams; this resonance shift

is a measure of the acceleration. The same resonant beams are used to sense the vibrational changes due to the coriolis acceleration caused by rotation [13]. The paper states that the devices, when properly packaged, have the capability to withstand 20,000 g shock loads along the accelerometer-input axes. The IMU is fabricated in a batch process from one piece of crystalline silicon [13]. More information on specific types of micromachining is provided later in this chapter.

The ISA is composed of only eleven parts. The eleven parts consist of three sensors and the housing and sense circuitry. The three sensors are mounted in what [13] refers to as a “cube-on-corner” triad. The three sensors are each mounted with an angle of 35.26° with respect to the horizontal plane for each of the rate axes. This forms an orthogonal triad with minimal volume consumption. The accelerometer axes lie along the faces of the three sensors forming an acute skewed relation. Each of the axes is 35.26° from the common vertical axis. The accelerometer axes are easily transformed to be co-located with the rate axes using a mathematical algorithm [13].

The sensors are housed within a magnetic grade stainless steel can. The device is sealed in a dry nitrogen gas environment to prevent moisture condensation at low temperatures. The can not only protects the sensors physically but also acts as a shield against both electric and magnetic fields. The final sensor has been centrifuged up to 15,000 g's and still found to function. All of the package elements were designed to withstand 20,000 g's along the central vertical axis [13].

2.6. Sagnac Effect

The Sagnac effect was discovered in 1913 by Sagnac [22]. Rotation in inertial space causes a path length difference between two counter rotating light beams in a Sagnac

interferometer, as shown in Figure 12. The actual Sagnac equation shows that the Sagnac effect is actually the flux of the rotation vector through the path enclosed by the ring interferometer [22]. The Sagnac equation is:

$$\Delta\phi_R = \frac{4\omega}{c^2} \vec{A} \cdot \vec{\Omega} \quad (\text{rad}) \quad (1)$$

where $\Delta\phi_R$ is the phase shift caused by the rotation vector Ω . \vec{A} is the area vector for the interferometer. The speed of light is c , and ω is the frequency of the light used in radians.

The Sagnac effect can be better understood by looking at Figure 13. Figure 13 shows a ring interferometer at time t_0 and then again at time t_1 . At time t_1 the interferometer has shifted in space. Point p_1 has moved and so it takes a light beam propagating in the clockwise direction less time to reach point p_1 than it would at time t_0 . In the same manner it takes the beam traveling in the counterclockwise direction more time to reach point p_1 than it would at time t_0 . This time difference is equivalent to a path length difference in the two counter propagating beams.

When the beams reach the detector in Figure 12, they interfere, forming an interference pattern. The interference pattern is given by the equation below [11]:

$$I = I_1 + I_2 + 2\sqrt{I_1 I_2} \cos \Delta\phi \quad (\text{Watts/cm}^2) \quad (2)$$

This equation is a raised cosine where the $\Delta\phi$ term is the phase difference between the two beams. The first two terms (I_1 and I_2), are the intensities of the counter propagating beams. In the Sagnac interferometer the two beams travel reciprocal paths and so, in the

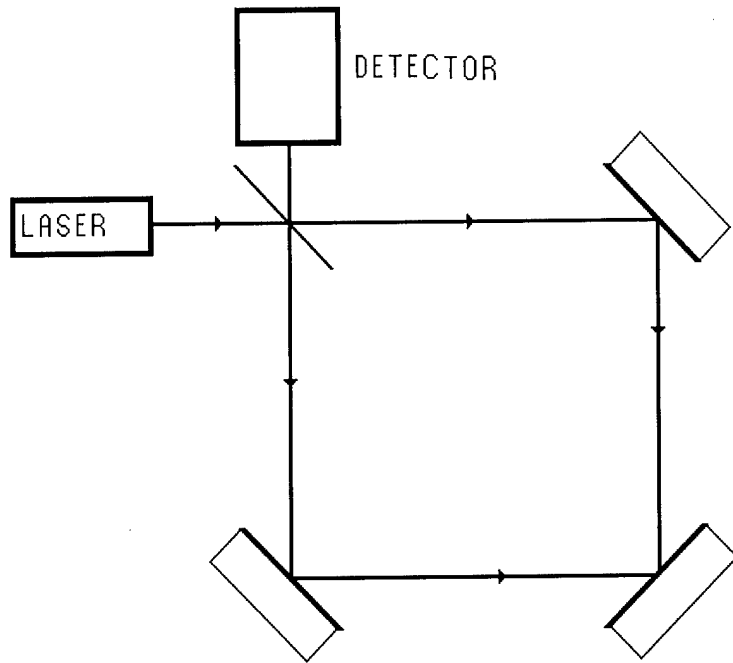


Figure 12. Sagnac Interferometer after [22]

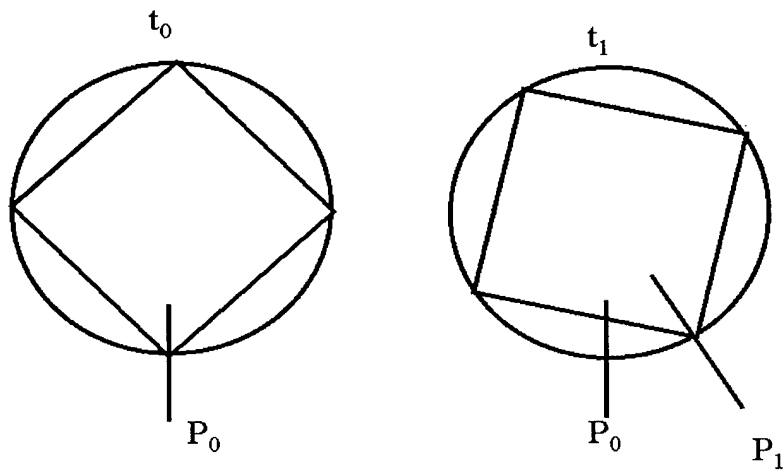


Figure 13. Sagnac Time Propagation from [22]

presence of no rotation, interfere with zero phase difference at the detector. As one travels in either direction from the detector, a phase difference occurs. With zero phase difference the interference pattern is at a maximum. As the phase difference increases the resultant intensity (I) decreases until the two beams are 180° out of phase, at which time the intensity is a minimum.

As previously noted, a rotation causes a path length difference that in turn causes a phase difference at the detector. Optical gyroscopes sense this phase difference. This phase difference is used to determine the time and path length difference that caused the rotation. This difference is used to determine the distance that the gyroscope has rotated. There are two main types of optical gyroscopes. Both use a different implementation of the Sagnac effect to determine the requisite rotation information. The two different types are ring laser gyroscopes and fiber optic gyroscopes.

2.6.1. Ring Laser Gyroscopes (RLG). Ring laser gyroscopes use a ring shaped resonant cavity that is equal to an integer number of wavelengths of the laser emissions. The counter rotating waves interfere and form a standing wave pattern. As the device rotates the standing wave pattern stays fixed in inertial space and the ring cavity rotates around the standing wave. This is equivalent to a path difference causing a shift in the interference pattern discussed previously. A photodetector is used to measure the interference pattern. The photodetector is fixed to the resonant cavity and so rotates in inertial space (see Figure 14). As the photodetector rotates it passes by minimums and maximums in the standing wave. The rotation information is extracted by counting this beat frequency. The total number of beats can be counted to determine the total rotation to a given point.

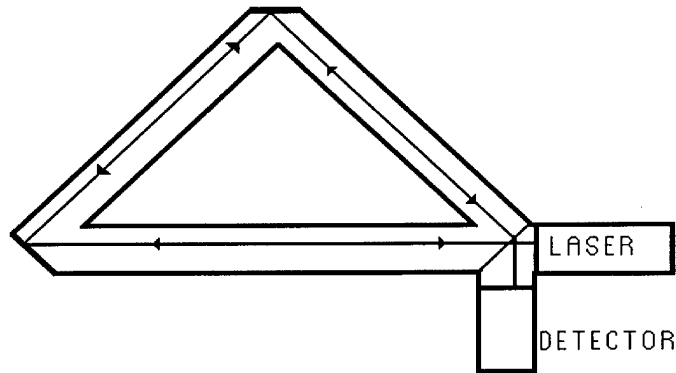


Figure 14. Sketch of a Ring Laser Gyroscope [19]

2.6.2. Fiber-Optic Gyroscopes (FOG).

2.6.2.1. Resonant Fiber-Optic Gyroscope (R-FOG). The R-FOG is similar to the RLG in its method of detection. In the R-FOG counter rotating laser beams are introduced into an optical fiber where the optical fiber is equal in length to an integer number of laser wavelengths. As such a standing wave pattern is formed in the fiber. The standing wave pattern is picked-off the fiber and the beat frequency again gives the required rotation information.

2.6.2.2. The Interferometric Fiber-Optic Gyroscope (I-FOG). The I-FOG senses a direct change in the interference pattern given by the Sagnac effect. The I-FOG uses a multi-turn coil to enhance the Sagnac effect. The increase in measurement is equivalent to the increase in magnetic flux achieved when a multi-turn inductor is used.

The interference pattern in Figure 15 shows that with no bias the interference pattern

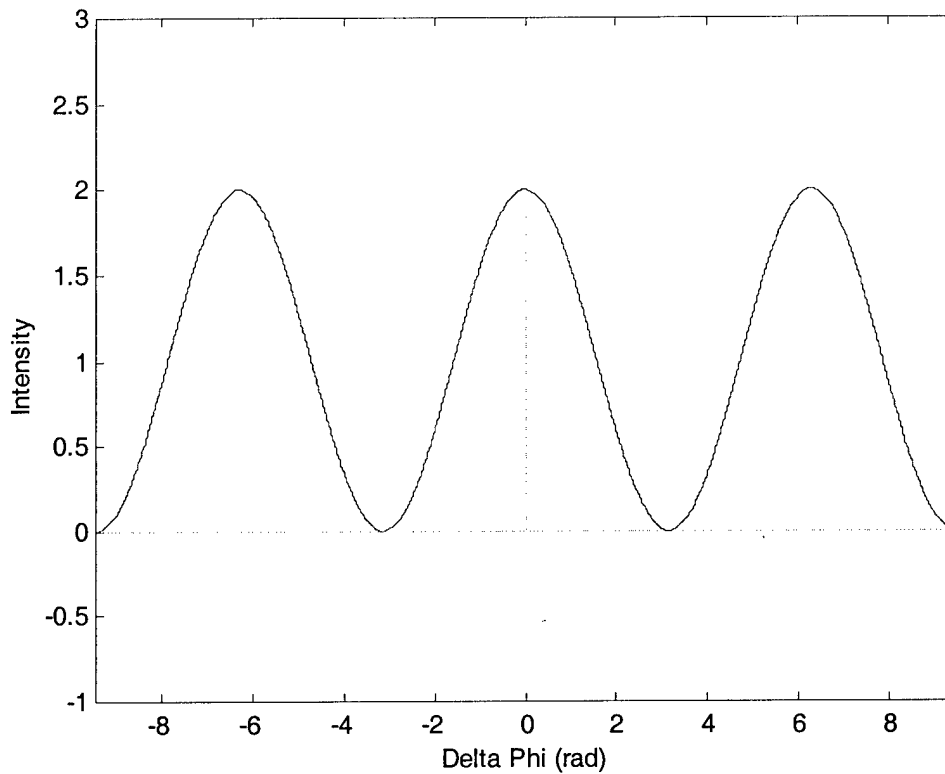


Figure 15. General Interference Pattern

is a maximum as expected. When the interferometer is rotated the intensity at the detector shifts left or right on the curve depending upon the direction of rotation. As the detector only senses the change in intensity it can not be determined which direction the interferometer is moving. In addition, at the maximum, the scale factor is non-linear, meaning it takes a large change in Ω , the rotation rate, to get a small change in ϕ , the phased difference. To ensure as linear a scale factor as possible, the gyroscope is operated at the point of inflection of the raised cosine. At the point of inflection the slope of the curve is maximum and the curve is at its most linear point. The point of inflection occurs at a ϕ , corresponding to a phase difference of $\pi/2$. To maintain operation at the point of inflection, the gyroscope is biased at a phase difference of $\pi/2$. At the $\pi/2$ bias

point the direction of change is determined by whether the intensity increases or decreases. The scale factor is also linear at this point with a large slope, so a small change in Ω causes a large change in ϕ , so that small rotations can be measured. The gyroscope is then operated over a region of 0 to Ω rotation rate, where a Ω rotation rate coincides with the first minimum on the interference curve.

This small range of operation, where ϕ ranges from 0 to π is in practice not that constricting. The length of the fiber coil determines the size of the operating region. The fiber length can be made any length within reason to give a large enough operation region. This flexibility of design is a big plus when using FOGs [6].

2.7. *Semiconductor Lasers*

LASER is an acronym that stands for Light Amplification by Stimulated Emission of Radiation. Laser light is used in optical gyroscopes because it is coherent light. Coherent light is light that is monochromatic, in phase, and propagates as a unified phase front. In order for an optical gyroscope to operate the light has to be coherent. If the light is continuously shifting phases it will form an interference pattern in the light detector. This phase shift will be indistinguishable from any such shift caused by a rotation. A single wavelength is important for the same reasons. If multiple wavelengths are present, they will propagate through the transmission medium at different speeds. The waves will then interfere when they combine at the detector, forming an interference pattern.

In truth, no laser is truly monochromatic or completely in phase. There is a small range of wavelengths over which any laser operates. As for coherence, lasers are coherent only for a given time, then they may shift properties, but once they shift they

will maintain these properties for a time period before changing again [12]. Because the laser emits coherent light for a given period of time, rotation can be determined during this time period. High quality lasers have long periods of coherence with only short periods of non-coherence. These high quality lasers allow optical gyroscopes to be constructed.

It is also important that the lasers used in optical gyroscopes have a low divergence output beam. In all lasers the beam begins to disperse as it propagates in space. At a long distance from the laser the beam width is very large and there is not a large amount of power present at any location. In the case of optical gyroscopes the divergence of the beam needs to be kept low so that as much power as possible is present at the detector. For the AFIT MiG this will be especially important, as the medium of propagation is free space. In fiber gyroscopes and in RLGs the surrounding medium keeps the beam contained, in the AFIT MiG there is no such luxury. Also, some power will be lost at the mirrors. In order to reflect as much power as possible off of each mirror the beam needs to be as small as possible. More power impinging on the mirror means more power reflecting.

There are two different types of semiconductor lasers each with their own characteristics. Vertical Cavity Surface Emitting Lasers (VCSEL) and edge emitting lasers. Vertical cavity lasers use Distributed Bragg Reflectors and the light is emitted from the surface of the laser. Edge emitters used cleaved mirrors and the light is emitted from the edge of the device. VCSELs have more circular beams and consequently lower dispersion and would thus be the choice for the AFIT MiG. VCSELs however are difficult to mount and thus add complexity to the device. Edge emitting lasers have

elliptical beams and higher dispersion. Because the light is emitted from the edge, however, they are easy to mount on the device and get the light to travel in the plane of the substrate. For this reason edge emitters are used on the interferometer reported in this thesis. Figure 16 and Figure 17 show schematics of an edge emitting laser and a VCSEL, respectively. For further information on the operation of Lasers see Appendix B.

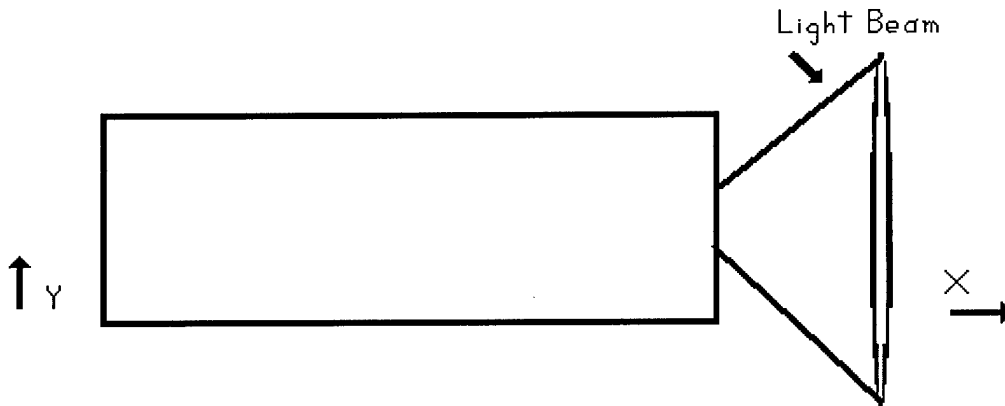


Figure 16. Edge Emitting Laser Geometry

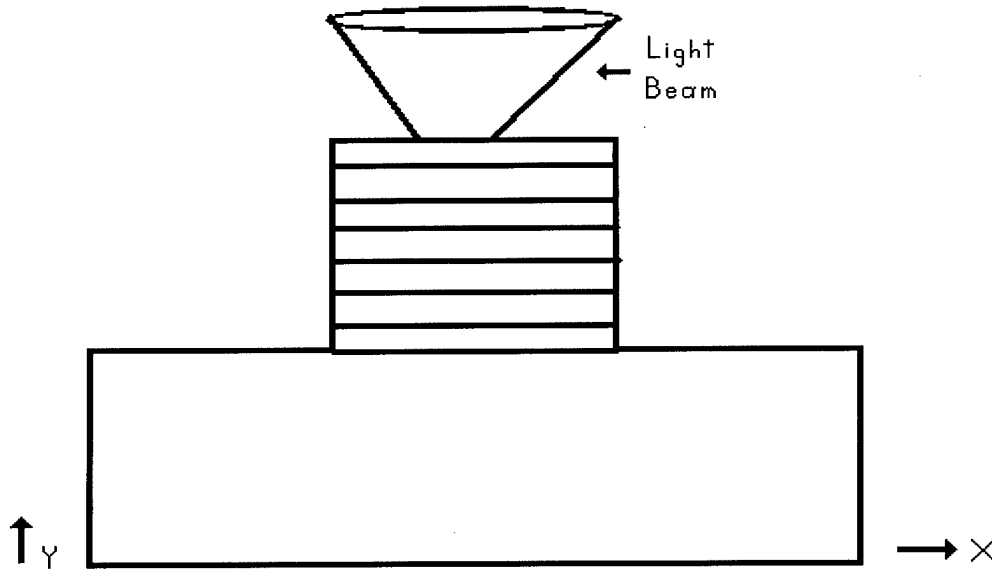


Figure 17. VCSEL Geometry

2.8. *Summary*

This chapter has given a brief overview of the technologies used to develop the AFIT MiG theory. Both the Sagnac effect, the principles by which optical gyroscopes operate, and micromanufacturing techniques were discussed. After the concepts of micromanufacturing were presented, an overview of the different types of MEMS inertial sensors and further work in the area was presented. This overview covered both simple single degree of freedom devices up to complete IMU triads capable of being used in an INS. A brief theory of laser devices was also presented to familiarize the reader with such devices.

Chapter three uses the Sagnac effect and the configuration of the AFIT MiG to develop the scale factor for the AFIT MiG. Along with theory for the scale factor, theory behind the performance limits of the AFIT MiG is also presented.

3. Theory

3.1. Sagnac Effect

The theory for the operation of the AFIT MiG parallels the theory of the I-FOG. The actual implementations, however, are different and so the I-FOG Theory is used only as a starting point for the development of the AFIT MiG equations. The Sagnac equation for the I-Fog is [22]:

$$\Delta\phi = \frac{2\pi LD}{\lambda c} \cdot \Omega \quad (\text{rad}) \quad (3)$$

In this equation the phase difference $\Delta\phi$ formed by the interference of the counter rotation beams during rotation is given as a function of the length (L) and diameter (D) of a circular fiber. The equation holds normally, as the majority of I-FOGs in-use are circularly wound gyroscopes. The parameters for this equation are listed below.

L - Length of the fiber in m

D - Diameter of the fiber path in m

λ - Wavelength of the light used in m

c - Speed of light in a vacuum in m/s

Ω - Rotation vector in rad/s

$\Delta\phi$ - Phase shift due to rotation in rad

Recalling the AFIT MiG design re-shown in Figure 18, the AFIT MiG is not a circular design and so Equation (3) cannot properly determine the phase difference due to the rotation of the device. In fact the laser path of the AFIT MiG spirals inward toward the

center of the device. Because of this there is not a constant diameter, or in the more general case of a non-circular device, a constant perimeter. Based on these circumstances it is more appropriate to determine the operation of the AFIT MiG based only on path length and not on the geometry of the path.

As stated in Chapter 2 the rotation of the interferometer causes a path length change for a laser beam traversing the interferometer. The sign of this change, positive or negative, is dependent upon the direction in which the beam is traversing the interferometer. These path length changes correspond to changes in the propagation times of the laser beams, which leads to a phase difference when the counter rotating laser beams interfere. Considering each part of the path and summing the results should

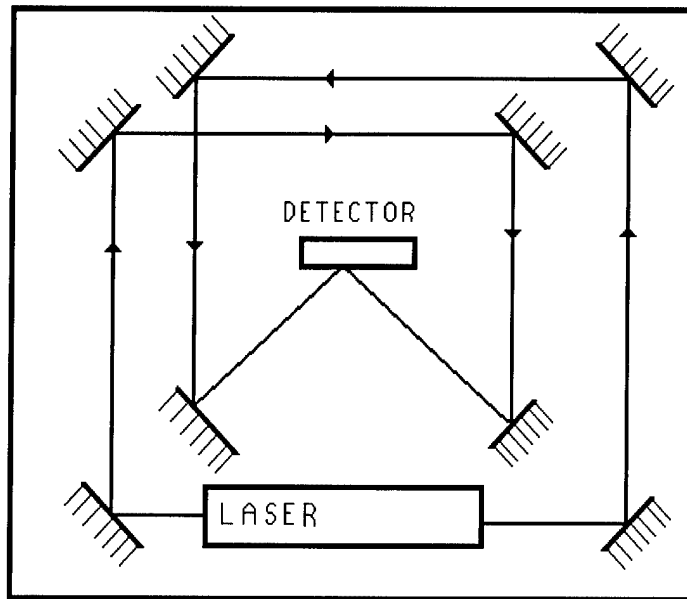


Figure 18. The AFIT MiG

provide for a solution independent of path geometry. The time difference for each part of the path will be determined and summed, and then converted to a phase difference.

To better understand this, consider one photon as it traverses the interferometer in the counterclockwise direction. This photon is marked in Figure 19. As the photon traverses path leg A also in the figure, the path leg is moving in the same direction. To the photon traveling down the leg the leg appears to have grown longer. By the time the photon has traversed the entire leg, the leg now appears as leg B. If the path leg were not moving, the photon would only have to travel to point 1, now, however, the photon has to travel to point 2. The increase in distance is length ℓ , between the two points. Each leg of the interferometer will cause this same path length change. Each of these path length changes will add time to the travel time of the interferometer. By the time the photon reaches the point where it started, or the collector, it will have amassed a net rotation time difference with respect to a stationary interferometer. Photons traversing the clockwise direction will experience a similar time shift, only of the opposite magnitude. When both counter rotating beams arrive at the collector, they have amassed a total time difference between the two beams equal to the sum of the time differences for the two separate directions.

Because the light traversing the interferometer is a wave, the intensity of the light at a particular point in space is a function of time. If the interferometer were not subjected to a rotation there would not be a time shift for either beam with respect to the other beam. The waves reaching the detector would be at a constant phase and would then give a constant intensity. If, however, the interferometer were subjected to a rotation, the beams

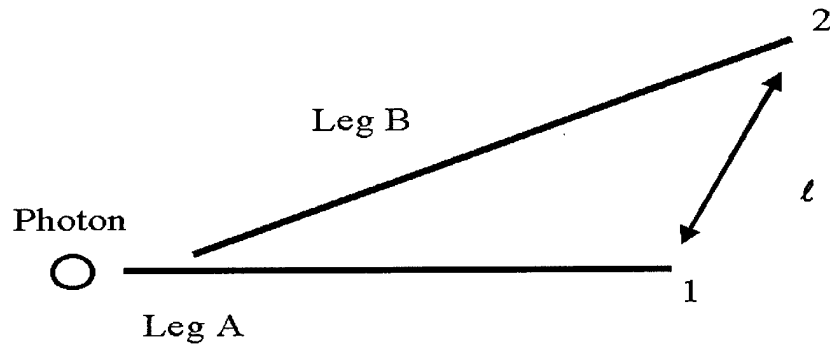


Figure 19. Photon Propagation

would shift in time with respect to each other, and when they interfere they would each have a phase at the collector that was different from the stationary case. The intensity at the detector would then also be different from the stationary case. If the rotation of the interferometer changed, the time difference would change, and thus the phase difference and intensity would also change. Measurement of this intensity change is, in fact, how the rotation information is collected from an interferometric gyroscope.

Turning back to the AFIT MiG, each leg of the AFIT MiG causes a time difference when the interferometer is rotating. To find the time difference for the entire interferometer, the time difference for each leg is first found. These time differences are summed up and converted to a corresponding phase difference. This phase difference then determines how the two counter rotating beams interfere, and thus the intensity of the interfering laser beams at the collector.

3.2. Sensitivity of The AFIT MiG

In developing equations to determine the time shift and thus phase difference caused by each leg, concentrate first on a random interferometer leg. The goal is to develop an

equation based on the length of the interferometer leg. Once such an equation is found, it can be applied to each leg in the interferometer, each component summed, and the final phase difference calculated. Figure 20 shows one leg of the interferometer circumscribed about the center of rotation of the interferometer. The location of the leg in the interferometer is not important. The derived equation will be valid for all legs in the interferometer, regardless of location. Now consider a photon located at point A. While the interferometer is at rest, the photon only has to travel to point B to exit the interferometer. A photon originating at B would only have to travel to A and there would be no difference in the propagation times of the two photons. If the interferometer is rotating, point B is also moving. While the photon is traversing the interferometer leg, the leg is moving, and by the time the photon exits the interferometer leg in the figure, Point B has move to Point C. Thus to exit the interferometer the photon had to travel a longer distance than for the stationary interferometer. Because the photon is traveling at

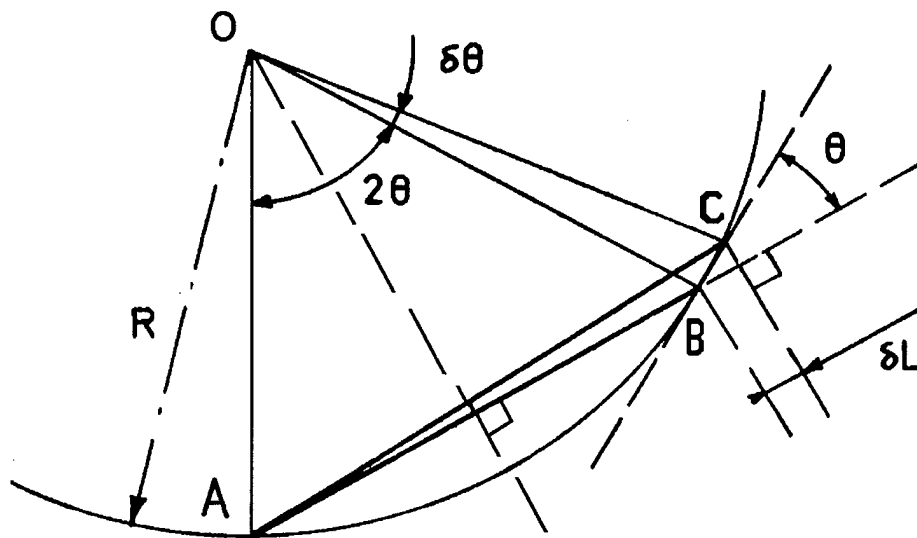


Figure 20 Circumscribed Interferometer Leg With Details [22]

the speed of light, the time it takes to traverse the interferometer leg is short, and the interferometer rotates through only a very small angle $\delta\theta$. Applying the small angle theorem, the extra distance the photon has to travel can be approximated by δL . The time it takes the photon to travel δL is given by $\delta L/c$. This time is the required time difference. So solving for the time difference reduces to finding the path length change δL . It is important to remember at this point that this length change δL must be found as an equation of the rotation rate. In Figure 20 the rotation rate causes the interferometer leg to sweep out angle $\delta\theta$. The distance δL is related to the rotation rate of the device through this angle.

Length δL is solved for with respect to the angle $\delta\theta$ using trigonometric relationships. The rotation of the interferometer sweeps out a differential angle increase $\delta\theta$ shown in Figure 20. The length BC can then be found using:

$$BC = R\delta\theta \quad (\text{meters}) \quad (4)$$

where BC is the length of the leg from B to C in the figure and R is the radius from the center of rotation of the interferometer to points A, B, and C. This solution is based on the fact that the arc an angle sweeps out is equal to the radius multiplied by the angle swept out. In the case of Figure 20 the angle is small enough that the arc can be considered a straight line, and so the length BC is approximated by the length of the arc swept out by $\delta\theta$. Then, using rules of geometry and trigonometry:

$$\delta L = BC \cos \theta \quad (\text{meters}) \quad (5)$$

where δL and BC are as previously described. The angle θ is also shown in Figure 20 and is determined from the angle 2θ , along with the rules of right triangles.

The relationship of Equation (5) must now be related to the rotation of the interferometer. The rotation angle $\delta\theta$ is to first order the angle of rotation during the propagation of the light beam [22]. Because the length of the interferometer is known this angle becomes:

$$\delta\theta = \frac{L}{c} \cdot \Omega \quad (\text{rad}) \quad (6)$$

With this relationship the connection between $\delta\theta$ and δL is made using substitutions.

Equation (4) is first substituted into Equation (5) giving:

$$\delta L = R\delta\theta \cos\theta \quad (\text{meters}) \quad (7)$$

Then Equation (6) is substituted into Equation (7) giving:

$$\delta L = \frac{L}{c} R \cos\theta \cdot \Omega \quad (\text{meters}) \quad (8)$$

This is the desired after relationship giving the increased distance the photon must cover, δL , as a function of the rotation rate of the interferometer.

The time change for the given leg of the device is determined using this relationship as:

$$\delta t = \frac{\delta L}{c} = \frac{LR \cos\theta}{c^2} \cdot \Omega \quad (\text{sec}) \quad (9)$$

Applying this relationship to each leg of the interferometer for the clockwise path of Figure 21 the time difference becomes:

$$\begin{aligned} \delta t_{cw} = & [L_1 R_1 \cos\theta_1 + L_2 R_1 \cos\theta_2 + L_3 R_2 \cos\theta_3 + L_4 R_2 \cos\theta_4 + L_5 R_3 \cos\theta_5 \\ & + L_6 R_3 \cos\theta_6 + L_7 R_4 \cos\theta_7 + L_8 R_4 \cos\theta_8 + L_9 R_5 \cos\theta_9] \frac{\Omega}{c^2} \quad (\text{sec}) \quad (10) \end{aligned}$$

Where L_1 through L_9 , θ_1 through θ_9 , and R_1 through R_9 are as given in Figure 21. The figure contains eighteen legs. Each leg and thus the associated radius and angle is independent of the other legs. This allows the equations developed to be applied to interferometers of different geometric shapes. It is dependent only upon the lengths of the optical legs and not upon how they are arranged. To make the equations derived simpler only nine of the legs are used in the derivation. Also, to keep Figure 21 from being too cluttered only two of the radii and angles are shown. The other radii and angles can be inferred from how R_1 , R_2 , θ_1 , and θ_2 are described. All other parameters are as previously given. The term δt_{ccw} is the same in form but opposite in sign of Equation (10). This form of the equation was chosen because it is the most general. Certain terms could be grouped and a simplification found, however, that simplification would not be applicable to different geometries as the given implementation is.

The time difference for the interferometer is the difference between the clockwise beam propagation time and the counterclockwise beam propagation time. These times are: $t_{cw} = t + \delta t_{cw}$ and $t_{ccw} = t - \delta t_{ccw}$. These times are based on the assumption that the interferometer is rotating in the clockwise direction. If the interferometer is rotating in the counterclockwise direction the signs of the two terms are changed and the results of Equation (10) remain true. The preceding terms are also based on the assumption that the two paths of the interferometer are the same length and reciprocal. This assumption is used during simplification while deriving the equations. In the next section this assumption is removed and the equations are re-derived. Under any circumstance the time difference between the counter rotating paths is the difference between the two

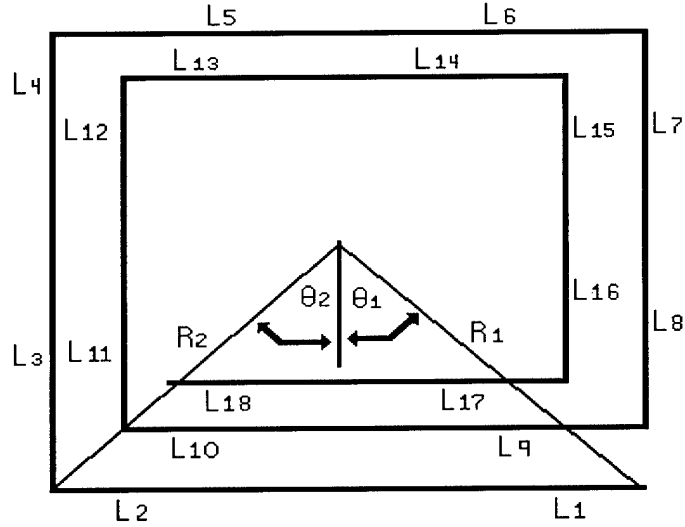


Figure 21 Clockwise Laser Path With Geometry

times. Subtracting the two times gives:

$$\Delta t = t_{cw} - t_{ccw} = \delta t_{cw} + \delta t_{ccw} \quad (\text{sec}) \quad (11)$$

When the two paths are reciprocal as has been assumed than this further reduces to:

$$\Delta t_{recip} = 2\delta t_{cw} \quad (\text{sec}) \quad (12)$$

This time difference is converted to the equivalent phase difference by:

$$\Delta \phi_{recip} = \omega \cdot \Delta t_{recip} \quad (\text{rad}) \quad (13)$$

where ω is the radian frequency of the laser light used. This phase difference, as previously described, causes the intensity changes in the interferometer as the interferometer rotates.

3.3. *Non-Reciprocal Case*

Up to this point it has been assumed that the interferometer has perfect reciprocity.

With the true AFIT MiG, however, this is not the case. In order to get the laser beam to

traverse the interferometer the beam paths are slightly offset. The question is then; how does this non-reciprocity effect the performance of the interferometer.

For the case of non-reciprocity the general form of the time difference equation, Equation 10, does not change. This equation will again be applied to each leg of the interferometer. The differences come in how the final time equation falls out of this application. To facilitate this development, consider again Figure 21. What will change in this figure is both the direction the light propagates, to form the counterclockwise path, and the lengths of the legs L_1 through L_{18} . To create the different length legs a differential distance δL is added to each leg. This difference is different from the δL used to determine Equation (10). Adding these differential distances also causes the radii and

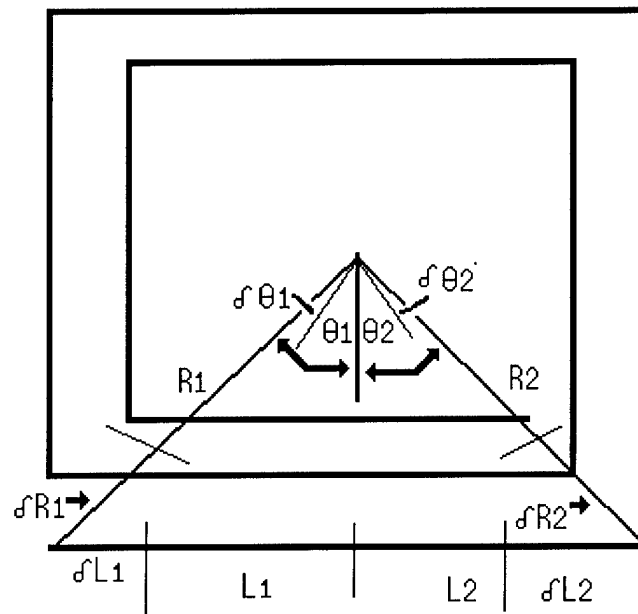


Figure 22. Non-Reciprocal AFIT MiG

angles to change by differential amounts δR and $\delta\theta$. Applying these differential changes to the first two legs in Figure 21 gives Figure 22. Then using Figure 22 to apply the differences to each leg the time difference for the counterclockwise direction becomes:

$$\begin{aligned} \delta t_{ccw} = & [(L_1 + \delta L_1)(R_1 + \delta R_1)\cos(\theta_1 + \delta\theta_1) + (L_2 + \delta L_2)(R_1 + \delta R_1)\cos(\theta_2 + \delta\theta_2) \\ & + (L_3 + \delta L_3)(R_2 + \delta R_2)\cos(\theta_3 + \delta\theta_3) + (L_4 + \delta L_4)(R_2 + \delta R_2)\cos(\theta_4 + \delta\theta_4) \\ & + (L_5 + \delta L_5)(R_3 + \delta R_3)\cos(\theta_5 + \delta\theta_5) + (L_6 + \delta L_6)(R_3 + \delta R_3)\cos(\theta_6 + \delta\theta_6) \quad \text{sec} \\ & + (L_7 + \delta L_7)(R_4 + \delta R_4)\cos(\theta_7 + \delta\theta_7) + (L_8 + \delta L_8)(R_4 + \delta R_4)\cos(\theta_8 + \delta\theta_8) \\ & + (L_9 + \delta L_9)(R_5 + \delta R_5)\cos(\theta_9 + \delta\theta_9)] \frac{\Omega}{c^2} \end{aligned} \quad (14)$$

where the parameters L_1 through L_9 , δL_1 through δL_9 , R_1 through R_5 , δR_1 through δR_5 , θ_1 through θ_9 , and $\delta\theta_1$ through $\delta\theta_9$ are as shown in Figure 22. Again, to keep Figure 22 from being cluttered information is only shown for two of the legs and the information for further legs can easily be inferred from how the first two legs are defined. All other parameters are as seen before.

When the terms of Equation (14) are expanded and collected the equation becomes large and is not easy to examine. However, if the trigonometric identity of Equation (15) and the small angle approximation are used Equation (16) is the end result.

$$\cos(A+B) = \cos A \cos B - \sin A \sin B \quad (15)$$

$$\begin{aligned} \delta t_{ccw} = & [L_1 R_1 \cos \theta_1 + L_2 R_1 \cos \theta_2 + L_3 R_2 \cos \theta_3 + L_4 R_2 \cos \theta_4 \\ & + L_5 R_3 \cos \theta_5 + L_6 R_3 \cos \theta_6 + L_7 R_4 \cos \theta_7 + L_8 R_4 \cos \theta_8 \\ & + L_9 R_5 \cos \theta_9 - L_1 R_1 \delta\theta_1 \sin \theta_1 - L_2 R_1 \delta\theta_2 \sin \theta_2 - L_3 R_2 \delta\theta_3 \sin \theta_3 - \dots] \frac{\Omega}{c^2} \end{aligned} \quad (16)$$

The first nine terms of Equation (16) are equivalent to Equation (10). Following these terms, there are further terms of the same type presented in the equation. These terms, when multiplied by Ω/c^2 , give additional time terms. The entire equation shows that

using a non-reciprocal interferometer has the effect of taking the reciprocal scale factor and adding terms to it. These terms can either increase or decrease the sensitivity of the interferometer depending on the geometry of the interferometer. The remaining terms not shown are covered in Appendix C where the entire equation is shown.

Given Equation (16), the time it takes for the beam to propagate around the interferometer in the counter rotating directions is: $t_{ccw} = t + \delta t_{ccw,r} + \delta t_{ccw,nr}$ and $t_{cw} = t - \delta t_{cw,r} - \delta t_{cw,nr}$. The terms $\delta t_{ccw,r}$ and $\delta t_{ccw,nr}$ represent the parts of Equation (16) that are equivalent to the reciprocal case and those terms that are different from the reciprocal case respectively. The same is true for the clockwise rotating beam. Because the reciprocal and non-reciprocal terms are combined into one equation, Equation (16), the time terms are reduced to: $t_{ccw} = t + \delta t_{ccw}$ and $t_{cw} = t - \delta t_{cw}$. The total time difference is then:

$$\Delta t_{nr} = t_{ccw} - t_{cw} = \delta t_{ccw} + \delta t_{cw} \quad (\text{sec}) \quad (17)$$

where all the terms are as previously described. This form is the same as for the reciprocal case, however, in this case δt_{ccw} is not necessarily equal to δt_{cw} and further reductions cannot be made.

3.4. *Fundamental Detection Limit*

There is a fundamental limit of detection associated with I-FOGs, and also with the AFIT MiG [6]. The limit is due to photon shot noise meaning that the uncertainty of the detector to directly measure the intensity of light input into it. The fundamental detection limit $\delta\Omega$ is given by [6]:

$$\delta\Omega = \frac{c}{LD} \frac{\lambda/2}{(n_{ph}\eta_D\tau)^{\frac{1}{2}}} \quad (\text{rad}) \quad (18)$$

Where: LD – Fiber Length and Diameter in meters²

n_{ph} - Number of photons/sec arriving at the photodetector in photons/s

η_D - Photodetector quantum efficiency

τ - Averaging time in s

c - Speed of light in a vacuum in meters/s

λ - Wavelength of the light used in the interferometer in meters

This limit is a measure of the minimum change in rotation rate the sensor is able to detect. Given ideal conditions this limit would give the lowest rotation detectable. Even with non-ideal conditions, this equations still gives a good approximation of what the minimum detectable rotation rate would be. This limit is a function not only of the length of the interferometer, but also of the quality of laser and detector used. To achieve a low fundamental detection limit, and thus be able to determine smaller rotation rates, high quality photodetectors must be used.

As with the determination of the previous AFIT MiG equations, formulas independent of path geometry need to be determined. To accurately re-derive the fundamental detection limit requires insight into photonics, which is beyond the scope of this research so a simpler method will be employed.

From the derivation of equations for an I-FOG in [6] the following relationships are known and can be easily derived:

$$A = \frac{\pi D^2}{4} \quad (\text{meters}^2) \quad (19)$$

This equation relates the area of a circle to the diameter. The relationship:

$$N = \frac{L}{\pi D} \quad (\text{meters}) \quad (20)$$

relates the number of turns in a coil to the coil length and diameter. The final relationship:

$$\Delta t = \frac{4AN}{c^2} \cdot \Omega \quad (\text{sec}) \quad (21)$$

is the Sagnac equation for an I-FOG where all the terms are as previously described.

Substituting Equations (19) and (20) into (21) and rearranging gives:

$$\frac{1}{c\Delta t} = \frac{c}{LD\Omega} \quad (22)$$

This equation relates LD to the time difference from rotation for an interferometer, $c\Delta t$.

Using the Δt solution from the reciprocal case of the AFIT MiG, Equation (10) and solving for LD gives:

$$LD = 2[L_1 R_1 \cos\theta_1 + L_2 R_1 \cos\theta_2 + L_3 R_2 \cos\theta_3 + L_4 R_2 \cos\theta_4 + L_5 R_3 \cos\theta_5 + L_6 R_3 \cos\theta_6 + L_7 R_4 \cos\theta_7 + L_8 R_4 \cos\theta_8 + L_9 R_5 \cos\theta_9] \quad (23)$$

Using this relationship for LD in the fundamental detection limit equation gives:

$$\delta\Omega = \frac{c}{4 \left[\begin{array}{l} L_1 R_1 \cos\theta_1 + L_2 R_1 \cos\theta_2 + L_3 R_2 \cos\theta_3 + L_4 R_2 \cos\theta_4 \\ + L_5 R_3 \cos\theta_5 + L_6 R_3 \cos\theta_6 + L_7 R_4 \cos\theta_7 + L_8 R_4 \cos\theta_8 \\ + L_9 R_5 \cos\theta_9 \end{array} \right]} \frac{\lambda}{(n_{ph} \eta_D \tau)^2} \quad (24)$$

This form of the fundamental detection limit gives the detection limit in terms of path length of the interferometer. To account for the non-reciprocal case the non reciprocal time term would be substituted into the fundamental detection limit equation.

3.5. *Summary*

The non-circular geometry of the AFIT MiG precludes using the standard implementations of the equations describing the Sagnac effect to solve for the phase shift due to rotation. To accommodate interferometers of any shape, the Sagnac equation was re-derived from the viewpoint that the Sagnac effect causes a time shift in the propagation time of a laser beam around an interferometer. Because of the wave nature of light, this time change causes a shift in the interference pattern at the detector of the interferometer. This shift in interference pattern is what is measured to pull off of the interferometer rotation information.

There is a distinct limit to how small of a rotation a Sagnac interferometer can measure. This is the fundamental detection limit for the interferometer. While the theory behind the detection limit is beyond the scope of this research, a general equation for an I-FOG was analyzed and converted over to use for the AFIT MiG.

The Sagnac equation for the AFIT MiG, and the detection limit were solved for both the reciprocal case and also the case where the interferometer exhibited non-reciprocities. The non-reciprocal case was similar to the reciprocal case and does not prevent the interferometer from functioning.

Chapter 4 uses the equations and relationships derived in this chapter to determine what rotations the AFIT MiG is capable of sensing. The chapter also applies the AFIT

MiG to flight profiles generated in MATLAB to determine how well it tracks changes in rotation. Both the reciprocal and non-reciprocal cases are covered in Chapter 4. The differences in performance for each case are analyzed.

4 *Simulation and Results*

4.1 *Gyroscope Equation*

The derivations of Chapter three arrived at an equation for the theoretical performance of the AFIT MiG. The final derivation, Equation (10) gives the expected phase difference between two counter rotating laser beams at the detector for a given rotation rate, Ω . This derivation assumed that both the clockwise and counterclockwise paths are reciprocal. Equation (16) gives the same relationship when the paths are not reciprocal. The noise in the gyroscope is modeled by Equation (24) in the form of the fundamental detection limit. When the gyroscope is operated it is biased at a certain operating point and so there are no unknown biases for the AFIT MiG. The one thing not modeled or accounted for is drift. The reason for this is that the theoretical drift for an optical gyroscope is zero. The main cause of drift in macro-optical gyroscopes is due to temperature gradients [8]. Normally this would be modeled; however, the small size of the AFIT MiG should negate most of these effects and so for this research the drift is not modeled.

The chief concern of a MEMS optical gyroscope is ensuring that the path length is sufficient to allow for detection of rotation. The detection of rotation is achieved by measuring the intensity of the interfering beams. A change in intensity is caused by a change in rotation rate. If the intensity of the interferometer is known when the device is not rotating, then any deviation from this non-rotating state, assuming a perfect device, is due to a rotation. The intensity is a function of the phase difference due to rotation. The intensity is given as

$$I = I_1 + I_2 + 2\sqrt{I_1 I_2} \cos(\Delta\phi) \quad (\text{W/cm}^2) \quad (25)$$

where I_1 and I_2 are the intensities of the counter rotating beams. The variable in this equation is the phase difference, $\Delta\phi$, from Equation (10). Thus, the intensity of the gyroscope is due to the rotation rate Ω .

As previously mentioned the phase measurement is subject to noise, therefore, the exact rotation rate is not known. What is known is a mean rotation rate with some standard deviation of the noise. If the noise is kept small, the mean rotation rate is a good estimate of the actual rotation rate. When there is a change in rotation rate there is movement along the curve generated by Equation (25). However, when the noise level is high, this change may be undetectable, since the rotation rate change cannot be detected when it is below the noise floor. Also, the actual rotation rate is hard to determine below this noise floor, because there is no measurable shift in the mean of the intensity.

The noise is generated by Equation (24) and is called photon shot noise. Photon shot noise is an uncertainty in the current generated in the photodetector due to light. When light impinges upon the photodetector it causes electron-hole pairs to be generated. These electron-hole pairs cause the current in the photodetector, and this current is what is measured. In any semiconductor material, however, electron-hole pairs are randomly generated throughout the material. It is possible for enough electron-hole pairs to be generated to generate a measurable amount of current. This current is added to the current generated from the light impinging on the photodetector. In an interferometer this increased current is sensed as a rotation. Because the current generated by excess electron-hole pairs is random it is modeled as white noise in interferometer models. Therefore, if a rotation is to be properly measured the current change in the photodetector

is causes must be greater than the random shifts caused by random electron-hole pair generation. The amount of noise and how it effects the measurements of rotation is discussed in Section 4.2.

4.2. Noise Level

4.2.1. Reciprocal Case The first concern for the AFIT MiG is to determine the noise floor. If the noise level is too high, than the interferometer will not be able to sense any reasonable rotation rates. The fundamental detection limit for the case of perfect reciprocity is given by Equation (24). For a five-leg interferometer built on a 1 cm by 1 cm die the fundamental detection limit is 0.0231 rad/sec. The wavelength of the laser used was 980 nm, the efficiency of the photodetector was 0.3, the number of photons incident on the detector was 3×10^{15} photons/sec, and the averaging time was 1 sec. Rotation rates slower than this value will be indistinguishable from the noise. Recall that this value is a function of the detector and laser used; more efficient detectors and powerful lasers would lower the detection limit.

Given this lower limit of detectability, the question is then asked; is this value low enough? If the detection limit is to high, than the gyroscope will not be useful for anything except a mental exercise. The detection limit of 0.0231 rad/sec is equivalent to 1.324 deg/sec. It will be shown later in this Chapter that this detection limit is low enough to be useful for both military and civilian applications.

4.2.2. Non-Reciprocal Case Since the actual AFIT MiG is not a reciprocal gyroscope, the next question is how does the non-reciprocity affect the detection limit. For the simple five-sided interferometer case equivalent to the reciprocal case the detection limit occurs at 0.0231 rad/sec. This is equal to 1.324 deg/sec. This shows that

theoretically the non-reciprocal AFIT MiG will have an equal noise level to the reciprocal AFIT MiG. Thus, the non-reciprocal interferometer should also perform adequately for civilian and military applications.

4.2.3. Additional Equation Terms Recall that the performance of an interferometric gyroscope is based on the path length of the device. The longer the path length, the smaller the rotation angles that will be detectable. To increase the accuracy of the AFIT MiG, and thus make the fundamental detection limit smaller, additional optical legs are required.

4.2.3.1. Additional Terms: Reciprocal Case The ideal interferometer should be reciprocal, and additional legs should increase the accuracy. Table 2 gives values for the number of optical legs in the gyroscope and the corresponding detection limit. The geometry of the optical path in Figure 21 was used to determine all parameters.

Notice that as the number of optical legs in the gyroscope increases, the fundamental detection limit decreases. The detection limit is cut by a factor of almost 2 when the number of legs in the gyroscope is doubled. As the number of legs increases, the size of

Table 2. Detection Limit

Number of Optical Legs in the AFIT MiG	Detection Limit in rad/sec	Detection Limit in deg/sec
9	0.0118	0.6761
10	0.0106	0.6073
11	0.0097	0.5558
12	0.0090	0.5157
13	0.0083	0.4756
14	0.0078	0.4469
15	0.0073	0.4183
16	0.0069	0.3953
17	0.0065	0.3724
18	0.0062	0.3552

each additional optical leg decreases. Therefore, each additional leg decreases the fundamental detection limit less than the previous leg. For example, the decrease in the detection limit caused by going from 9 to 10 legs is 0.0012 rad/sec while the decrease in the detection limit created by the addition of the 18th leg is only 0.0003 rad/sec. Notice, however, there is a practical limit to the number of additional optical legs that may be added. Therefore, there is a trade-off between the complexity induced with adding additional legs compared to the minimal gain achieved in the detection limit.

The decrease in additional gain for each additional optical leg is more easily seen in Figure 23. Here it is shown that the trend is almost a reverse exponential, implying that as the number of optical legs increases, the gain from each additional optical leg quickly approaches zero. Because the device in question is a MEMS device, the law of diminishing returns is not as pronounced as for a macroscopic device. This occurs since the device is constructed using semiconductor manufacturing techniques. Thus, the

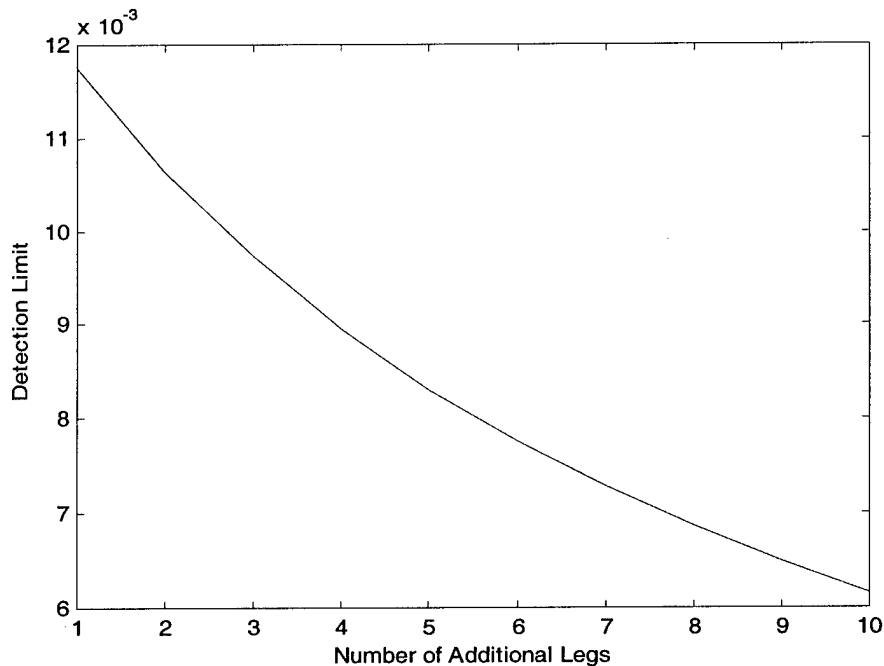


Figure 23. Law of Diminishing Returns For The AFIT MiG

addition of additional optical legs only requires adding them to the initial design. When the devices are mass-produced, each additional optical leg will be added to all devices, without any additional manufacturing cost. In fact, since the device is a MEMS device, the size of the gyroscope is more important than the number of optical legs. Recall also, that the number of optical legs must be limited because of the loss of optical power as the laser traverses the interferometer. In practice the designer cannot fill up the chip with optical legs until there is no longer any room for more legs.

4.2.3.2. Additional Terms: Non-Reciprocal Case Since the AFIT MiG is a non-reciprocal device, the effect of non-reciprocity along with the addition of optical legs needs to be determined. The geometry for the non-reciprocal AFIT MiG simulated used the geometry of Figure 21 for the clockwise path, and the geometry of Figure 22 for the counterclockwise optical path. Table 3 gives the results for the non-reciprocal interferometer with additional optical legs. The format is the same as for Table 2. This data shows the same trends as the data in Table 2. As the number of optical legs Non-Reciprocal Detection Limit

Number of Optical Legs in the AFIT Mig	Detection Limit in rad/sec	Detection Limit in deg/sec
9	0.0118	0.6761
10	0.0107	0.6131
11	0.0097	0.5558
12	0.0090	0.5157
13	0.0083	0.4756
14	0.0077	0.4412
15	0.0073	0.4183
16	0.0069	0.3953
17	0.0065	0.3724
18	0.0062	0.3552

increases the detection limit decreases. The decrease in improvement in detection limit from the addition of each optical leg from Figure 23 is duplicated in Figure 24, which shows the same inverse exponential curve.

The data collected in tables 2 and 3 does not differ by much. There is little difference between the scale factors for the reciprocal and non-reciprocal AFIT MiGs. Because the scale factors differ so little it would be expected that the two cases would also have similar detection limits. This fact is verified in Table 4. Table 4 shows the amounts the reciprocal and non-reciprocal cases differ. While the two cases differ in two places the overall trend is that the detection limit is the same for both the reciprocal and non-reciprocal AFIT MiG.

Given the data in Tables 2, 3, and 4, the number of optical legs in the AFIT MiG does not matter beyond a certain point. The amount of legs to be designed in an actual device is dependent upon other factors such as the losses incurred by each additional mirror added to the interferometer.

4.3. *Wavelength Dependency*

4.3.1. *Scale Factor Sensitivity* Recalling both the AFIT MiG scale factor, Equation (10), and the fundamental detection limit Equation (24), notice that both equations are dependent on the wavelength of the light used. Up to now the wavelength was not discussed since it is considered constant for any particular device. In reality, however, no laser is truly monochromatic and has in fact a small range of possible wavelengths. While this wavelength error could cause a perturbation in the operation of the gyroscope, it is very small and usually neglected.

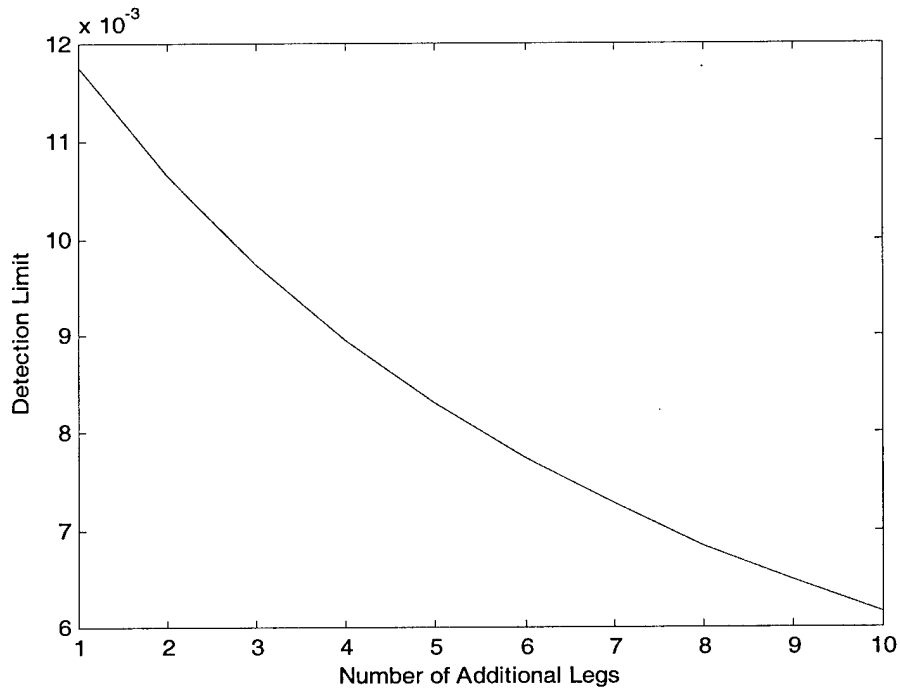


Figure 24. Law of Diminishing Returns for the Non-Reciprocal AFIT MiG

Table 3. Reciprocal/Non-Reciprocal Differences

Number of Additional Optical Legs in the AFIT MiG	Difference in rad/sec	Difference in deg/sec
1	0.0000	0.0000
2	0.0001	0.0057
3	0.0000	0.0000
4	0.0000	0.0000
5	0.0000	0.0000
6	-0.0001	-0.0057
7	0.0000	0.0000
8	0.0000	0.0000
9	0.0000	0.0000
10	0.0000	0.0000

Even though the error due to non-monochromatic light is often neglected in optical gyroscopes, it is still desired to determine how the AFIT MiG would perform using different median wavelengths of light. To determine the phase shift due to rotation the

scale factor from Equation (10) is multiplied by the radian frequency of the light. The frequency is the speed of light divided by the wavelength of the light. This means that the wavelength term, λ , is in the denominator of the final phase shift equation. As the wavelength is decreased the scale factor should increase. Figure 25 plots the output of the scale factor equation for different wavelength values. The rotation rate vector is an increasing ramp function. As is expected, the shorter the wavelength the steeper the scale factor, and the steeper the scale factor, the better the performance. The reason for the increase in sensitivity is that as the wavelength gets shorter, the difference in number of wavelengths between the two counter rotating beams increases. A given rotation then causes a greater change in intensity at the detector. There is one draw back to using shorter wavelength light. As the wavelength decreases so does the

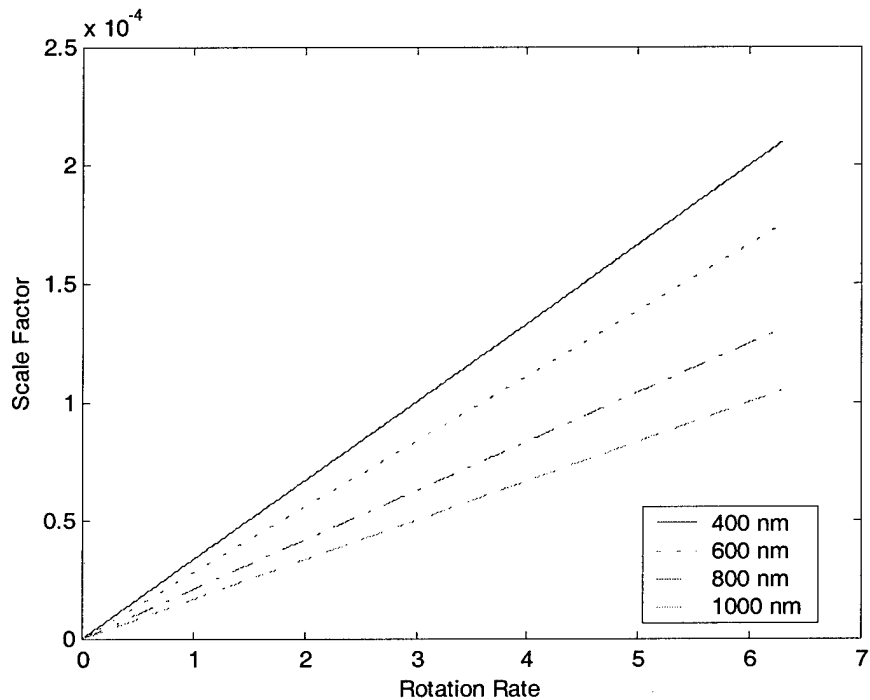


Figure 25. Scale Factor Sensitivity To Wavelength

maximum detectable rotation rate. To understand how, reference the intensity equation:

$$I = I_1 + I_2 + 2\sqrt{I_1 I_2} \cos(\Delta\phi) \quad (26)$$

Since the cosine term repeats itself every 2π , rotations causing a phase difference 2π apart are not discernible from one another. A shorter wavelength means that the difference will approach this 2π limit more quickly than a longer wavelength interferometer. To completely discern all rotations the gyroscope must be limited to operate in a range where $-\pi < \Delta\phi < \pi$. Smaller wavelengths limit the range of rotation rates that fall within this limit. Ergo, the designer must decide in choosing an appropriate wavelength for the gyroscope whether it is more important to sense small rotations or to have a greater range of operation.

If a gyroscope needs both a low detection limit and a broad range, tradeoffs can be made to get optimal performance for both constraints. The longer the optical path of the gyroscope the greater the detection range. However, on a MEMS gyroscope there is a finite amount of space available to place the optical path beyond which the range of operation for a given wavelength cannot be extended. Furthermore, the limits on the number of mirrors due to optical power dissipation come into play.

4.3.2. Detection Limit Sensitivity The fundamental detection limit also depends upon wavelength, but in an opposite manner compared to the scale factor. In the fundamental detection limit Equation (24), the wavelength is in the numerator. Thus, as the wavelength decreases, so does the fundamental detection limit. Table 5 gives

Table 4. Fundamental Detection Limit Wavelength Sensitivity

Wavelength in nm	Fundamental Detection Limit in rad/sec	Fundamental Detection Limit in deg/sec
400	0.0031	0.1776
600	0.0038	0.2177
800	0.0050	0.2865
1000	0.0063	0.3610

fundamental detection limits for different wavelengths. Since the size of the interferometer was set to 18 legs in this research, decreasing the fundamental detection limit allows for smaller rotation rates to be detected. Additionally, lowering the fundamental detection limit lowers the noise level, ensuring that smaller rotation rates will have intensities above the noise.

4.4. Flight Profile Simulation

In a previous section it was stated that the AFIT MiG's sensitivity should be adequate enough and its fundamental detection limit should be low enough to be a useful sensor. This will be verified through simulation. The AFIT MiG's performance will be evaluated against three different flight profiles generated using a program called Progen from a MATLAB™ INS toolbox [25]. Progen processes user-supplied inputs to generate maneuvers the aircraft will perform over time. The program's output includes a Direction Cosine Matrix (DCM) that transforms coordinates from the body frame to the navigation frame and other flight information. Reference frames will be discussed later in this section. The only information required for this simulation involving the AFIT MiG is the DCM, thus all other information is omitted.

Direction Cosine Matrices are 3×3 matrices of vector projection angles. These matrices are used to transform vector information between bases. A bases is a set of

three unit vectors that can be used to completely describe any point in space. The DCM is used when a vector A , is known in one basis, call it the 1 basis, and the vector is needed in another basis, the 2 basis. The DCM transforms the vector from the 1 basis to the 2 basis. To do so the A vector in the 1 basis is premultiplied by the DCM, for example: $A^2 = {}^2C^1A^1$. In this equation ${}^2C^1$ is the DCM that converts vectors described in the 1 basis to the 2 basis. The information contained in the vector does not change, only the representation of the information changes. For example, a DCM from one basis to another basis would appear as:

$$\begin{bmatrix} 1 & 0 & 0 \\ 0 & \cos\theta & \sin\theta \\ 0 & -\sin\theta & \cos\theta \end{bmatrix} = \begin{bmatrix} 1 & 0 & 0 \\ 0 & 0.924 & 0.383 \\ 0 & -0.383 & 0.924 \end{bmatrix} \quad (27)$$

The values in each location in the DCM are the cosine of the angle between the unit vectors in each of the bases. For instance, element (2,2) is 0.924, this means that angle between the second unit vectors describing the two bases, in this case basis 1 and basis 2, is the arccos of 0.924, or 22.5°. The angle of 22.5° was chosen randomly from the set of all angles between 0° and 90°.

The Progen program DCM gives the transformation from the body frame of the aircraft to the navigation frame. The body frame is a basis that moves with the aircraft. For Progen the body frame x-axis is aligned with the nose of the aircraft, the y-axis is perpendicular to the x-axis and points out the left wing of the aircraft. The z-axis forms a right hand triad and points in the direction of the tail. The navigation frame is the basis that is used to describe the aircraft's trajectory over the surface of the earth. The navigation frame is also called the East, North, Up frame. The x-axis points in the north, the y-axis points to the east, and the z-axis points up from the surface of the earth. The

three axes also form a right hand triad. Both the body frame and the ENU frame are shown in Figure 26. The direction cosine matrix is used in the MATLAB routine DCM2eulr to extract Euler angles. The Euler angles describe the rotations that translate the body frame to the navigation frame. After the Euler angles are extracted from the DCM they are

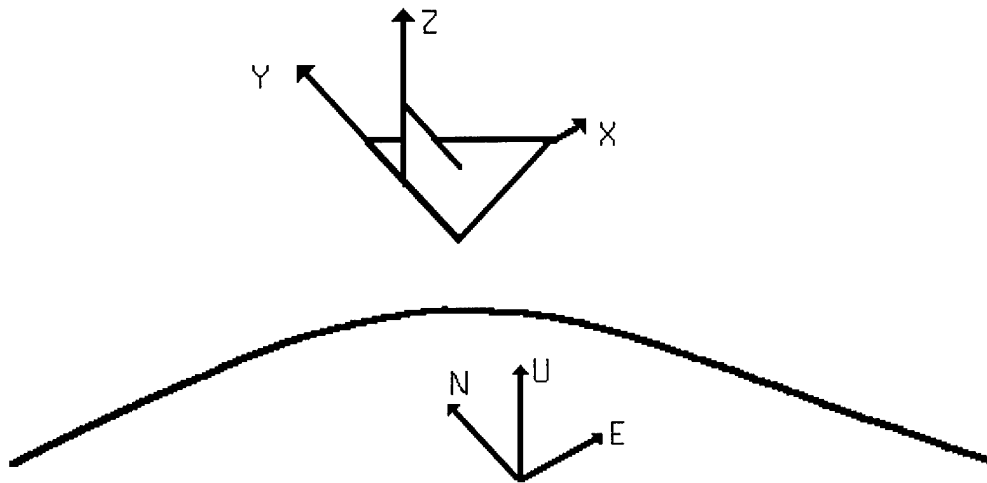


Figure 26. Reference Frames

differentiated to form a vector of Euler rates. While the Euler rates describe the rotations of the aircraft they are not what inertial sensors measure. When inertial sensors are used in a strap down configuration on an aircraft they directly measure the body rates. That is they measure how the aircraft rotates about the body frame. The DCM:

$$\begin{bmatrix} \sin \theta \sin \phi & \cos \phi & 0 \\ \sin \theta \cos \phi & -\sin \phi & 0 \\ \cos \theta & 0 & 1 \end{bmatrix}$$

translates the Euler rates to body rates [15]. In this DCM θ and ϕ are the Euler angles that describe rotations about the y-axis and x-axis respectively. This DCM is used in Equation (28) to extract the body rates ω_x , ω_y , and ω_z from the three Euler rates [15].

$$\begin{bmatrix} \omega_x \\ \omega_y \\ \omega_z \end{bmatrix} = \begin{bmatrix} \sin \theta \sin \phi & \cos \phi & 0 \\ \sin \theta \cos \phi & -\sin \phi & 0 \\ 0 & 0 & 1 \end{bmatrix} \begin{bmatrix} \dot{\psi} \\ \dot{\theta} \\ \dot{\phi} \end{bmatrix} \quad (28)$$

When Progen creates a flight profile it can only use certain maneuvers. When a turn is simulated Progen simulates only constant radius, constant altitude turns. All turns are simulated as instantaneous turns. This causes singularities in the DCM output matrix. Singularities in the body rates also occur because when the Euler angles in the DCM go beyond 90°. Such points cause singularities in the Euler angle solutions and show up in the body rate data. These singularities appear as jumps in the Euler rate data. These jumps are converted to jumps in the body rates when Equation (28) is applied. Analysis of these problems reveals that Progen is not an adequate program to model rotation rates for the simulation of the AFIT MiG. However, no other MATLAB™ routines were available for use during this research, thus Progen was used.

To create the simulations, flight profiles of three different types of aircraft are input into the Progen routine. The Euler angles are extracted from the DCM and converted to Euler rates. The Euler rates are then converted to body rates using Equation (28). Equation (24) is used to simulate noise that would be present in an actual interferometer and the noises are added into the body rate vector. The vector containing the body rates and noise is then input into the AFIT MiG equations. The output of the AFIT MiG equation is the phase difference that would occur in an actual AFIT MiG. This phase difference is placed into Equation (26). The output of Equation (26) is the intensity that

the photodetector on the actual AFIT MiG would sense and convert to voltage. It is this intensity minus two that is plotted. The constant of two is taken off to show how the phase shifts cause shifts in the intensity, it is these changes that show rotation, not the absolute intensity. This subtraction also allows for the data to be plotted more clearly.

If the phase difference were placed directly into Equation (26) the interferometer would be operating about a point of low sensitivity. The sensitivity changes because Equation (26) is a raised cosine equation. The maximum sensitivity of a gyroscope occurs when the phase is $\pi/2$. To keep the gyroscope operating at this maximum point the position of one of the mirrors is piezo-actuated to adjust the phase difference, keeping it at $\pi/2$. Figure 27 is a sketch of the piezo-actuation of one of the mirrors on an interferometer.

Because the intensity equation is a raised cosine values are repeated every π radians of phase shift. To increase the operating range of the interferometer the piezo-actuator uses

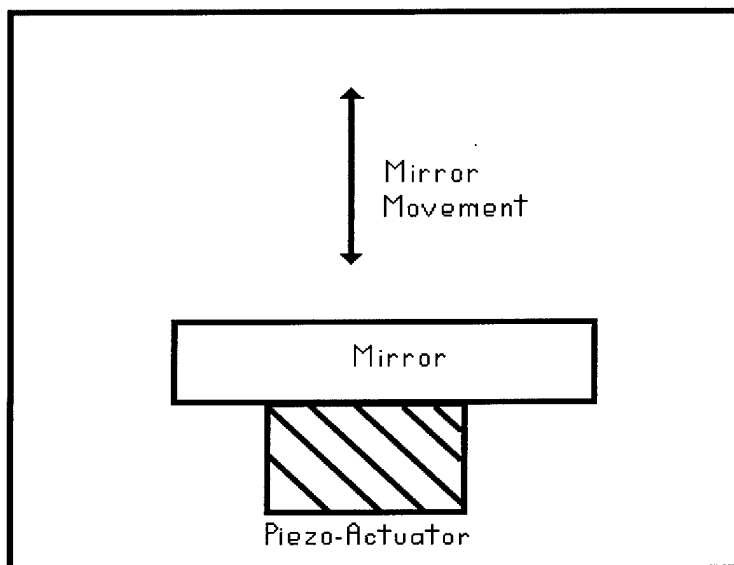


Figure 27. Piezoresistive Modulation of AFIT MiG

two different points of phase bias: $\pi/2$ and $-\pi/2$. To accurately simulate this biasing in the AFIT MiG, the phase input to the interference equation used for simulation is the output of the AFIT MiG simulation added to a square wave that switches from $\pi/2$ to $-\pi/2$ every second.

The first aircraft simulated is the Beechcraft C-12 Super King Air. The flight profile is the same profile used in EENG 635 Summer 1999 at AFIT. Figure 28 is the C-12 ENU flight profile. The body rates for the C-12 flight profile are shown in Figure 29. In describing the body rates the terminology Roll Rate, Pitch Rate, and Yaw Rate will be used to represent rotations about the body x, y, and z rates respectively. Figure 30 is the simulated AFIT MiG pitch rate output. The noise is seen in the data as the width of the output. Rotation rates appear as shifts in the output levels. Comparing the simulated AFIT MiG output to the pitch rate plot in Figure 29 shows that the simulated AFIT MiG

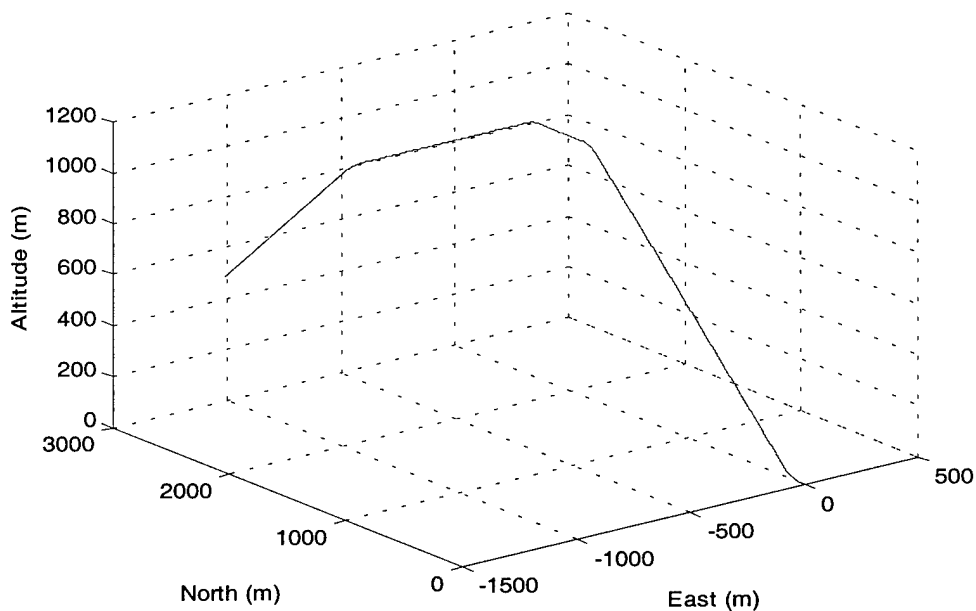


Figure 28. Simulated C-12 ENU Flight Profile

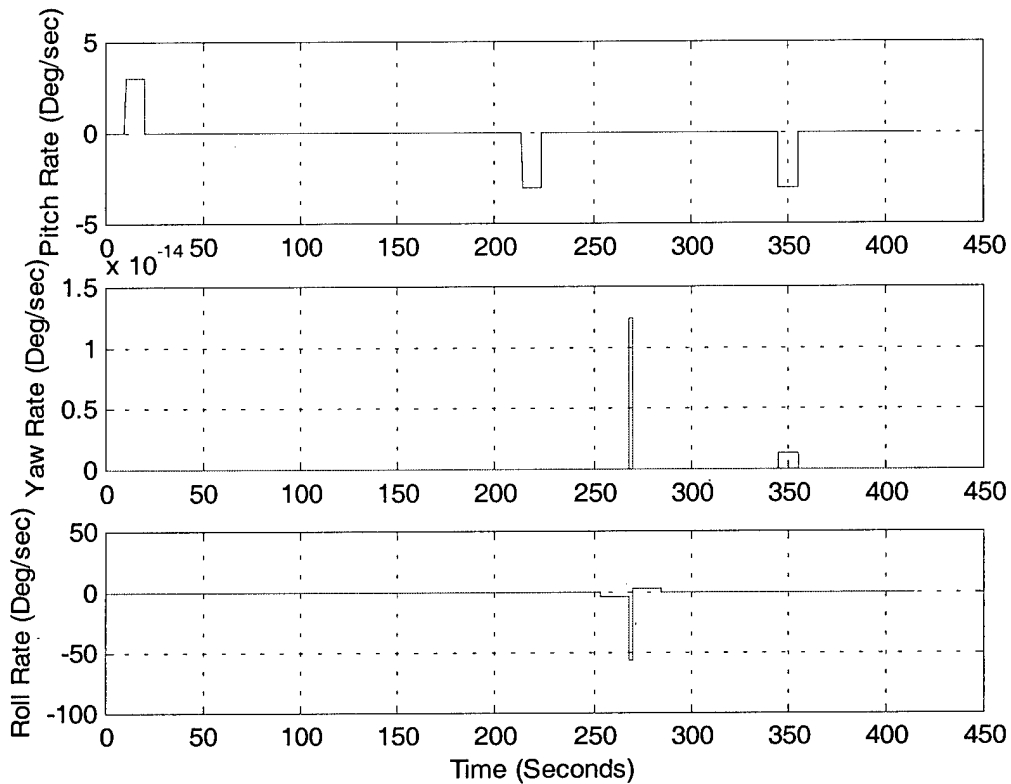


Figure 29. Simulated C-12 Body Rates

is able to sense all the rotation rates in the pitch rate profile. If the output of the simulated AFIT MiG is discernible from the noise, it can be sensed.

The shifting of the output given a rotation is due to the biasing scheme used on the interferometer. With no rotation both the $\pi/2$ and $-\pi/2$ bias inputs give the same output. When there is rotation, however, there is phase shift and the outputs from the different input biases are different. If the roll rate is in the positive direction the positive biased input shifts the output down the intensity curve and the negatively biased input shifts the output up the intensity curve. If roll rate is in the negative direction the effect of the bias inputs on the output are reversed.

Figure 31 shows an enlargement of the first pitch rate sensed in Figure 30. The square

wave output and noise are clearly seen. To determine the direction of the rotation the biasing state must be known. With known biasing state the initial shift in output tells which direction the rotation was in.

Figure 32 is the simulated AFIT MiG roll rate output. All rotation rates from Figure 29 are sensed in the output. At the center of the rotation rate there is a spike in the data. The spike is due to the problem in the way Progen generates flight profiles. The instantaneous turns cause a jump in the roll rates. This jump occurs exactly when the C-12 turns. On either side of the jump is the data sensing the roll into and roll out of the turn. Figure 33 is a close up of the roll data showing the roll into the turn. The noise is also shown in this figure along with the square wave output caused by the biasing input.

Examining Figure 29 shows that there is no yaw rate associated with the C-12 profile. While there is a jump in the data, the yaw rate generated is on the order of 10^{-14} rad/sec. This equates to an order of 10^{-12} deg/sec. This rotation rate is minimal and is due to the

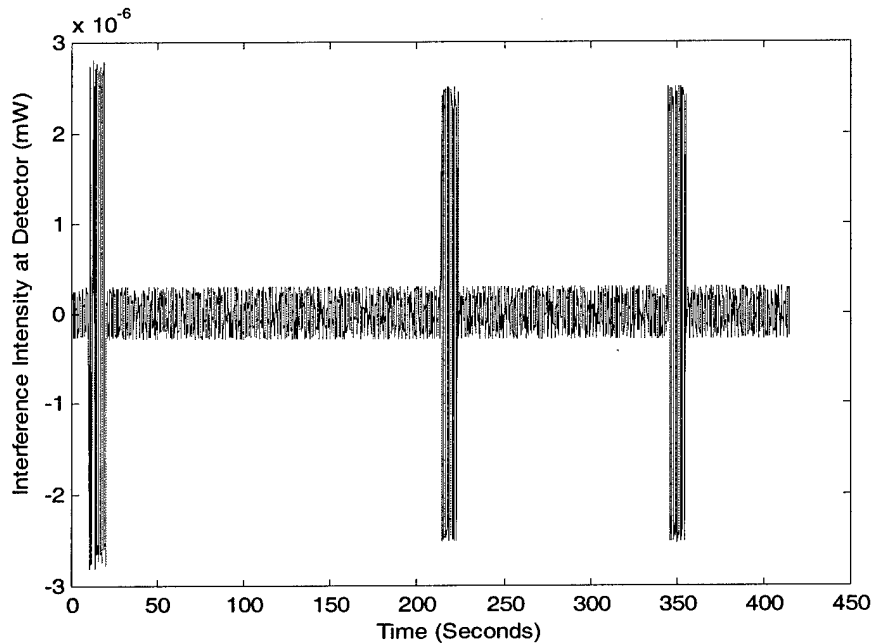


Figure 30. Simulated AFIT MiG C-12 Pitch Rate Output

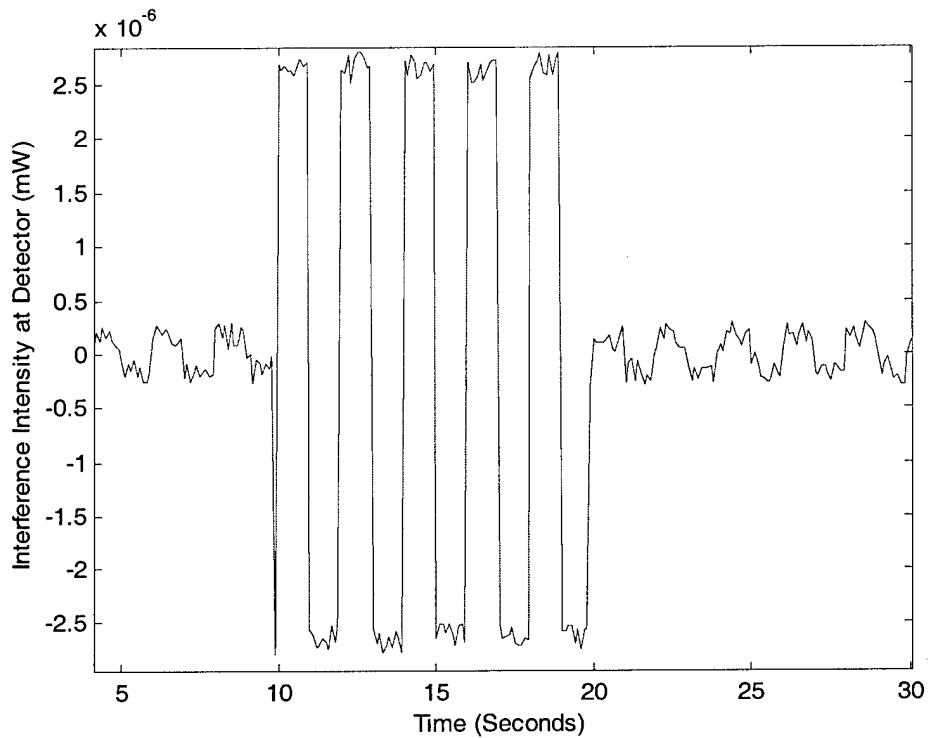


Figure 31. Enlargement of Section of Simulated AFIT MiG Output For C-12 Pitch Rate

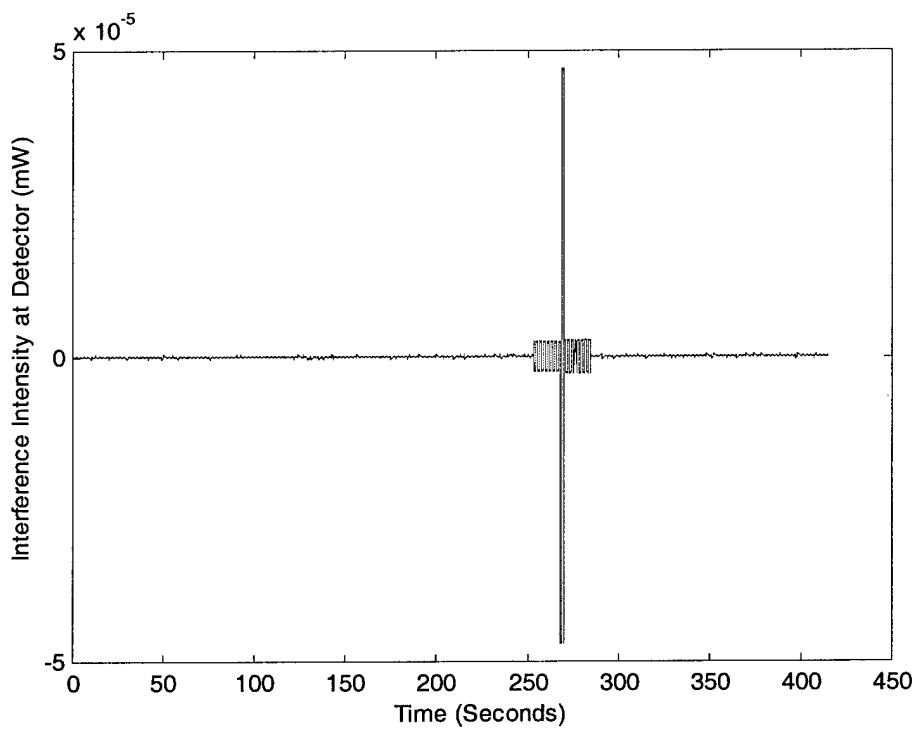


Figure 32. Simulated AFIT MiG C-12 Roll Rate Output

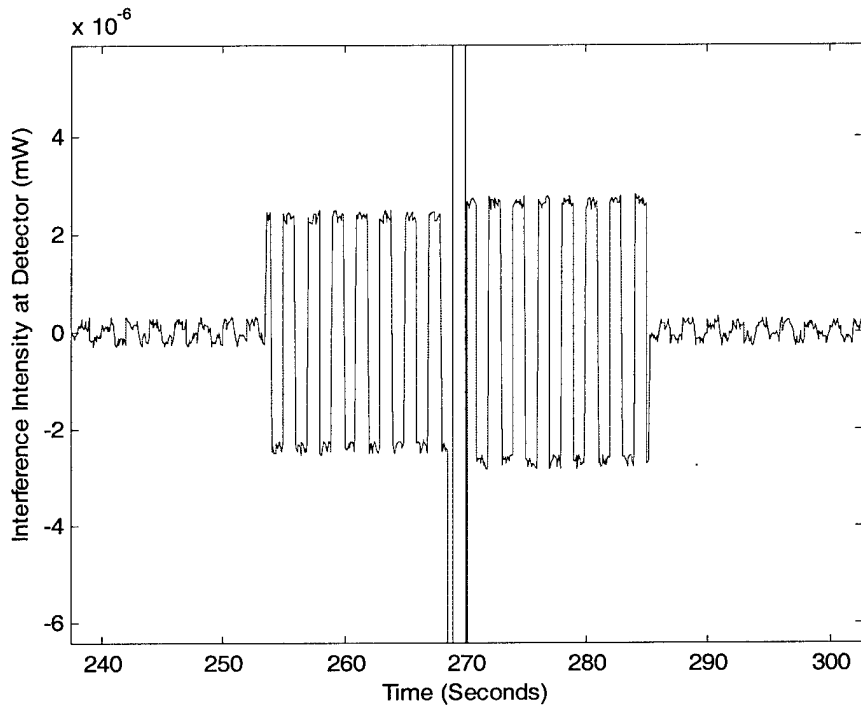


Figure 33. Enlargement of Section of Simulated AFIT MiG Output For C-12 Roll Rate

singularities generated by Progen. Figure 34 shows the simulated AFIT MiG output for the yaw rate. Because there is no yaw rate the plot shows only noise. The jump in data caused by the Progen routine is too low to be simulated by the AFIT MiG.

For the second flight profile a more dynamic aircraft was modeled. The profile is a generic fighter aircraft profile demonstrating high maneuverability and high speeds. The ENU plot of the flight profile is shown in Figure 35. The body rates are shown in Figure 36. In this figure the body rates are shown to spike to over 1000 deg/sec. These spikes are from the singularities caused by the Progen routine. Unfortunately these spikes are so large that they increase the scale of the MATLAB™ plots to a point where the real data is almost indiscernible. If the data is closely examined the points where body rates occur

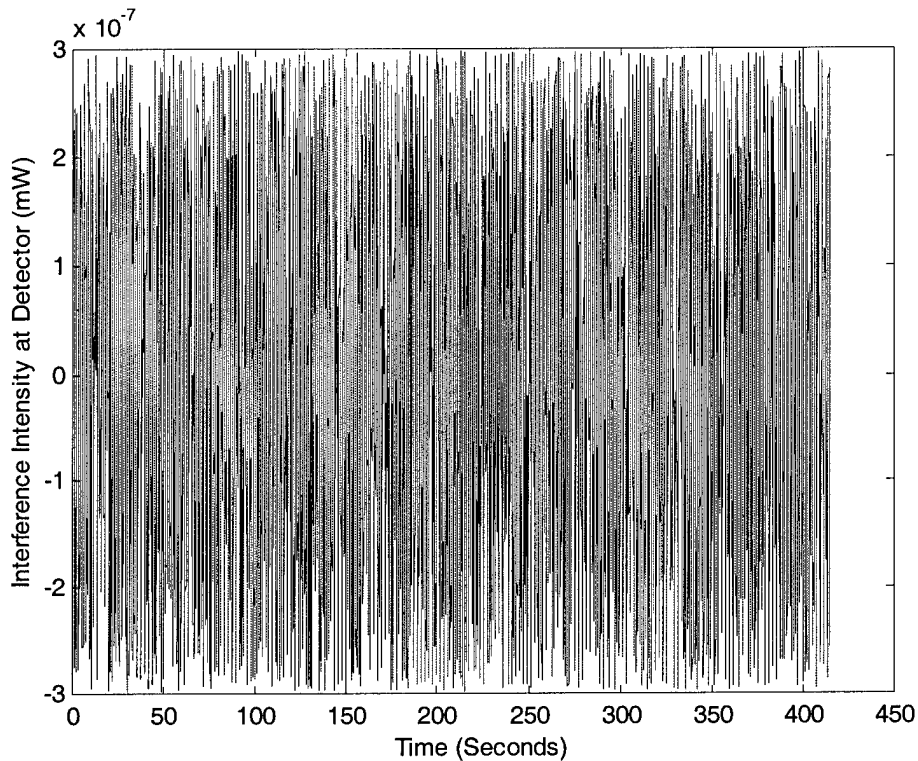


Figure 34. Simulated AFIT MiG C-12 Yaw Rate Output

can be determined. Figure 37 is the simulated AFIT MiG output for the fighter roll. The data shows the spikes from Progen again. The simulated AFIT MiG output does track the roll rates shown in figure 36. Figure 38 and Figure 39 show the simulated AFIT MiG output for pitch rate and yaw rate respectively. The same trends that were discerned in the roll rate analysis are repeated here. The simulated AFIT MiG does sense the rotation rates for both pitch and yaw. Unfortunately the Progen problem is more pronounced for more volatile maneuvers. The singularities occur so often in the fighter body rate data that further analysis is difficult.

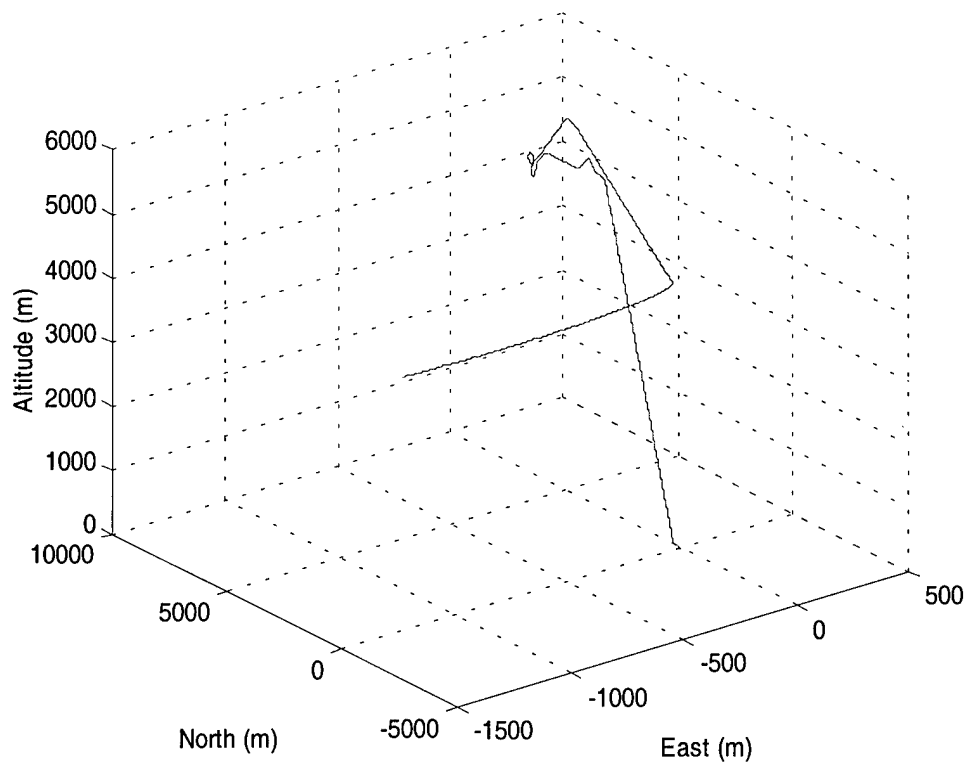


Figure 35. Simulated Fighter Aircraft ENU Flight Profile

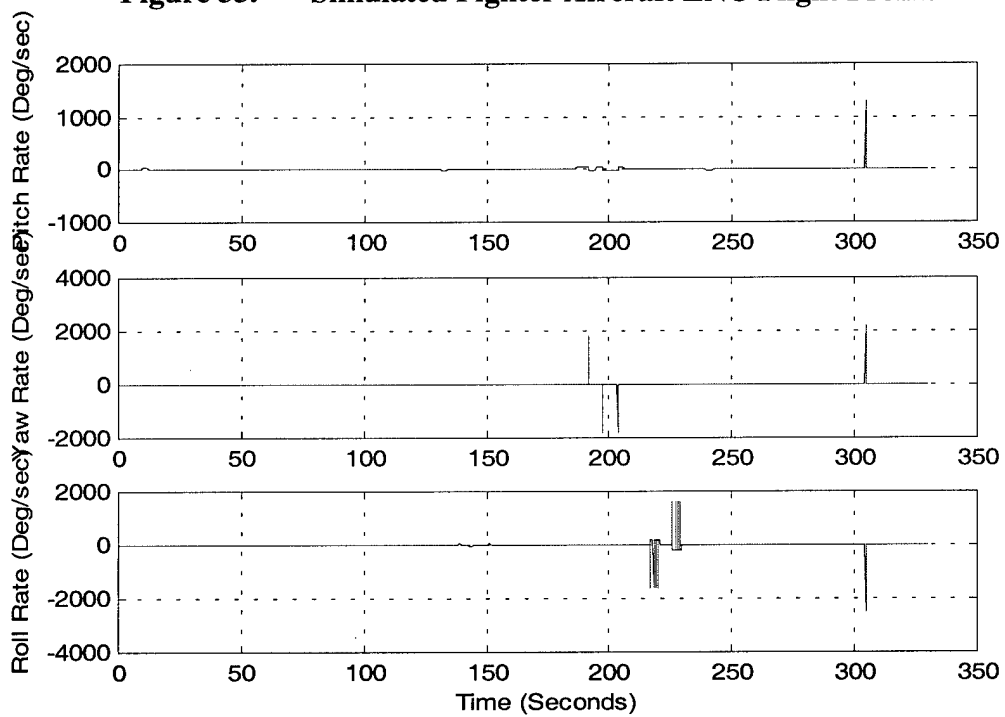


Figure 36. Simulated Fighter Aircraft Body Rates

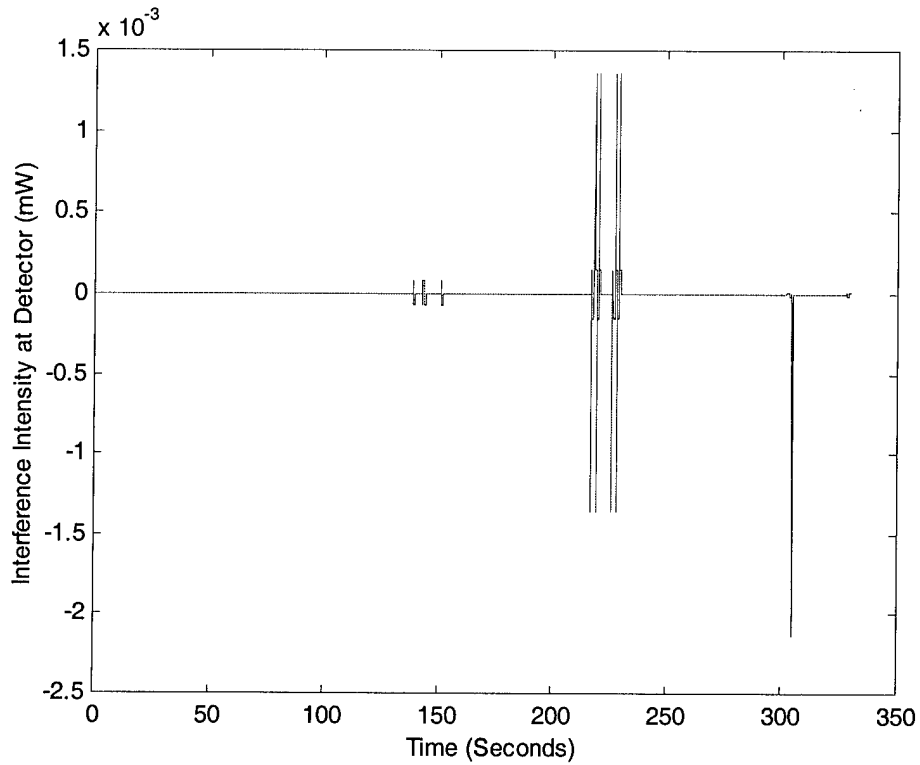


Figure 37. Simulated AFIT MiG Fighter Aircraft Roll Rate Output

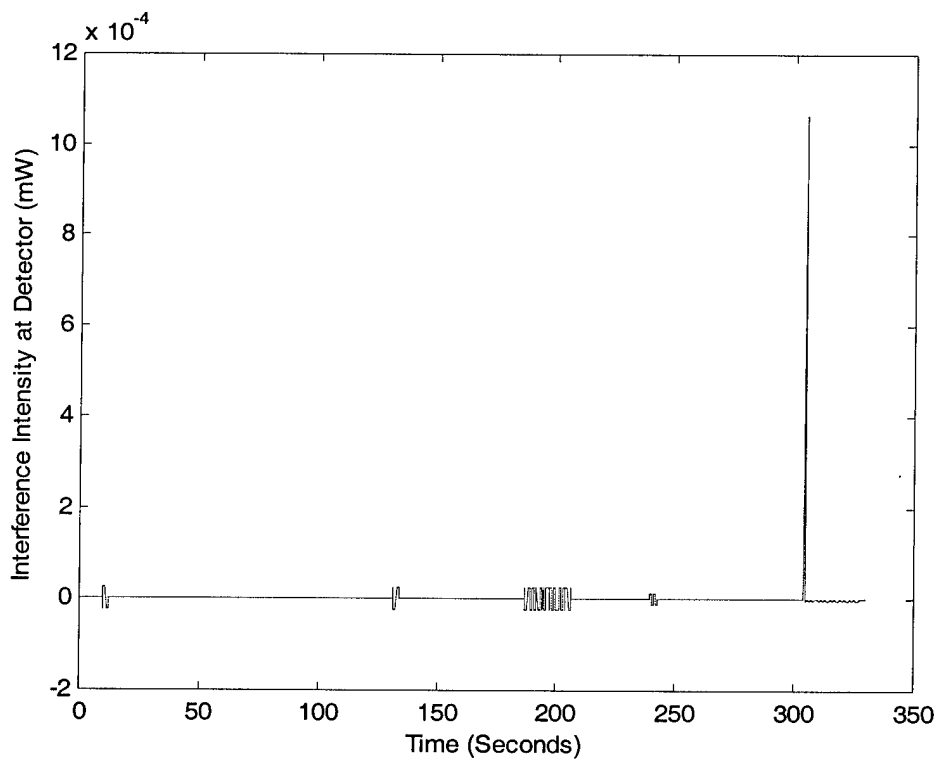


Figure 38. Simulated AFIT MiG Fighter Aircraft Pitch Rate Output

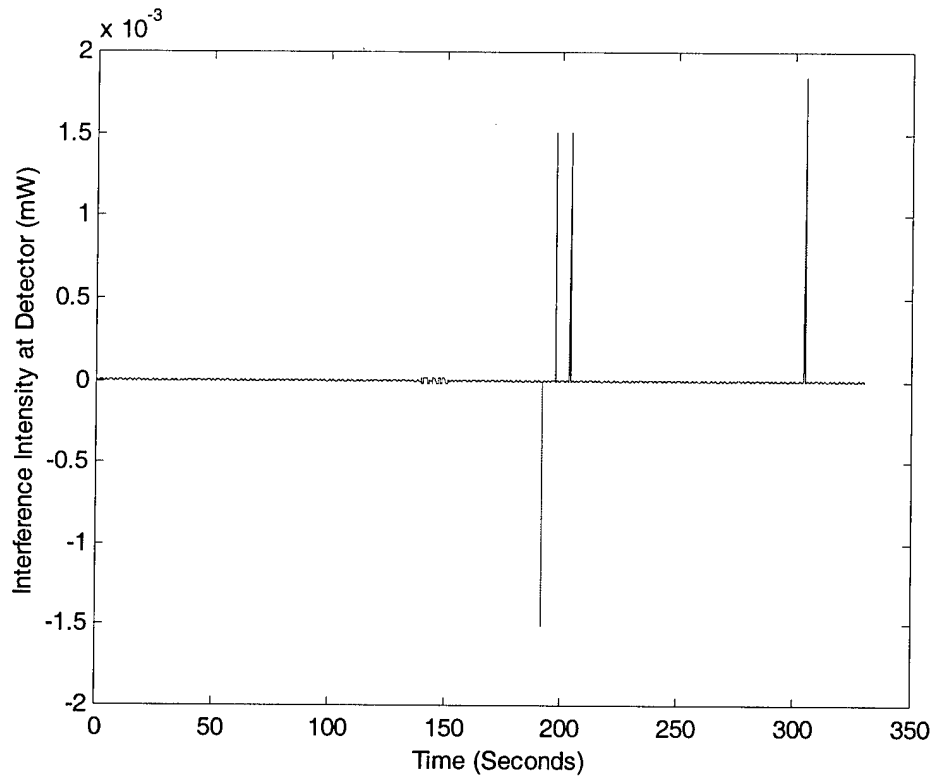


Figure 39. Simulated AFIT MiG Fighter Aircraft Yaw Rate Output

To try and overcome the shortfalls of the Progen profile generator, a third profile was created that ensured the Euler angles never went beyond 90° . No turns were performed which also ensures that no singularities will be generated from the turns. The flight profile consists of straight flight with associated pitches and rolls. Figure 40 is the ENU flight profile for the third simulation case. Figure 41 is the roll and pitch body rates for the profile. The yaw rate is not shown because no yaw was present. A situation with no yaw was also demonstrated for the C-12 profile. To eliminate redundancy the noise plot is not shown here.

Figure 42 is the simulated AFIT MiG roll output. There are no jumps in the data and so the noise and transitions are easily seen. This profile shows how a series of different rotation rates would appear. The amount that the simulated AFIT MiG output varies

from the noise is larger for larger rotation rates. This is what would be expected. In the absence of the biasing input, the output of the simulated AFIT MiG would be a line that showed the different intensity levels. The output without the biasing input would be the envelope of the simulated AFT MiG output shown in Figure 42. This can be thought of as the interferometer being amplitude modulated by the input biasing signal.

Figure 43 is the simulated AFIT MiG pitch rate output. This body rate output is similar to the output of Figure 42. Again there are no jumps in the data so that the noise and phase changes are clearly seen.

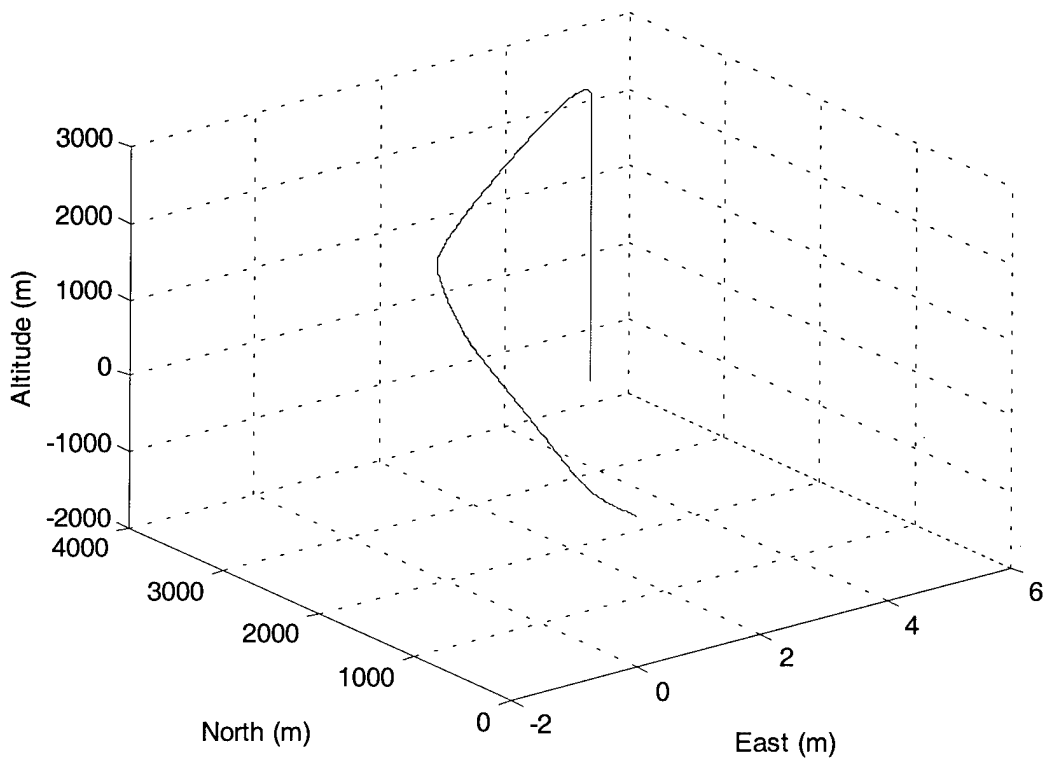


Figure 40. Simulated Third Profile ENU Track

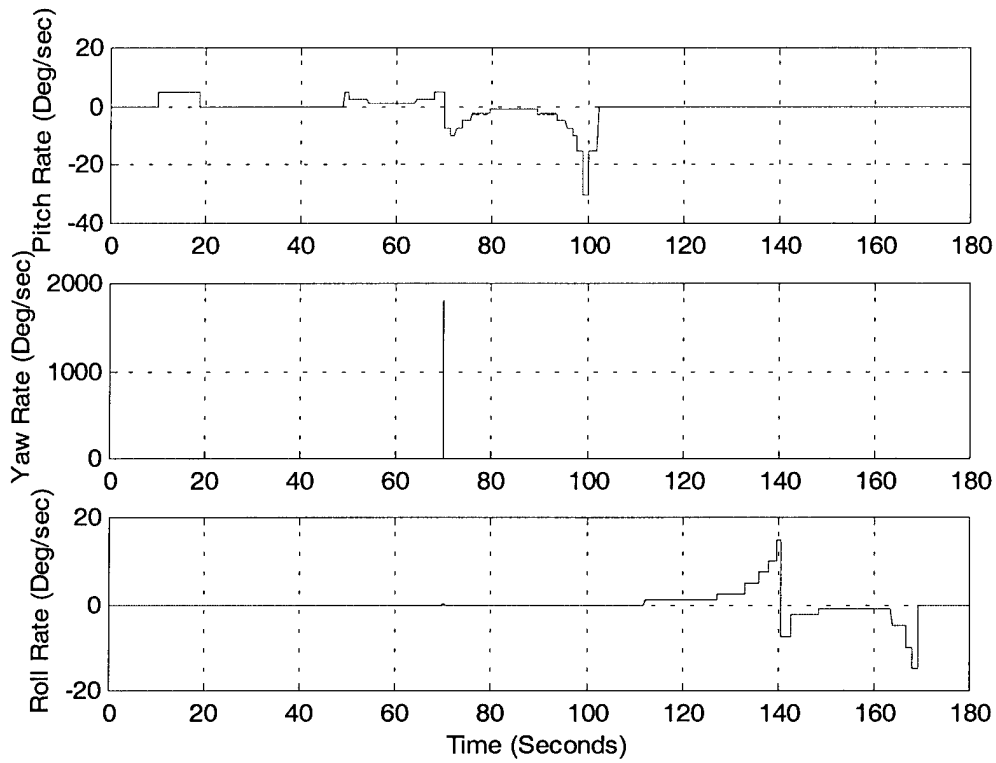


Figure 41. Simulated Third Profile Aircraft Body Rates

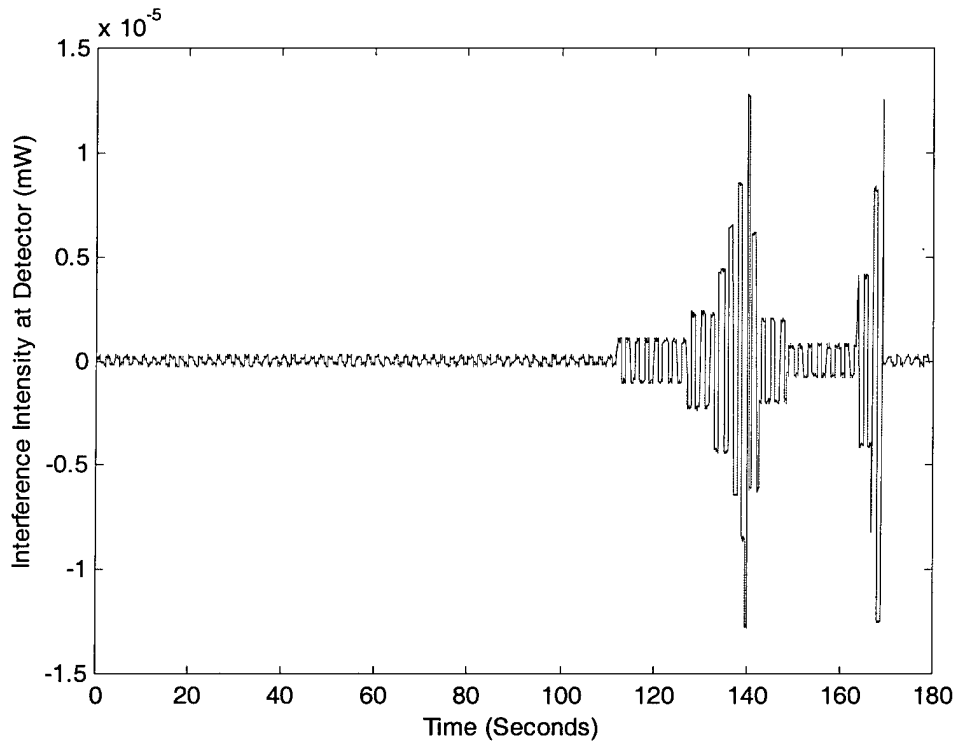


Figure 42. Simulated AFIT MiG Third Profile Aircraft Roll Rate Output

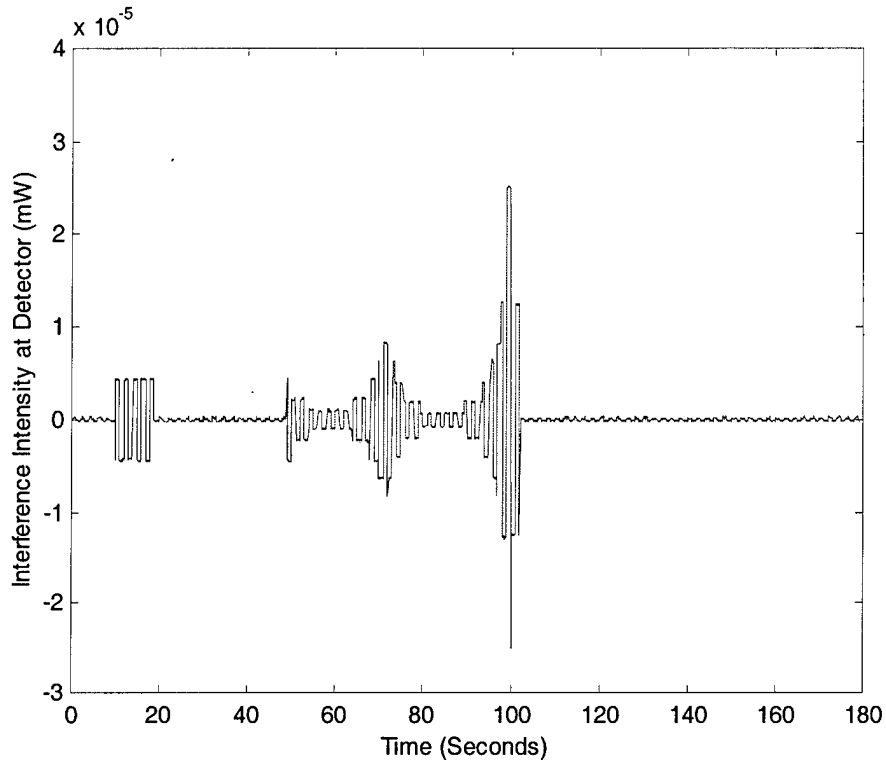


Figure 43. Simulated AFIT MiG Third Profile Aircraft Pitch Rate Output

In all three cases presented above, the interferometer's drift is not modeled. The reason for this is that the theoretical drift for the interferometer is zero [6, 22]. Recall that the main cause of drift in fiber optical gyroscopes is due to a heat gradient over the device. The refractive index of silicon fibers is heat dependent. If there is a heat gradient different parts of the fiber have different refractive indices. Because of the difference in refractive indices in the fiber the light propagates at different velocities through the fiber. This causes a phase difference at the detector of the gyroscope. As time increases the temperature gradient changes and thus the phase differences changes. This causes the interferometer to drift.

The AFIT MiG, through its design, eliminates the above problems. The propagation medium is air, and can be considered free space. The change of the refractive index of

air with respect to heat is negligible under most conditions. This non-volatility of the refractive index with temperature limits the drift in the interferometer. Also, because the size of the AFIT MiG is small, large temperature gradients do not occur across the device. Even if there were gradients present, they would be small across the device and so the drift would be small.

However, even though the theoretical drift in the AFIT MiG is zero, and the design of the AFIT MiG reduces the effect of the factors that cause drift, in reality the gyroscope will exhibit drift. The reasons for the drift could come from differences in material properties on the AFIT MiG or from other sources. Varying electric or magnetic fields across the device could cause drift, possibly even mechanical vibrations. Therefore, even though drift is not modeled it is still possible that drift will occur. To fully characterize the output of a working gyroscope the amount of drift needs to be measured. Once the drift is measured the source should be found and the effects modeled.

4.5. Summary

Despite problems encountered with Progen, the MATLAB™ routine used to generate the flight profiles used in simulation, simulated AFIT MiG results were obtained. The simulated AFIT MiG was readily able to track body rates as described above. Changes in the body rates were tracked in simulation by the AFIT MiG.

Also, it was shown that the non-reciprocity of the AFIT MiG had very little effect on both the overall performance, and the noise performance of the AFIT MiG. Furthermore, there is little value in adding further optical legs to the AFIT MiG after a certain point. Each additional leg provides less gain than the leg added previous to it. If the gain of the

added optical leg is low it might not be worth the added amount of complexity in the AFIT MiG design.

The next chapter covers the design of a MEMS interferometer designed to prove the feasibility of propagating laser light around an open loop MEMS interferometer. If it can be shown that light can indeed be propagated around such an interferometer than the next step would be the design and testing of a functional gyroscope design.

5 *Light Propagation Proof Of Concept Device Design*

5.1 *Conceptualization*

Unfortunately the actual AFIT MiG device could not be constructed. The actual construction of the device would require the use of either a LIGA process or injection molding. No cost-effective methods for either of these processes were available at the time of this writing. It is still important, however, to prove that the concepts involved in the AFIT MiG are feasible. The main concept to prove is that a laser beam can propagate around an open loop MEMS interferometer with acceptable losses. An acceptable loss implies that there is enough energy present at the detector to obtain a useable reading.

Because of the lack of processes available, MUMPS was employed. MUMPS has been used by AFIT in the past and is a reliable process within the MUMPS design constraints. As stated earlier in Section 2.2.2.1, MUMPS is a process that has two releasable layers of thickness 2 μm and 1.5 μm . While structures this thin cannot be used as mirrors, the releasable layer attributes of the MUMPS process allow for flip up mirrors. These flip up mirrors, discussed in detail in this chapter, are used for the light propagation proof of concept device. [17]

There are two main problems with using the MUMPS mirrors that do not allow an actual prototype AFIT MiG to be built. The first problem is that the mirrors are unstable in the upright position. Any mechanical vibrations in the device would cause vibrations of the mirrors. Any vibration of the mirrors would cause changes in path length of the propagating laser beams. These path length changes would of course cause a phase difference between the two laser beams at the photodetector. This phase difference would be unstable and could cause a large drift that would no longer allow for the

detection of useful signals. The second problem with MUMPS mirrors is caused by residual stresses in the MUMPS polysilicon and metal layers. Residual stresses have been measured in these layers to be quite high. The stresses also differ from layer to layer. When multiple layers are used the differences in residual stresses cause the mirrors to curl [19]. Curled mirrors lose the desired reflective properties of flat mirrors and make it difficult to get the laser light to propagate in the required direction.

Even with these poor qualities, MUMPS should be adequate to successfully demonstrate the transmission of laser light around the device. The configuration used for the test device is shown in Figure 44. Sets of MUMPS mirrors were placed at four different locations around the die forming a square. The mirrors were placed in the middle of the die edges to allow maximum area usage. Nominal mirror placement would be in the four corners of the die thus utilizing the entire die perimeter. However, CRONOS Microsystems, the consortium that offers the MUMPS process, uses the corner of every die sight for test fixtures, and so the mirrors were moved to the locations shown in Figure 44. The square and rectangular fixtures located in two places in Figure 44 are bond pads for attaching the laser and photodetector to the interferometer. Multiple pads were placed on the die for redundancy. If one or more pads are damaged during release of the die there will still be sites available for mounting the laser and detector. Multiple sets of mirrors are placed on the die for this same reason. The mirrors on the upper left corner of the die are used to practice the technique of flipping up the mirrors. Damaging these mirrors has no effect on the operation of the device. Also placed on the die are two different sizes of octal mirrors. These mirrors have no real value or use beyond that of

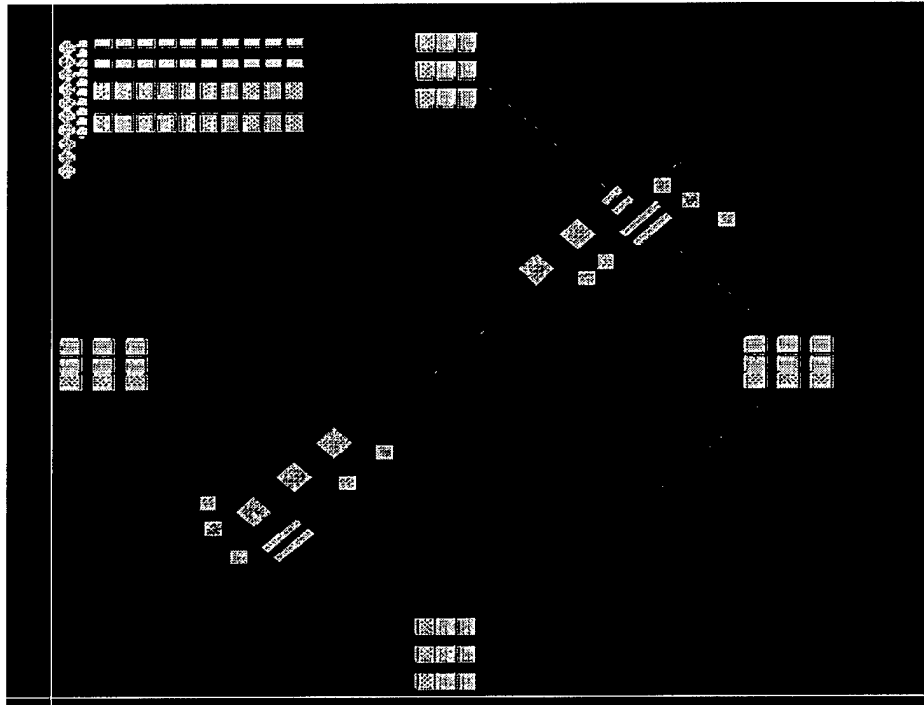


Figure 44. AFIT MUMPS 34 Layout

taking up space on the die. The octal mirrors are mentioned in the research for completeness. The die is $1\text{ cm} \times 1\text{ cm}$ square

The CADENCE layout editor was used in all instances to design the devices. CADENCE is a UNIX based Computer Aided Design (CAD) program that is used to layout Very Large Circuit Integrated (VLSI) circuits and has been altered for MEMS designs [5]. Figure 45 shows the CADENCE layout editor screen. Once the design is laid out on CADENCE and deemed acceptable it is saved to a file and then converted to the Caltech Intermediate Form (CIF). CIF is one of the formats that CRONOS Microsystems via the internet.

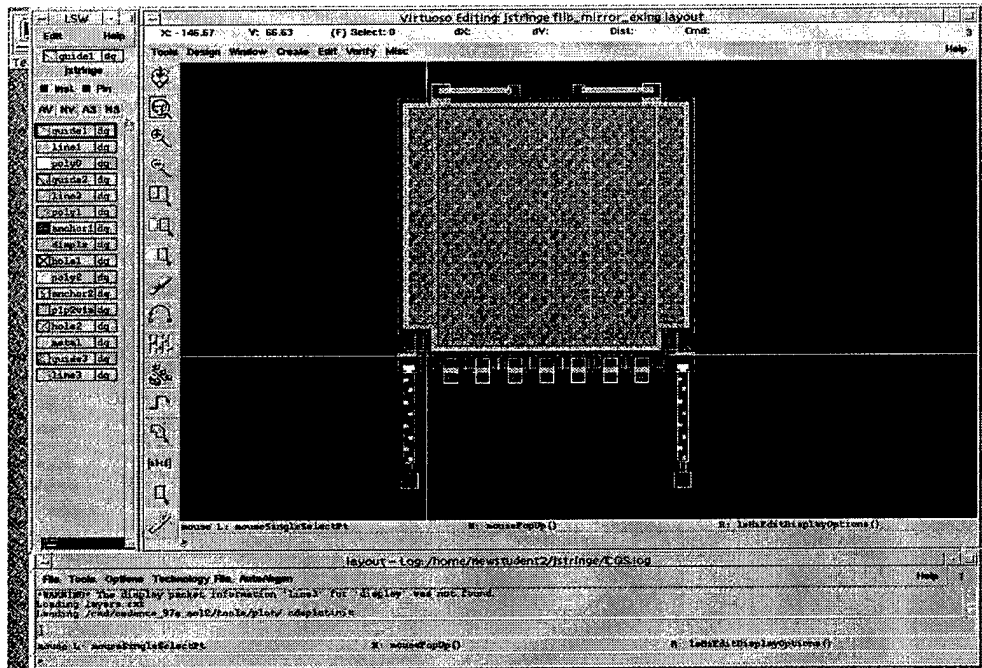


Figure 45. CADENCE Layout Editor

accepts for MUMPS runs. The completed CIF file is then sent by Fast Transfer Protocol (FTP) to CRONOS Microsystems.

5.2. MUMPS Mirrors

5.2.1. Mirror Overview The MUMPS flip up mirrors are constructed of stacked polysilicon and gold. This is done for maximum strength and also to keep the mirrors as flat as possible after release. Residual stresses are built-up in the different MUMPS layers during processing. When the devices are released they tend toward an unstressed state. Because of the different levels of stresses the layers contract or expand differently and cause bowing in MUMPS devices. The worst curling happens when gold is placed on Poly2. The addition of the Poly1 layer should provide greater strength and greater resistance to curling. The hinges and latch structures composing the rest of the mirror are created from a combination of Poly1 and Poly2. The two layers are used along

with the conformal nature of MUMPS to construct the hinges and latches. The construction of such structures are discussed later in this chapter.

5.2.2. MUMPS Hinges The MUMPS hinges are constructed of Poly1 and Poly2 layers. The conformal nature of MUMPS ensures that Poly2 will fill in the areas where no Poly1 is placed. This allows for Poly2 to enclose Poly1 to a certain degree. To form a hinge, Poly1 is shaped into a pin structure that will be attached to the mirror and allow for the mirror to flip up. The Poly1 pin is held to the substrate by Poly2 brackets, which are anchored to the nitride. There is no Poly0 in the hinge structure. The CADENCE design layout of an actual MUMPS hinge is shown in Figure 46. This hinge pin is 206 μm long and 4.5 μm wide. The fingers on the main hinge pin are 10 μm wide by 15.5 μm long. The hinge clamps are rectangles with sides of length 22.5 μm and 12 μm .

Different MUMPS hinges allow for different amounts of movement. Varying the width of the hinge pin varies the amount of movement in the hinge. There is a finite amount of space available for the hinge movement governed by the thickness of the different MUMPS layers. Figure 47 shows a cross section of a MUMPS hinge. The first oxide provides 2 μm of space and the second oxide provides 0.75 μm . Also included in the amount of space available for hinge movement is the 2 μm from Poly1. The hinge pin must be of a size that will allow the hinge to operate properly. Therefore the diagonal of the hinge pin cannot be larger than the 4.75 μm provided by the MUMPS layers. In

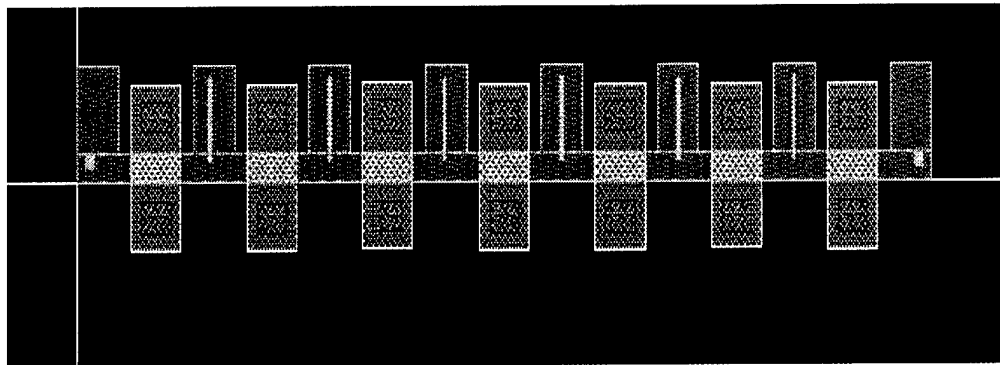


Figure 46. CADENCE Layout of MUMPS Hinge

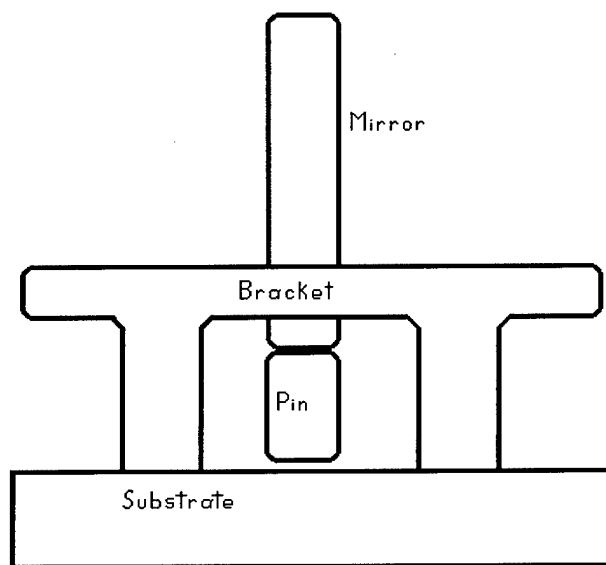


Figure 47. Cross Section of a MUMPS Hinge

reality the amount of space may be less than $4.75\ \mu\text{m}$ depending on how well the MUMPS process is controlled. Previous AFIT work has determined that the nominal hinge pin size is $3.5\ \mu\text{m}$ creating a $4.25\ \mu\text{m}$ diagonal.

Unfortunately, the nominal hinge pin size was not factored into the design of the AFIT MiG test structure. The hinge in Figure 45 has a hinge pin width of $4.5\ \mu\text{m}$ which was

larger than the nominal 3.5 μm and caused problems during release which will be discussed in Chapter 6.

5.2.3. MUMPS Latches Because the MUMPS process requires space to create working hinges, the MUMPS flip-up mirrors do not stay upright without added support. MUMPS latches provide the support for the test device. MUMPS latches consist of two parts, a Poly1 clasp, and a Poly2 pin. The clasp is connected to the main mirror forming one continuous structure. The clasp has a T-shaped hole where the pin is inserted and then locked down. The T-shaped hole has a narrow opening width of 7.5 μm and a T-top width of 10 μm . Figure 48 is the CADENCE layout of the MUMPS latch clasp. The latch pin can be constructed of Poly2 or Poly1-Poly2 stacked with a Poly2 tip. The latter design is a stronger design and is implemented in the test device. The tip of the pin is I-shaped, with the width of the I-beam, 5 μm , just smaller than the width of the T-beam on the clasp. The width of the top of the I, 9 μm , is also slightly smaller than the width of the top of the T. When the mirror is flipped up the I-tip of the pin is inserted into the T-hole in the clasp. When the mirror is fully erect the I-pin slides down into the T-clasp locking the mirror in place. The latch pin is 120 μm in length. The CADENCE layout of the latch pin is Figure 49.

There is still some movement allowed in the mirror caused by the fact that the T-clasp is larger than the I-pin. This difference in size between the components of the MUMPS clasp are needed to ensure proper operation. The amount of movement, however, is much smaller than the amount of movement allowed by the original hinge and is acceptable for the test device.

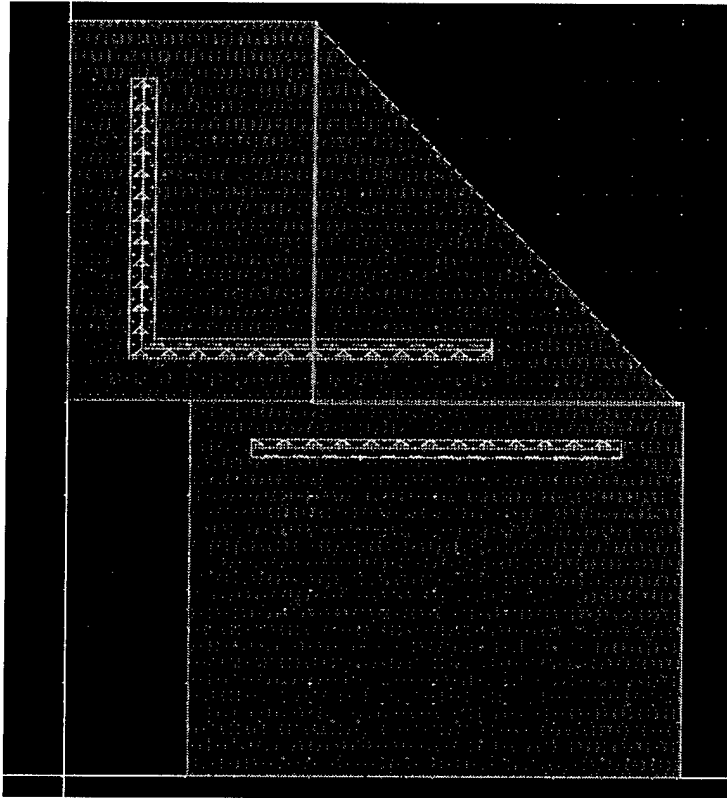


Figure 48. CADENCE Layout of MUMPS Latch Clasp

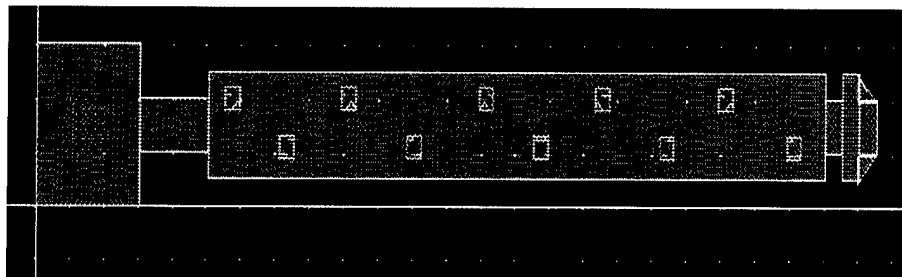


Figure 49. CADENCE Layout of Latch Pin

The dimensions of the latch are determined using the Pythagorean theorem. The length of the pin is designed to lock the clasp tightly in place when the mirror is erect. The latch pin forms the hypotenuse of a right triangle. The length of the pin is set so that when the mirror is flipped up the mirror is pulled tight to the front of the hinge.

5.2.4. MUMPS Mirror Plate The mirror plate is the part of the mirror that does the reflecting. The mirror plate is constructed of stacked Poly1 and Poly2 with gold. The Poly1-Poly2 stack is done by covering the majority of the Poly1 sheet with a Poly1_Poly2_via. The Poly1 and Poly2 sheets extend beyond the via. The gold is placed over the Poly2 leaving a band of Poly2 exposed at the edges. Holes are placed through the sheet at 30 μm intervals to allow for the release etch to etch underneath the mirror. The holes in the mirror do degrade from the reflecting characteristics of the mirror but are necessary to release the mirrors. Also, because the purpose of the test device was to show light propagation, the losses due to the etch holes are negligible.

The mirror plate has flaps on both sides. The reason for this shape is to include the MUMPS latches into the device while maximizing reflecting space. The flaps also allow for a more continuous mirror when more than one mirror is used on the device. The test design uses sets of three mirrors to maximize reflecting area. The mirror also has pegs sticking out of the top of the mirror plate. These pegs allow for easier construction of the mirror. These pegs are used in conjunction with “help flips,” (discussed in the next section) to keep the mirror off of the substrate. The mirror needs to be off of the substrate to flip it up during final assembly. The pegs are Poly2 extensions that cover the end of the help flips. With the additional mirror flaps the size of the mirror plate is approximately 200 μm \times 200 μm . Figure 50 shows the CADENCE layout of the finished mirror plate.

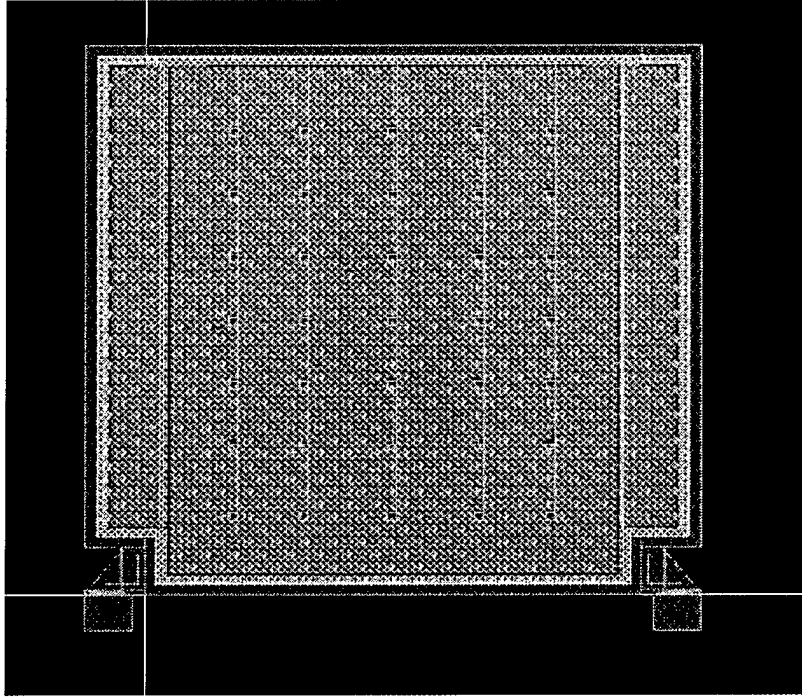


Figure 50. CADENCE Layout of MUMPS Mirror Plate

5.2.5. MUMPS Help Flip A MUMPS help flip is a cantilever beam placed near the edge of the mirror plate. The end of the help flip is under the pegs on the mirror plate discussed previously. The help flip cantilevers are constructed of stacked Poly1-Poly2 and gold. Poly2 and gold cantilevers provide a greater lift capability since these cantilevers have greater bend due to the residual stresses. However, for greater strength, stacked Poly1-Poly2 cantilevers are used. The longer the cantilever, the higher the deflection gets off of the surface. Because multiple mirrors are used, however, the size of the cantilever is limited to the length of the mirror.

One long cantilever could possibly lift the mirror into place by itself. While an attractive proposition, it is not a sure thing; thus two smaller cantilevers are used to keep the mirror plate above the substrate. These cantilevers have one end anchored to the

substrate, and the other end is free. The cantilevers were made $35\ \mu\text{m}$ long \times $5\ \mu\text{m}$ wide.

Figure 51 is the CADENCE layout of the help flips.

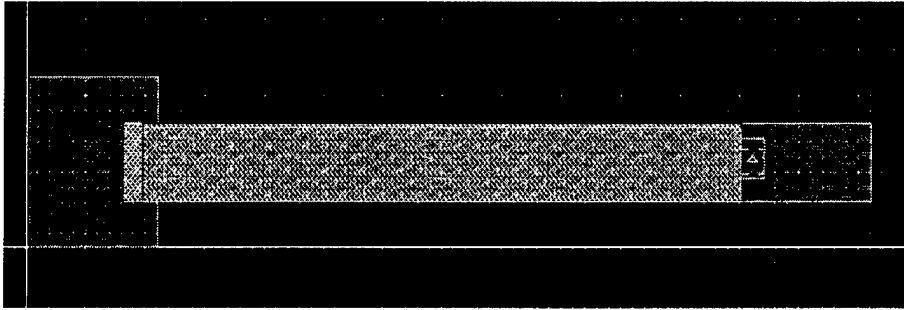


Figure 51. CADENCE Layout of MUMPS Help Flip

5.2.6. Final Mirror Design When all of the preceding components are put together the final mirror is formed. In reality, the Poly1 mirror plate, Poly1 latch clasp, and Poly1 hinge pin are one solid piece of material. The Poly2 areas are then fabricated

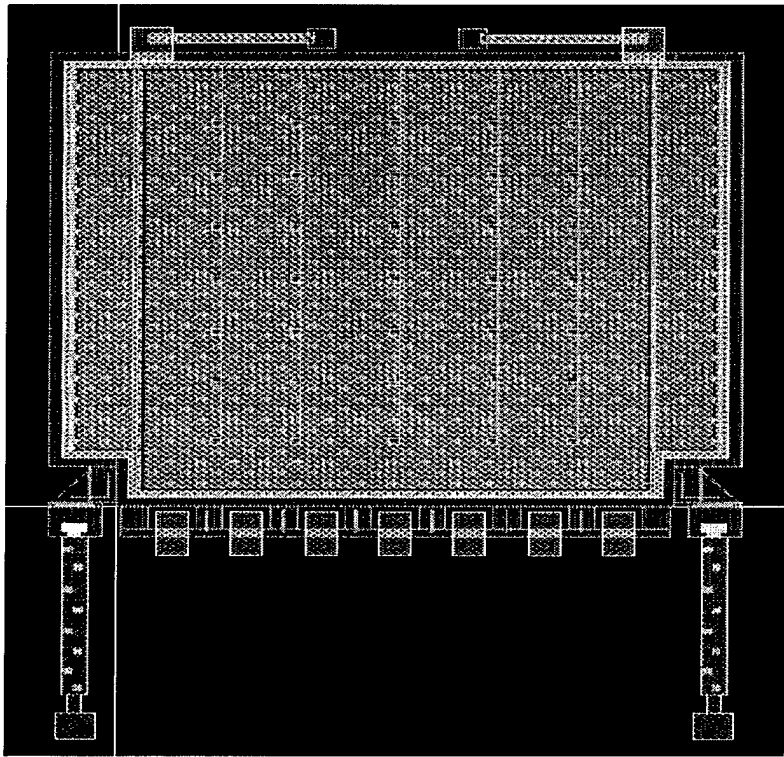


Figure 52. CADENCE Layout of Complete MUMPS Mirror

over the Poly1 structures, with the gold of course being placed last. The entire mirror structure takes up an area around $300\ \mu\text{m} \times 300\ \mu\text{m}$. Figure 52 is the CADENCE layout of the completed MUMPS mirror.

5.3. *MUMPS Bond Pads*

5.3.1. Overview On a MUMPS die bond pads are made of large areas of silicon and gold that form large solderable surfaces. Two different types of bond pads are used to make electrical connections on the AFIT MiG test device. The first type of pad, the power pad, is isolated from the substrate by the nitride layer. This type of pad is used to bring power to the laser and read the signal from the detector. The other type of pad, the ground pad, is electrically connected to the substrate. This makes the substrate a large ground to which all devices are grounded. This makes it possible to have only one ground connection for the entire device. There is a separate pad for each power connection and each signal wire. All wires from the bond pads to the devices are run using Poly0.

The power pads are also used to connect the laser and detector to the substrate. The pads are shaped to surround the devices creating areas where the devices can be soldered to the pads. Three such pads are used for the connection of the laser. These correspond with the laser design to create a flip-chip type connection. The detector used two pads, one to solder the front signal wire to, and the other for the ground. The pads are connected to the actual power power pad and ground pad through Poly0 wires.

5.3.2. Power Pad The MUMPS handbook [18] gives a design for a standard MUMPS bond pad. This standard design was used for both types of bond pads with a slight modification for the ground pad. The design is a stacked Poly0-Poly1-Poly2-gold with each additional layer getting progressively smaller as the layers are deposited. The progressive decrease in size of the layers is to prevent electrical isolation from occurring. Each layer provides a buffer when etching the layer above it preventing the etch from cutting off the electrical connection. The most important place for this is when Poly1 is placed on Poly0. If the Poly1 section were larger than the Poly0 section it is possible that due to Poly1 overetch the wires would become electrically isolated from the bond pad. Also, Anchor1 overetch could cut the connection, so the Anchor1 section must be smaller than the Poly1 section. The Poly1_Poly2_via is made inside the Poly1 area also; this is not as big of a concern but done for safety sake. The Poly2 is placed outside of the Poly1_Poly2_via both for corrugation and to ensure that the combine Poly-

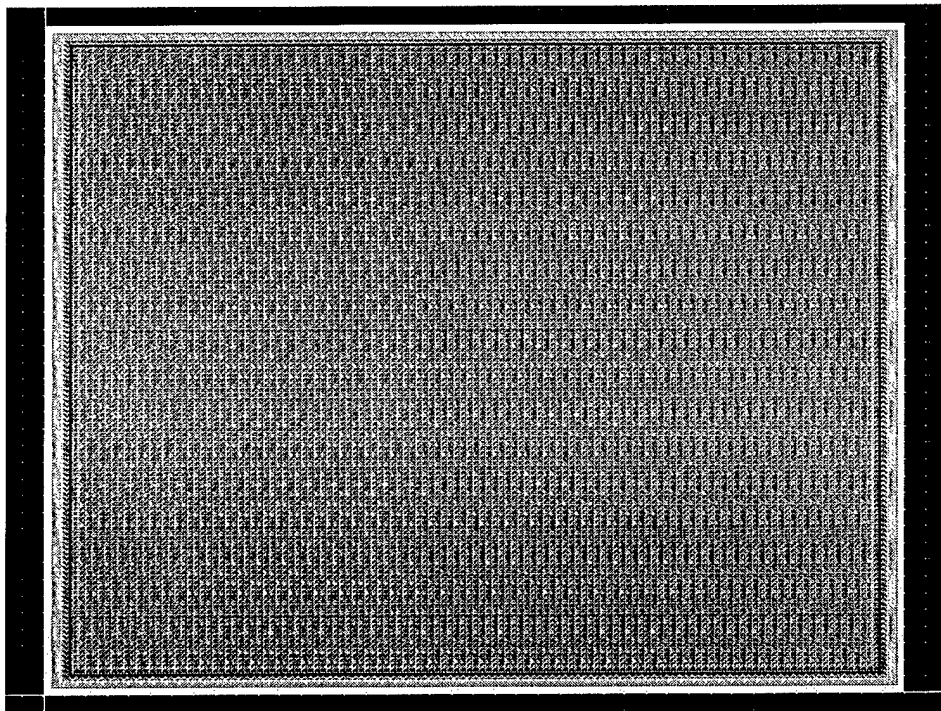


Figure 53. CADENCE Layout of The MUMPS Power Pad

Poly1_Poly2_via etch does not disrupt the electrical connection. The gold is again placed inside of the Poly2 area. The finished power pad is $400\ \mu\text{m} \times 400\ \mu\text{m}$. Figure 53 is the CADENCE layout of the power pad.

5.3.3. Ground Pad The ground pad is identical to the power pad except for one addition. To ground the ground pad to the substrate, Poly0 is not placed into the center of the pad. When the Anchor1 etch is performed, the nitride is breached, and the pad becomes electrically connected to the substrate. The other layers, Poly1 through gold, are built up as before. Once again the wires to connect to devices on the die are done in Poly0. The ground pads were also made $400\ \mu\text{m} \times 400\ \mu\text{m}$. Figure 54 is the CADENCE layout of the bond pad.

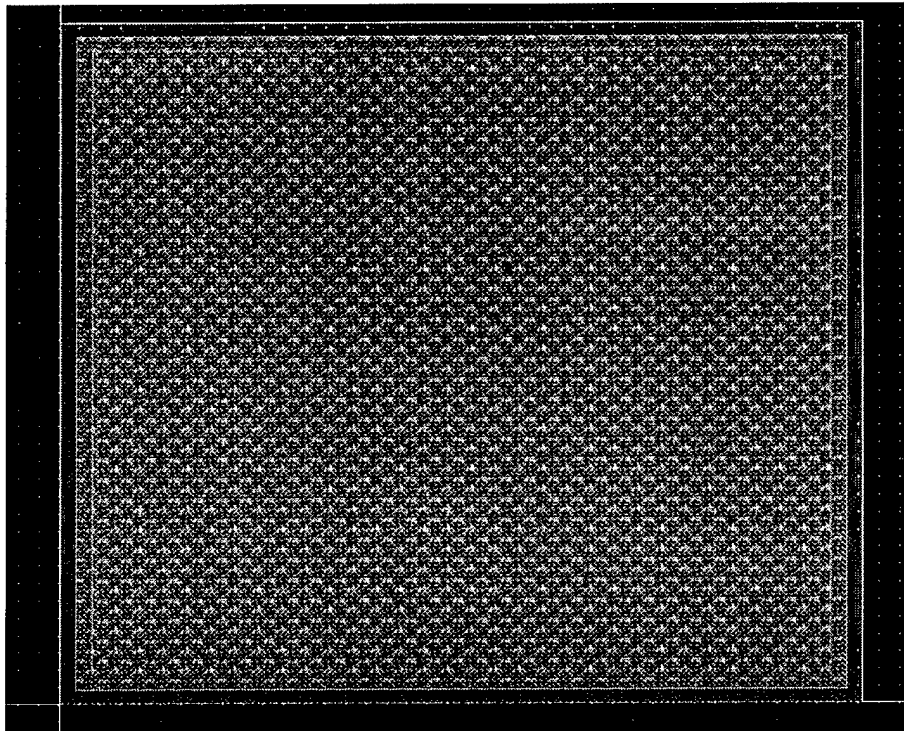


Figure 54. CADENCE Layout of MUPS Ground Pad

5.4. *MUMPS Octal Mirrors*

Octal mirrors were placed onto the final MUMPS submission to take up space. There is a lot of space on the MUMPS die that is left empty. AFIT has always had a policy of trying to use up as much die space as possible. It was in this spirit that two different sizes of octal mirrors were designed and placed on the die. The octal mirrors are intended to curl up once released. The mirrors are eight sided with four lever arms attached to four of the sides. These lever arms allow the mirrors to curl up while at the same time keep it anchored to the substrate. The mirrors are stacked Poly1-Poly2-gold. The lever arms are Poly1 anchored to the nitride. Poly0 is not used in the devices. The two sizes are based on the sides where the lever arms are attached. The two sizes are 50 μm and 100 μm .

Figure 55 is the CADENCE layout of the 100 μm mirror.

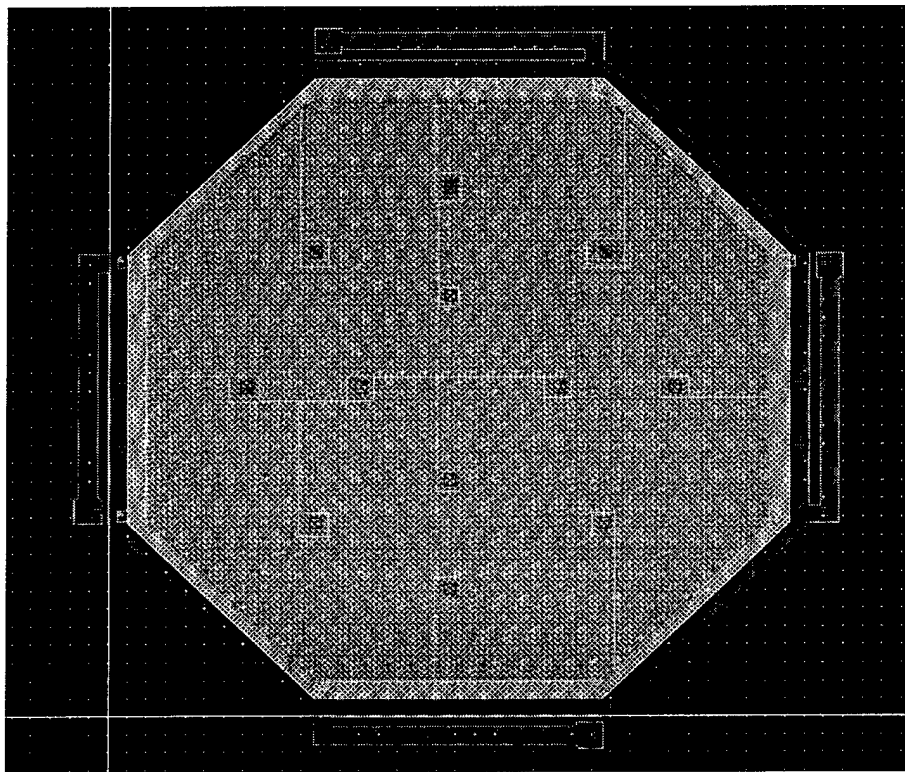


Figure 55. CADENCE Layout of Large Octal Mirror

5.5. *Summary*

The test structures were built to show that laser light could be propagated around an open loop MEMS interferometer. MUMPS was used because it is an available process and can be fairly reliable if the design limits are followed. After the devices are fabricated they must be released, assembled, and tested. Chapter 6 discusses the release, assembly, test results, and analysis of the results for the test structures discussed in this Chapter.

6 *Laser Light Propagation Device Testing and Results*

6.1. *MUMPS Processing*

MEMS research devices usually require some form of manual assembly. The assembly may entail powering devices such as thermal actuators on the device to perform assembly, or for the case of the AFIT MiG test device, actual physical assembly. This assembly seems to negate the possibility of mass production of MEMS devices due to the labor involved. If the devices tested were the finished products, this might be true. In the case of the AFIT MiG, however, the envisioned final product will not require the same assembly as the test device. Never the less, the test device requires physical assembly as detailed below.

6.2. *Release Procedure*

When the MUMPS dice are shipped to the user they still have all the oxides present and have also been coated with a thick layer of photoresist for protection. To prepare the die for operation, or in MEMS terminology to “release” them, the photoresist must be stripped and then the oxides removed.

6.2.1. *Photoresist Removal* Since the photoresist has not been developed, it is still soft which makes release easier. Removal of the photoresist is done using acetone. Two different acetone baths are used. The first acetone bath removes the bulk of the photoresist. MUMPS dice are placed in the first acetone bath for 5 to 10 minutes. The second acetone bath removes any residual photoresist left on the die. MUMPS dice are left in the second acetone bath for 5 to 10 minutes. The amount of time the dice remain in the acetone baths is not exact and in fact the longer they remain, the less chance any

photoresist will be left on the die. The acetone does not harm the underlying silicon, polysilicon, gold, or nitrides of the device.

After the photoresist is removed the dice are placed in a methanol bath for 5 to 10 minutes. The methanol bath removes the acetone from the dice. When the dice are removed from the methanol they are placed on a 55° C hot plate for up to 5 minutes. The hot plate evaporates the methanol from the dice leaving dry dice for etching

6.2.2. Oxide Removal The three sacrificial layers in the MUMPS process are deposited silicon dioxide layers. To create working devices these oxide layers must be removed. Oxide is removed using an acid etch. Different acids will etch the polysilicon, silicon, and silicon dioxide at different rates. For this process an etch that quickly etches silicon dioxide while not quickly etching polysilicon and silicon is needed. Concentrated hydrofluoric acid, HF (49%), etches silicon oxide at rates from 18k to 23k Å/min while etching polysilicon and silicon at a much lesser rate [20, 33].

To remove the oxides the MUMPS dice are placed in concentrated HF for 2.5 min. The dice are then placed in a methanol bath for 5 to 10 min. The first methanol bath removes most of the acid from the dice. A second methanol bath is used to remove the remainder of the acid. MUMPS dice are left in the second methanol bath for 15 to 20 min. The longer the dice are left in the methanol baths the more acid, and more importantly water, is removed from the dice and the better the release. Water causes “stiction” to occur in MUMPS devices. Methanol evaporates quickly and does not have as large a meniscus as water does. Because of the lower meniscus the methanol does not pull the MEMS structures toward the die surface as much as water does. After the alcohol baths the dice are placed on a 55° C hot plate for 5 to 10 min.

The release of MUMPS dice should be done in a clean environment so that dust and other particles do not interfere with the operation of the device. Optimally the release would be done inside a clean room. The dice would be packaged in the clean environment and sealed so that they would always operate in a clean environment. The AFIT Cooperative Engineering Materials labs, however, do not provide the cleanest of environments. Fortunately, for the AFIT MiG test devices, the absolute sterility of the environment is not a factor and the facilities used proved adequate.

Table 6 is a summary of the release procedure used.

Table 6. Release Procedure

Procedure	Time in min
1st Acetone Bath: Bulk Photoresist Removal	5-10
2nd Acetone Bath: Residual Photoresist Removal	5-10
1st Methanol Bath	5-10
Hot Plate Bake @ 55° C	≤ 5
Concentrated HF (49%): Oxide Removal	2.5-3
1st Methanol Bath: Main Acid Removal	5-10
2nd Methanol Bath: Residual Acid Removal	15-20
Hot Plate Bake @ 55° C	≤ 5

6.3. Device Assembly

After the AFIT MiG test devices have been release they must be assembled. The mirrors arrive flat on the substrate and must be flipped up. Figure 56 shows a section of MUMPS mirrors on the substrate of the device. Each of the mirrors are 200 μm × 200 μm in area. The picture is at a magnification of 97 × actual size. When the mirrors are flipped up they

appear as in Figure 57. These mirrors in this image have been magnified $160\times$ actual size. The mirrors are flipped up using a microprobe.

Figure 58 is a sketch of the microprobe. The microprobe has controls for three degrees of freedom. The controls shown on the probe move the tip of the device in the X, Y, and Z directions. To flip the mirrors the tip of the probe is placed in front of the mirror and slid under the mirror. The tip is then moved forward and up, lifting the mirror into place. Care must be taken not to break the mirrors, as they are fragile. When the mirror is flipped up, the lock on the mirror is engaged. Figure 59 shows the mirror locking mechanism engaged. This figure is at a magnification $310\times$ actual size. Note that a problem may occur since the mirrors may not be at 90° with respect to the substrate because of the inherent slop of the MUMPS hinge. Figure 60 shows bond pads for a laser and detector. The pads in Figure 60 are shown at $55.5\times$ actual size.

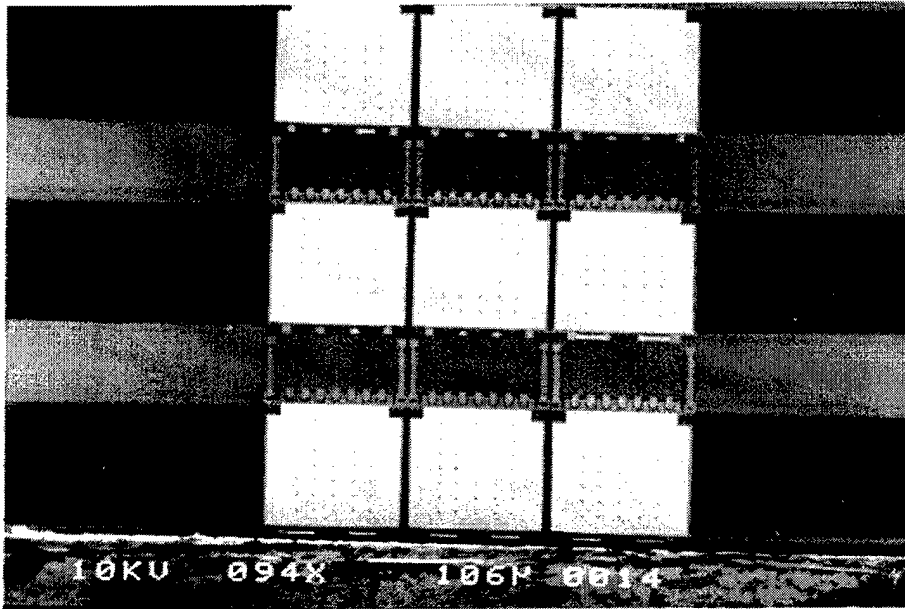


Figure 56. Unassembled MUMPS Mirrors

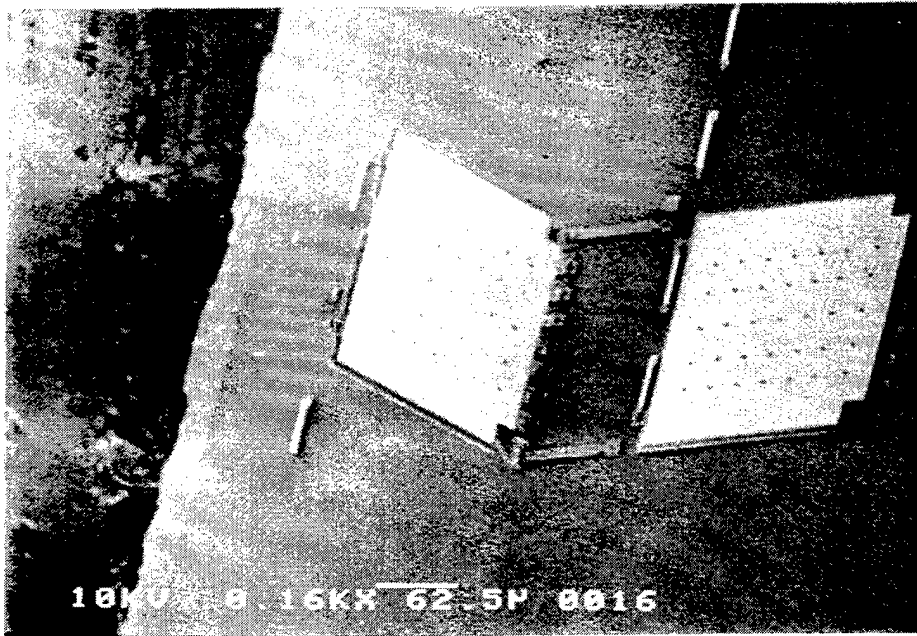


Figure 57. Assembled MUMPS Mirrors



Figure 58. Microprobe

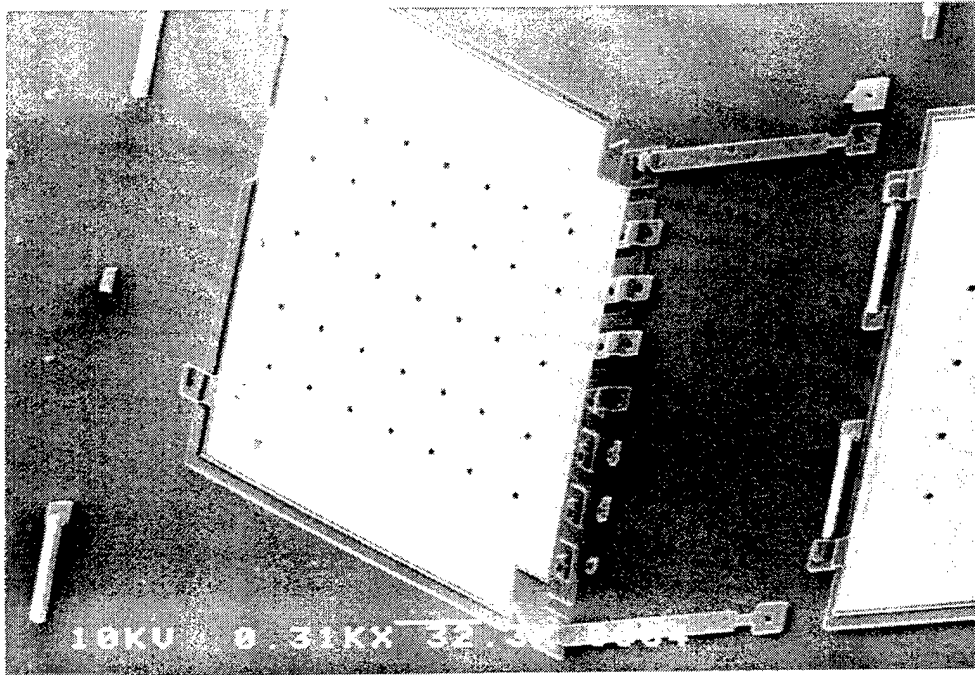


Figure 59. Mirror With Locking Mechanism

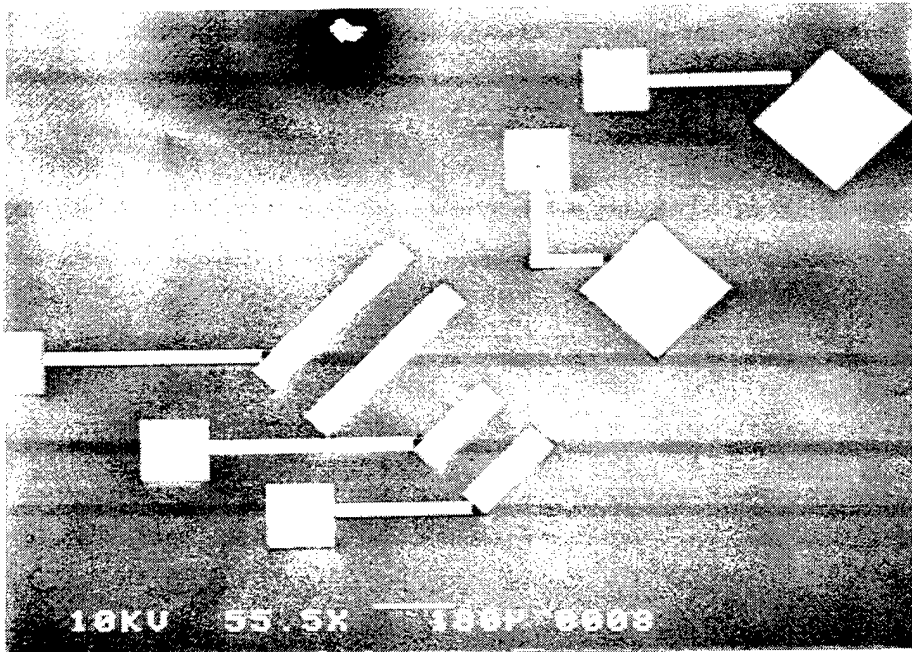


Figure 60. MUMPS Bond Pads

Unfortunately, for this research, the laser detectors were not received in time, therefore the lasers and detectors were not mounted on the die and an alternate method for testing had to be employed. The lasers were not mounted to ensure they would not interfere with the ad-hoc testing method used. Nominally the laser and detector would be placed onto the pads shown in Figure 60. To operate the lasers, probe tips would make contact with the bond pads and deliver the required power.

6.4. Hinge Failure

During the flipping of the first set of mirrors, it became apparent that a problem existed with the design of the mirror hinges. Each time a mirror was flipped up, it broke off of the hinge. The break point usually occurred when the mirror was $\geq 45^\circ$.

The reason for the mirror failure was discovered upon reviewing the design file for the AFIT MiG test device. Recall from Chapter 5 that the nominal hinge pin size was $3.5 \mu\text{m}$ due to the limited space allowed from the MUMPS process. Test device hinge pins were $4.5 \mu\text{m}$ in thickness. Thus, when each mirror was flipped up, the hinge pin would get wedged against the hinge, preventing the mirror from being fully deployed at a 90° angle. Figure 61 is a close-up of a MUMPS hinge to show the hinge pins and brackets. This hinge bracket is $12 \mu\text{m}$ wide. The image is at $3100 \times$ actual size.

6.4.1. Hinge Fix 1 To overcome the problem of large hinge pins two solutions were proposed. The first solution was to leave the die in the release etch for a long period of time. The HF would eventually etch away some of the excess silicon off the hinge pin and hinge bracket leaving enough room to flip up the mirror. Etch times were increased first to 4 min, then from 4 min to 7.5 min in 1 or 0.5 min steps. After a series

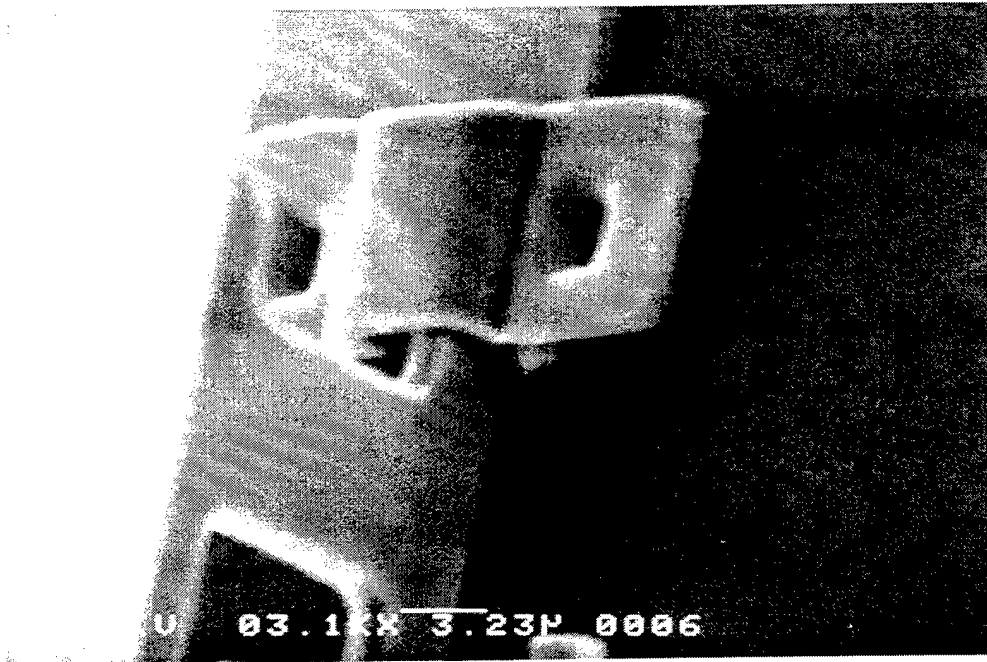


Figure 61. MUMPS Hinge Close-up

of etch tests the yield of mirrors increased resulting in a nominal etch time of 5 min. An etch time of 5 min allowed enough mirrors to be flipped up to allow testing. Below 5 min there was not enough space in the hinge and the mirrors would break off of the hinge as before. At greater than 5 minutes the polysilicon became too weak, and the hinge brackets would just be ripped off of the die.

However, the process was not reliable. Mirrors still broke off of their hinges and others were too weak and failed by other means. After repeated attempts, enough mirrors were flipped up to test the device. Figure 62 shows a flipped up mirror hinge. Notice the broken parts of the hinge. Figure 62 is at 140 \times actual size. Further information on the actual testing of the device and what is meant by enough mirrors is found in section 6.5.

6.4.2. Hinge Fix 2 The second method used to increase the mirror yield attempted to overcome the hinge pin problem by using a weak silicon polishing etch. HNA, a 1:3:8 ratio mixture of HF, HNO₃, and acetic acid, gives polysilicon etch rates of 0.7 to 3 $\mu\text{m}/\text{min}$ [20, 33]. By diluting the etch with de-ionized (DI) water the etch rates can be more closely controlled. The HNA was mixed with 10 ml HF, 30 ml HNO₃, 80 ml acetic acid, and 100 ml DI water. The etch was first performed for 15 sec. This etch rate was too long causing all of the mirrors to be etched from the die. Etch times of 2.5 sec, 5 sec, and 10 sec were then tried. The 5 sec and 10 sec etch times were too long causing the polysilicon to be weakened to a point where the mirror either came right off of the die or was shattered from touching it with the probe. A final etch time of 2.5 sec was used. This etch time allowed for a greater mirror yield than the 5 min HF over etch.

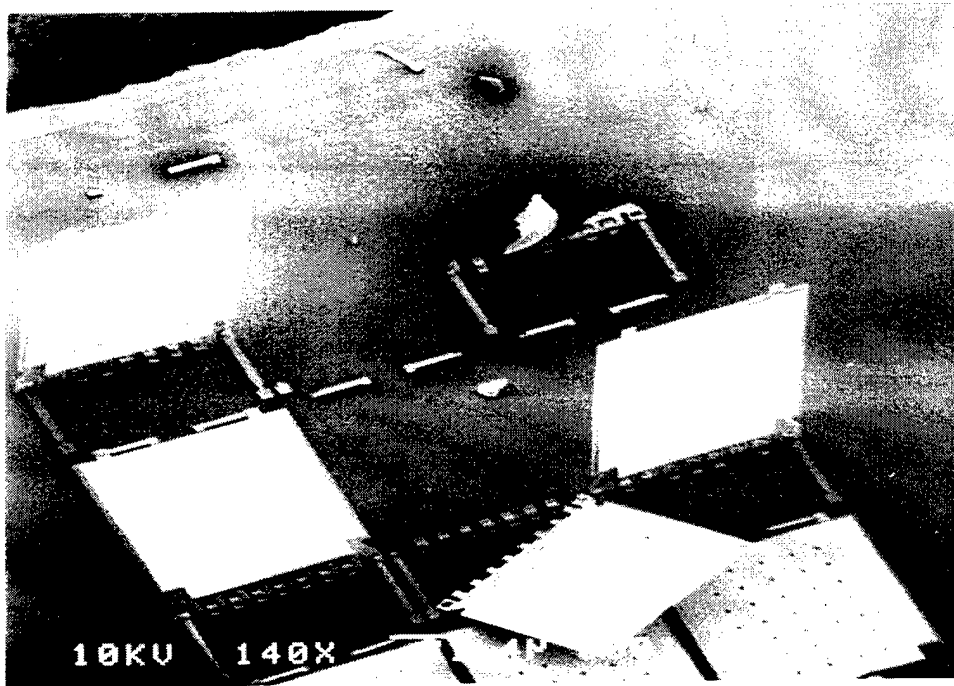


Figure 62. MUMS Mirror With Broken Hinge

As with the extended HF etch, the HNA etch provided enough mirrors to test the device, but problems were still encountered. Mirrors still broke off of the hinge pins and others tore the hinge brackets from the die. Therefore, to obtain working devices, the design needs to be changed and another MUMPS run performed. Figure 63 shows a MUMPS hinge with a broken hinge bracket. The hinge in Figure 63 has been magnified 1000 ×, the actual hinge pins are 12 μ wide and 22.5 μm long.

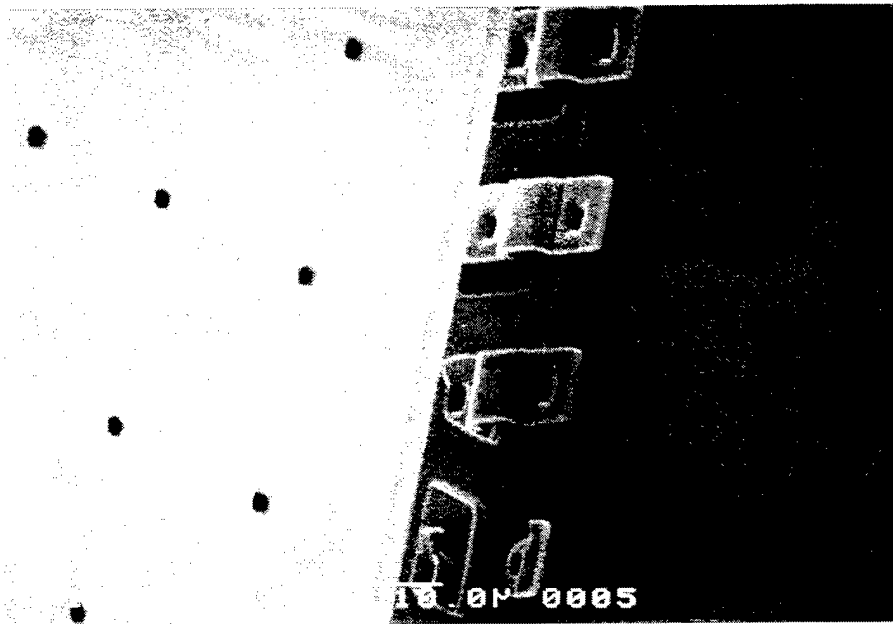


Figure 63. Hinge With Broken Bracket

6.5. Device Testing

Since photodiodes were not available for mounting, an alternate method of testing was derived. The testing method used a red (around 780 nm wavelength) visible laser pointer with power output of < 0.25 mW, and a white background. The laser pointer was aimed at the device and the light was propagated around the mirrors. A white background was placed in the light path to catch the light and determine if the test was successful.

In order to test the light propagation multiple mirrors had to be flipped up in different locations around the die. Due to the inadequate design of the AFIT MiG test device, it was determined that two mirrors in adjacent sites as shown in Figure 64 would be adequate to test the concept. The Xs in Figure 64 show where the mirrors need to be in reference to each other for testing. The determination was based on the number of mirrors required to determine whether light was propagating around the interferometer or just reflecting out of the interferometer and being collected. Three corners of the square would be preferred for greater testing. With three corners testing could determine if light could propagate completely around the square. The two mirror case was obtained using the 5 min over etch process. Later the three mirror case was obtained using the HNA polishing etch.

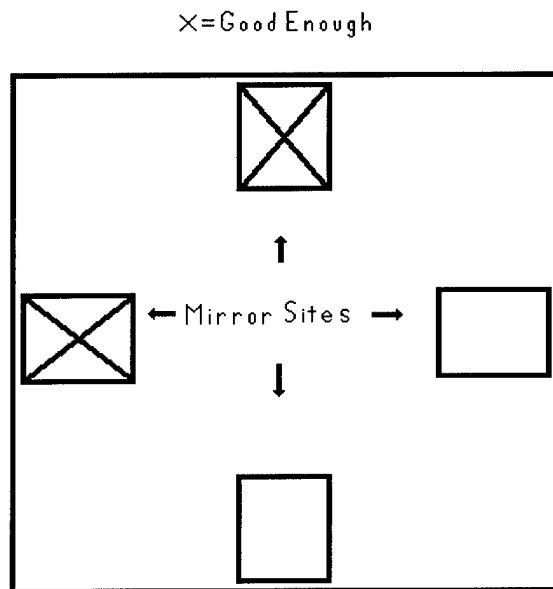


Figure 64. MUMPS Mirror Sites

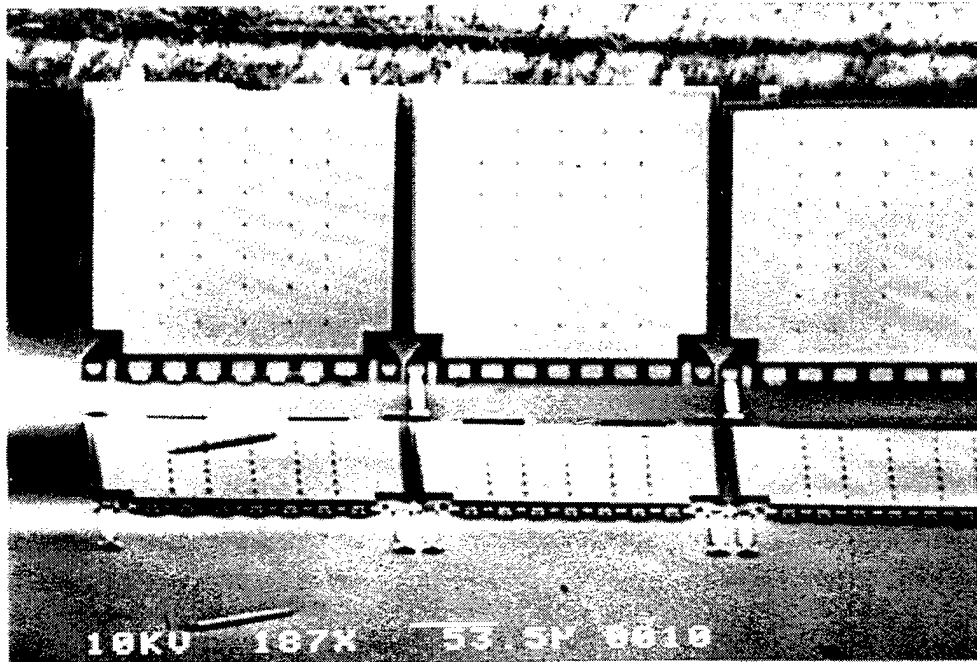


Figure 65. Multiple MUMPS Mirrors

Ideally in each location three mirrors would be flipped up next to each other as shown in Figure 65. Due to the mirror failures this happened at only one site using the HNA etch. Figure 65 is at a magnification $187 \times$ actual size.

Laser light was then shown to propagate around first two then three mirrors on the interferometer. The experiment was successful despite the complications. Laser light was propagated around an open loop interferometer. This is a required element of the AFIT MiG operation. That this is possible warrants further experimentation of the AFIT MiG idea.

This experiment used a low energy source that was not contained and poorly aligned with the mirrors. In the actual AFIT MiG a higher power laser would be used and it would be properly aligned with the mirrors of the interferometer. A fair amount of power should then be available at the photodetector of the AFIT MiG. The exact amount of

power required at the detector of the AFIT MiG is not known. It is hoped that this “fair” amount of power would be adequate.

6.6. *Octal Mirrors*

The octal mirrors placed on the device became a good indicator of proper etch time. The octal mirrors, shown in Figure 66, were more loosely attached to the substrate and so were etched off of the die with etch times greater than 4 min. The mirrors in Figure 66 have been magnified 400 × their actual size.

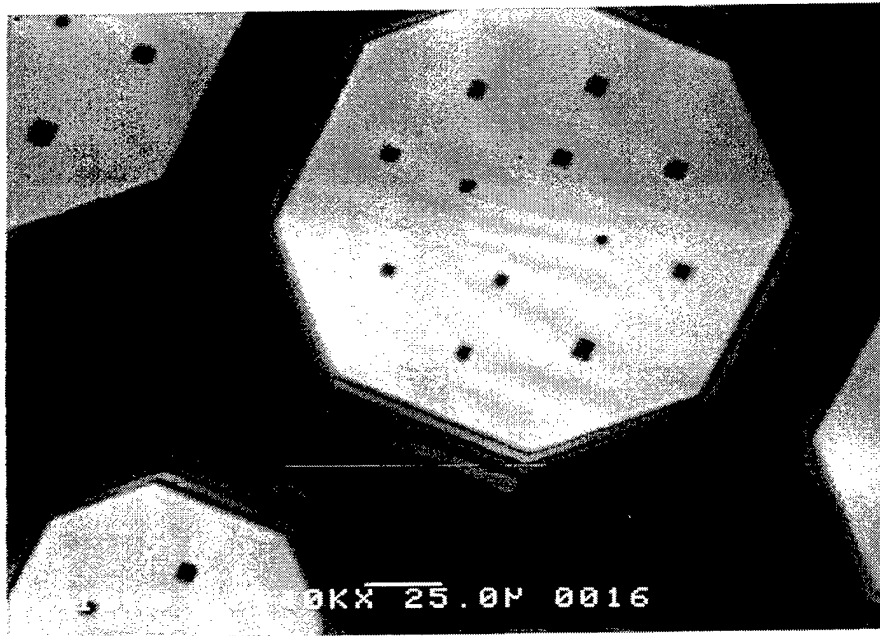


Figure 66. Octal Mirrors

6.7. *Summary*

A design flaw in the AFIT MiG test device created considerable problems during the assembly of the device. These assembly problems in turn led to complications during the actual testing of the device. Further complications occurred since the photodetectors were not available. Thus, an alternate testing method had to be implemented. An ad hoc

(improvised, impromptu) method employing a laser pointer was used and the tests were successful.

The AFIT MiG test device proved the concept that a laser beam can be propagated around an open loop MEMS interferometer and collected at the end of the interferometer. The AFIT MiG will be a more complex design and will use better components to sense rotation rates.

Chapter 7 provides a summary of the entire research and then discusses follow on work to the research. This initial AFIT MiG design is just the beginning. Different techniques can be employed to manufacture the actual device and further sensing research can be done.

7 *Conclusions and Recommendations*

7.1 *Conclusions*

There were two main parts to this research. The first part involved simulating the AFIT MiG using MATLAB [25]. The second part involved proving that laser light could be propagated around an open loop interferometer.

The MATLAB simulations of Chapter 4 show that theoretically the AFIT MiG can sense rotation rates generated by different aircraft types. Of the aircraft simulated, the C-12 was the least agile and the simulated AFIT MiG was able sense the rotation rates generated by the C-12's maneuvers.

Simulations also showed that making the AFIT MiG non-reciprocal had little to no effect on the simulated performance. The simulated sensitivities for AFIT MiG designs with different optical path lengths had reciprocal and non-reciprocal outputs that were indistinguishable.

The total length of the optical path length did have an impact on the simulated performance of the AFIT MiG. As the number of optical legs, and the total optical path length increased, so did the sensitivity of the simulated AFIT MiG. It was shown that as the number of optical legs increases, the effect of each additional leg becomes less and less. Therefore, there is a tradeoff between the actual performance increase and the complexity increase due to adding an optical leg.

It was also shown that the wavelength of laser light used had an impact on the sensitivity of the simulated AFIT MiG. The smaller the wavelength the greater the simulated sensitivity. It is thus beneficial to use small wavelength lasers when building

an actual AFIT MiG. Remember though, that the smaller the wavelength the smaller the region of operation of the simulated AFIT MiG.

When the light propagation test device was fabricated problems occurred. Do to a design flaw the mirrors did not flip up properly. Eventually an ad hoc testing method was applied and light was propagated around an open loop MEMS interferometer. This proved that it was possible to propagate light around an open loop MEMS interferometer, a necessary component of the AFIT MiG.

7.2. Further Research Recommendations

The research discussed here is just a beginning. Further research needs to be done to bring the AFIT MiG out of its infancy. It could be that there are better ways to configure the mirrors of the AFIT MiG. Optics can be used to evaluate the best way to configure the AFIT MiG. Direct continuation of this research should concentrate on the fabrication of the AFIT MiG.

7.2.1. Micromachining Techniques At the time of this writing, MUMPS was the only process available to AFIT for the construction of the devices. MUMPS, however, is not an adequate process for construction of the AFIT MiG as currently envisioned. To fabricate the AFIT MiG in MUMPS requires using flip up mirrors. Flip up mirrors are not stable. Large movements of the mirrors in an interferometer would disrupt the interference of the laser beams at the photodetector. On a Sagnac interferometer rotation would cause constant movements of the mirrors. This constant movement would cause a constant disruption that would continually shift the phase difference at the detector so that output due to rotation is no longer discernible from noise caused by mirror movement.

MUMPS mirrors are also fragile. The end product of the AFIT MiG is a gyroscope to be used in both aircraft and expendable vehicles. The devices may be subject to large G-forces and shocks. Mirrors used on the AFIT MiG need to be robust and capable of withstanding shocks and large G-forces.

Along the lines of creating stable mirrors, research needs to be done using other processes to form the AFIT MiG. One possibility and the one envisioned during this research is the use of a LIGA or similar process to form the mirrors. Some universities and businesses are doing LIGA. The main problem with LIGA is the cost. Funding would need to be obtained and a LIGA run submitted.

Another method could involve bulk micromachining. Interferometers formed out of a bulk silicon substrate would be stable and robust. Vertical mirrors could be formed using an anisotropic etch. The mask structure and alignment would have to be researched to determine optimal placement.

The research presented thus far has relied on silicon micromachining. The realm of MEMS is expanding and new fabrication techniques are being developed. It may be that a new technique, or technique not discussed in this research will provide the best means of fabricating a working AFIT MiG.

7.2.2. Sensing of The AFIT MiG An investigation of how the information obtained from the AFIT MiG will be processed and used is required. This research should consider the piezoelectric actuation of the mirrors to bias the gyroscope at the maximum sensitivity. The signal from the gyroscope is a voltage from the photodetector that corresponds to the rotation applied. Possibly this information could be digitized and Digital Signal Processing (DSP) used to process the information and determine the actual

rotation. Other methods of information processing might be more appropriate and could be researched.

7.2.3. Powering The AFIT MiG New advances in power cells are leading to new methods of powering devices. Power cells in MEMS are also an area of research. Power cell MEMS could be built into the AFIT MiG to make the device self-sufficient. This research would concentrate on integrating the power cell MEMS with the AFIT MiG.

7.2.4. Mirror Phase Shifts and Losses Different mediums propagate and reflect light differently. When a laser beam is incident upon a mirror one of three things can happen to the light. The light can propagate through the mirror, the mirror can reflect the light, or the mirror can absorb the light. If the light is propagated through the mirror or reflected off of the mirror it will undergo a phase shift. Research needs to be done to determine the effects of the light reflecting off of the mirrors in the open loop interferometer. Questions about how does the phase shift affect the AFIT MiG performance, and how much energy is lost at each mirror need to be answered.

Appendix A. The Sagnac Effect

The Sagnac effect, which states that “an optical path length difference is experienced by light beams propagating along opposite directions in a rotating frame,” is the fundamental theory behind all optical gyroscopes [23]. This optical path length difference is directly proportional to the absolute rotation of the rotating frame. Through measurement of this optical path length difference the rotation is determined in all optical gyroscopes. G. Sagnac, for whom the theory is named, “first demonstrated the sensing of inertial rotation by means of optical interferometry in 1913 [6].”

Figure 67 is a simple interferometer of the type Sagnac used in 1913 to first determine the Sagnac effect. The interferometer consists of a beam splitter and four mirrors. Light enters the interferometer through the beam splitter where the light is broken into two counter rotating beams. The beams then propagate around the interferometer and are

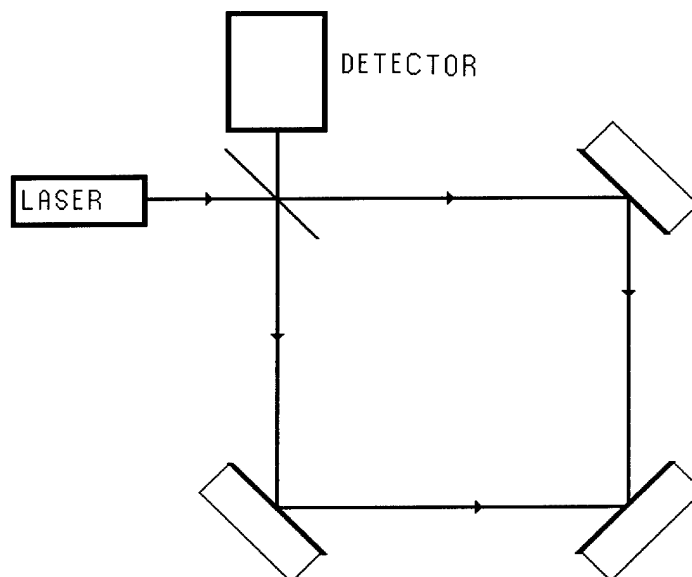


Figure 67. Sagnac Interferometer

recombined at the splitter. When the device is rotated the counter rotating beams experience different path lengths. This difference is sensed and the rotation determined.

For a circular interferometer the Sagnac effect is given by:

$$\Delta L = \frac{4\vec{A}}{c_0} \vec{\Omega} \quad (\text{meters}) \quad (29)$$

In this equation A is the area vector of the interferometer, c_0 is the speed of light in a vacuum and Ω is the rotation vector in rad/sec. The resulting ΔL is the optical path length difference that results. Rigorous derivation of this equation is “based on the propagation of light in a rotating frame where in general the theory of relativity must be used to perform the exact calculation [6].” For illustration a simpler method will be used for explanation.

To begin this discussion, consider Figure 68. This is a circular interferometer with radius R , and point S . When there is no rotation two photons leave S traveling in opposite directions. Both photons arrive back at S at the exact same time given by $t = 2\pi R/c_0$, where $2\pi R$ is the distance the photons travel around the circumference of the interferometer. Next consider the rotation interferometer of Figure 69. The photons again travel around the interferometer, however, because the interferometer is moving, so is the starting point. The point S , where the photons start from and where the photodetector is located, has rotated to point S' . Because of this motion the clockwise rotating photon travels a shorter distance back to the starting point than the

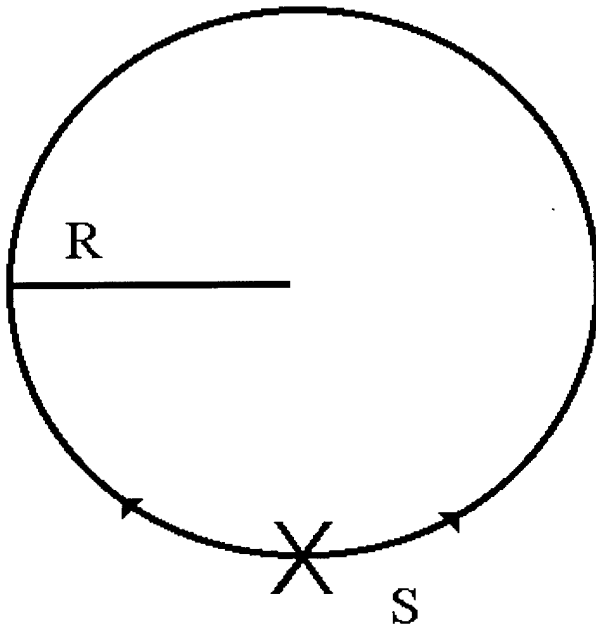


Figure 68. Circular Interferometer

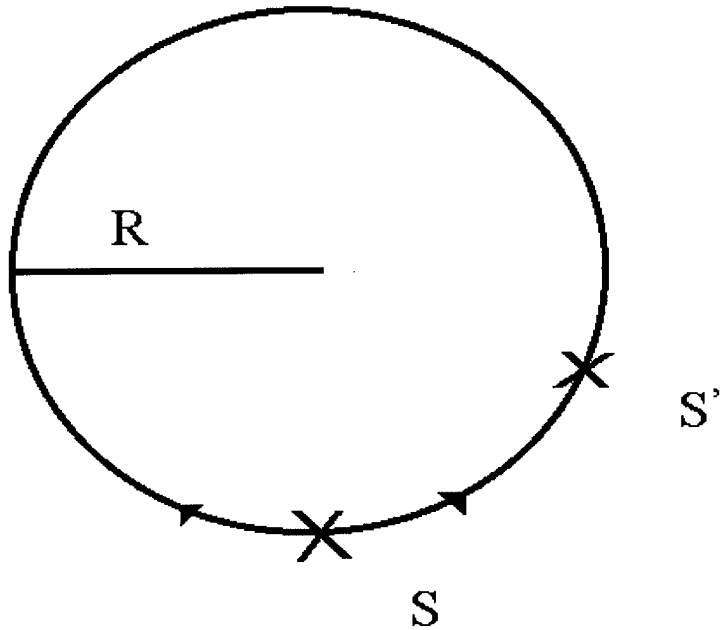


Figure 69. Rotated Circular Interferometer

counterclockwise rotating photon. The distance the counterclockwise rotating photon covered is given by:

$$L_{ccw} = 2\pi R + R\Omega t_{ccw} = c_{ccw} t_{ccw} \quad (30)$$

This equation states that the length the counterclockwise photon travels is less than the perimeter (circumference) of the interferometer by a distance equal to the tangential velocity of the photon, $R\Omega$ multiplied by the time it took the photon to travel L_{ccw} , t_{ccw} . In addition this length is also equivalent to the speed of the photon, c_{ccw} multiplied by the time of propagation. In a vacuum $c_{ccw} = c_o$. In the same manner the photons propagating in the cw direction will arrive at the starting point, now located at S'. The distance the cw photons traveled is given by

$$L_{cw} = 2\pi R - R\Omega t_{cw} \quad (31)$$

where t_{cw} is the time taken to cover the distance L_{cw} , and again $c_{cw} = c_o$ for propagation in a vacuum.

Solving Equation (30) and Equation (31) for t_{cw} and t_{ccw} respectively, and subtracting gives:

$$t_{cw} - t_{ccw} = \frac{2\pi R}{c_o - R\Omega} - \frac{2\pi R}{c_o + R\Omega} \quad (32)$$

$$t_{cw} - t_{ccw} = \frac{4\pi R^2}{c_o^2 - (R\Omega)^2} \Omega \quad (33)$$

In the denominator of Equation 33 the square of c_o is much greater than the square of $R\Omega$, from this we get:

$$\Delta t = t_{cw} - t_{ccw} \approx \frac{4\bar{A}}{c_o^2} \bar{\Omega} \quad (34)$$

The path length difference ΔL caused by the rotation is therefore:

$$\Delta L = c_o \Delta t = \frac{4\bar{A}}{c_o} \bar{\Omega} \quad (35)$$

which is identical to Equation (29).

For an alternative way of thinking about the Sagnac effect first transform equation (29) into a different form:

$$\Delta\phi_R = \omega \cdot \Delta t = \frac{4\omega\bar{A}}{c_o^2} \bar{\Omega} \quad (36)$$

where $\Delta\phi_R$ is the phase difference between the two beams caused by rotation. The angular frequency of the light used is ω . This result is very general and can be extended to any axis of rotation and any enclosed path even if they are not contained in a plane [6]. Such an extension is made by considering the scalar product $\mathbf{A} \bullet \boldsymbol{\Omega}$ where the bold denotes vector quantities. The area vector \mathbf{A} can be defined by the line integral:

$$\bar{\mathbf{A}} = \frac{1}{2} \oint \bar{\mathbf{r}} \times d\bar{\mathbf{r}} \quad (37)$$

Now the Sagnac effect is represented by the flux of the rotation vector through the enclosed area given by the flux integral $\mathbf{A} \bullet \boldsymbol{\Omega}$.

The last thing of interest regarding the Sagnac effect is the question of how large it is. For a basic feel consider an area of 100 cm². A rotation rate of 1 rad/sec would give a ΔL of 1.3×10^{-8} cm. A rotation of 1 rad/hr would give $\Delta L = 3.7 \times 10^{-12}$ [23]. Navigation grade performance requires an accuracy of better than 0.01 deg/hr or 4.8×10^{-8} rad/sec. Such would require an ΔL of less than 1.0×10^{-15} cm [23]. This is a very small distance even

when compared with dimensions such as the diameter of a Hydrogen atom, which is about 10^{-8} cm [24]. Even so with controlled processes such detection is possible.

Appendix B. LASERS

LASER is an acronym that stands for light amplification by stimulated emission of radiation. It is the high coherency of lasers that make them the optimal light source for use in optical gyroscopes. Coherent light is light that is monochromatic, highly directional, and highly polarized. If a light source in an optical gyroscope is not monochromatic the different wavelengths begin to interfere and resolution is lost. The light must be highly directional so that it can be propagated around an interferometer allowing for the maximum energy possible to be available at the detector.

More importantly for optical gyroscopes, the light must be of continuous phase. There can be no jumps in the phase or detection capability is lost. The reason is that phase is the means of acquiring the rotation information. Any phase shift is a rotation. If the phase suddenly shifts in the light it will be interpreted as a rotation. Only if the light is continuous in phase is detection possible. In reality no laser can maintain continuous phase indefinitely. The phase, however, is continuous for long periods of time and when the phase shifts it remains at the new phase for a long period of time. If the phase is continuous for a greater time period than it takes the laser beam to propagate around the interferometer, than the beams will interfere with zero phase difference in the condition of no interference. There will be brief periods of interference when the laser shifts phase, but these will only cause instants in time when the rotation information is not available. If the laser is of high quality these instants will be few and far between.

To understand why this is true the operation of lasers will now be briefly explained. For a laser to operate three fundamental conditions are required. The first component of

lasing is a population inversion. Quantum physics states that electrons exist at quantized energy states in atoms. As atoms interact with other atoms of the same type these energy levels become energy bands, as more spaces are needed to allow for the greater number of electrons. In these bands the electrons naturally gravitate to the lowest available energy states. If, however, energy equal to the energy difference between electron bands is imparted into the system electrons will be excited to the higher levels. These excited electrons stay in these higher states for only a short while. When the energy is released it can either dissipate into the lattice or be released as a photon with energy

$$E = E_2 - E_1 = \frac{hc}{\lambda} \quad (38)$$

where E_1 and E_2 are the energies of the corresponding energy bands, h is Planck's constant, λ is the wavelength of the light emitted, and c is the speed of light in a vacuum. The wavelength of the laser light emitted from a laser is thus dependent upon the energy levels in the material. In equilibrium most electrons are in the lowest energy states with a few in higher states that soon lose the energy and return to a lower state. If, however, enough energy is imparted into a system, the majority of electrons enter higher energy states. When a greater percentage of electrons are in higher energy states the condition is called a population inversion.

When a photon interacts with a material in which there is a population inversion it may stimulate the emission of another photon from the surrounding atoms. When this occurs the stimulated photon has the same phase and possibly the same direction as the stimulating photon. If the photon interacts with a homogeneous system such as a gas or a semiconductor the stimulated emission photons will all have the same wavelength and the emitted light will be monochromatic. Soon thereafter the photons emitted by stimulation

will stimulate emission of further photons. An avalanche effect will ensue and laser light will be emitted.

To have a beam of light and have the possibility for continuous wave (cw) operation, the other two parts of a laser must exist. These are a pump and a resonant cavity. If stimulated emission occurs in a population inversion the inversion will soon become depleted and the medium will return to an equilibrium state. If, however, an energy pump is used to continuously pump energy into the system the electrons that are emitting photons will regain the quanta of energy required to return to the higher energy level. The population inversion can then be maintained.

The third part of the laser, the resonant cavity, is what allows for cw operation and a strong pulse of light. Photon emission started at one end of the population inversion will quickly pass through the population inversion and exit the other side. While this is laser light it is a weak pulse. To get stronger light the photon emission must remain in a population inversion for a greater amount of time. There is a size limit to how big the population inversion can be made, especially in semiconductor lasers. To overcome this the population inversion is placed inside a resonant cavity. The light that is formed by the first pass through the population inversion passes back through the population inversion and the light grows stronger. To get light out of the cavity, one side is made less reflective than the other. Thus light is always being emitted from one end of the cavity while being strengthened inside the cavity.

Semiconductor lasers are used in fiber optic gyroscopes and on the AFIT MiG. Semiconductor lasers use a semiconductor diode to form the population inversion and pump. The resonant cavity is formed by one of two different means. The two main types

of semiconductor lasers are named for the way they form the resonant cavity. These are the edge emitting laser and the vertical cavity surface emitting laser (VCSEL). The edge-emitting laser uses two cleaved edges to form the mirrors of the resonant cavity.

VCSELs use Distributed Bragg Reflectors grown on top of the semiconductor to form the resonant cavity. As garnered from their names, the edge-emitting laser emits light from the edge of the device and the VCSEL emits light from the surface of the laser. The AFIT MiG utilizes edge-emitting lasers that emit from both edges.

Appendix C. AFIT MiG Equation

This Appendix contains the entire AFIT MiG equation for the non-reciprocal case. The appendix builds on what was presented in Chapter 3. The material of Chapter 3 will not be reproduced in this Appendix. Recall Equation (10), the reciprocal AFIT MiG equation:

$$L_1 R_1 \cos \theta_1 + L_2 R_1 \cos \theta_2 + L_3 R_2 \cos \theta_3 + L_4 R_2 \cos \theta_4 + L_5 R_3 \cos \theta_5 + L_6 R_3 \cos \theta_6 + L_7 R_4 \cos \theta_7 + L_8 R_4 \cos \theta_8 + L_9 R_5 \cos \theta_9 \quad (39)$$

When the clockwise and counterclockwise propagating optical paths are not the same length, referred to as non-reciprocities, this equation becomes:

$$\begin{aligned} & (L_1 + \delta L_1)(R_1 + \delta R_1) \cos(\theta_1 + \delta \theta_1) + (L_2 + \delta L_2)(R_1 + \delta R_1) \cos(\theta_2 + \delta \theta_2) + \\ & (L_3 + \delta L_3)(R_2 + \delta R_2) \cos(\theta_3 + \delta \theta_3) + (L_4 + \delta L_4)(R_2 + \delta R_2) \cos(\theta_4 + \delta \theta_4) + \\ & (L_5 + \delta L_5)(R_3 + \delta R_3) \cos(\theta_5 + \delta \theta_5) + (L_6 + \delta L_6)(R_3 + \delta R_3) \cos(\theta_6 + \delta \theta_6) + \\ & (L_7 + \delta L_7)(R_4 + \delta R_4) \cos(\theta_7 + \delta \theta_7) + (L_8 + \delta L_8)(R_4 + \delta R_4) \cos(\theta_8 + \delta \theta_8) + \\ & (L_9 + \delta L_9)(R_5 + \delta R_5) \cos(\theta_9 + \delta \theta_9) \end{aligned} \quad (40)$$

Using the trigonometric identity $\cos(A + B) = \cos A \cos B - \sin A \sin B$ along with the small angle approximation we can make the reduction for all terms:

$$\cos(\theta + \delta \theta) = \cos \theta - \delta \theta \sin \theta \quad (41)$$

Multiplying and collecting like terms along with using the above simplification yields:

$$\begin{aligned}
& (L_1 R_1 + L_1 \delta R_1 + \delta L_1 R_1 + \delta L_1 \delta R_1) (\cos \theta_1 - \delta \theta_1 \sin \theta_1) + \\
& (L_2 R_1 + L_2 \delta R_1 + \delta L_2 R_1 + \delta L_2 \delta R_1) (\cos \theta_2 - \delta \theta_2 \sin \theta_2) + \\
& (L_3 R_2 + L_3 \delta R_2 + \delta L_3 R_2 + \delta L_3 \delta R_2) (\cos \theta_3 - \delta \theta_3 \sin \theta_3) + \\
& (L_4 R_2 + L_4 \delta R_2 + \delta L_4 R_2 + \delta L_4 \delta R_2) (\cos \theta_4 - \delta \theta_4 \sin \theta_4) + \\
& (L_5 R_3 + L_5 \delta R_3 + \delta L_5 R_3 + \delta L_5 \delta R_3) (\cos \theta_5 - \delta \theta_5 \sin \theta_5) + \\
& (L_6 R_3 + L_6 \delta R_3 + \delta L_6 R_3 + \delta L_6 \delta R_3) (\cos \theta_6 - \delta \theta_6 \sin \theta_6) + \\
& (L_7 R_4 + L_7 \delta R_4 + \delta L_7 R_4 + \delta L_7 \delta R_4) (\cos \theta_7 - \delta \theta_7 \sin \theta_7) + \\
& (L_8 R_4 + L_8 \delta R_4 + \delta L_8 R_4 + \delta L_8 \delta R_4) (\cos \theta_8 - \delta \theta_8 \sin \theta_8) + \\
& (L_9 R_5 + L_9 \delta R_5 + \delta L_9 R_5 + \delta L_9 \delta R_5) (\cos \theta_9 - \delta \theta_9 \sin \theta_9)
\end{aligned} \tag{42}$$

Further multiplication and collecting of like terms yields:

$$\begin{aligned}
& L_1 R_1 \cos \theta_1 - L_1 R_1 \delta \theta_1 \sin \theta_1 + (L_1 \delta R_1 + \delta L_1 R_1 + \delta L_1 \delta R_1) (\cos \theta_1 - \delta \theta_1 \sin \theta_1) + \\
& L_2 R_1 \cos \theta_2 - L_2 R_1 \delta \theta_2 \sin \theta_2 + (L_2 \delta R_1 + \delta L_2 R_1 + \delta L_2 \delta R_1) (\cos \theta_2 - \delta \theta_2 \sin \theta_2) + \\
& L_3 R_2 \cos \theta_3 - L_3 R_2 \delta \theta_3 \sin \theta_3 + (L_3 \delta R_2 + \delta L_3 R_2 + \delta L_3 \delta R_2) (\cos \theta_3 - \delta \theta_3 \sin \theta_3) + \\
& L_4 R_2 \cos \theta_4 - L_4 R_2 \delta \theta_4 \sin \theta_4 + (L_4 \delta R_2 + \delta L_4 R_2 + \delta L_4 \delta R_2) (\cos \theta_4 - \delta \theta_4 \sin \theta_4) + \\
& L_5 R_3 \cos \theta_5 - L_5 R_3 \delta \theta_5 \sin \theta_5 + (L_5 \delta R_3 + \delta L_5 R_3 + \delta L_5 \delta R_3) (\cos \theta_5 - \delta \theta_5 \sin \theta_5) + \\
& L_6 R_3 \cos \theta_6 - L_6 R_3 \delta \theta_6 \sin \theta_6 + (L_6 \delta R_3 + \delta L_6 R_3 + \delta L_6 \delta R_3) (\cos \theta_6 - \delta \theta_6 \sin \theta_6) + \\
& L_7 R_4 \cos \theta_7 - L_7 R_4 \delta \theta_7 \sin \theta_7 + (L_7 \delta R_4 + \delta L_7 R_4 + \delta L_7 \delta R_4) (\cos \theta_7 - \delta \theta_7 \sin \theta_7) + \\
& L_8 R_4 \cos \theta_8 - L_8 R_4 \delta \theta_8 \sin \theta_8 + (L_8 \delta R_4 + \delta L_8 R_4 + \delta L_8 \delta R_4) (\cos \theta_8 - \delta \theta_8 \sin \theta_8) + \\
& L_9 R_5 \cos \theta_9 - L_9 R_5 \delta \theta_9 \sin \theta_9 + (L_9 \delta R_5 + \delta L_9 R_5 + \delta L_9 \delta R_5) (\cos \theta_9 - \delta \theta_9 \sin \theta_9)
\end{aligned} \tag{43}$$

Examining the first term from each of the rows in the above equation gives:

$$\begin{aligned}
& L_1 R_1 \cos \theta_1 + L_2 R_1 \cos \theta_2 + L_3 R_2 \cos \theta_3 + L_4 R_2 \cos \theta_4 + L_5 R_3 \cos \theta_5 + L_6 R_3 \cos \theta_6 \\
& + L_7 R_4 \cos \theta_7 + L_8 R_4 \cos \theta_8 + L_9 R_5 \cos \theta_9
\end{aligned} \tag{44}$$

This is equivalent to Equation 39 given above. The effect of non-reciprocal terms is to take the original scale factor and add to it further terms of the same type that are a function of the non-reciprocity.

The above derivation is for the AFIT MiG with only nine terms. The equation for n terms can be determined from the following:

$$\sum_{i=1}^n \left(\begin{array}{l} L_i R_{\text{floor}\left(\frac{i+1}{2}\right)} \cos i - L_i R_{\text{floor}\left(\frac{i+1}{2}\right)} \delta\theta_i \sin \theta_i + \\ \left(L_i \delta R_{\text{floor}\left(\frac{i+1}{2}\right)} + \delta L_i R_{\text{floor}\left(\frac{i+1}{2}\right)} + \delta L_i \delta R_{\text{floor}\left(\frac{i+1}{2}\right)} \right) (\cos \theta_i - \delta\theta_i \sin \theta_i) \end{array} \right) \quad (45)$$

In this equation the term floor refers to rounding down to the nearest whole number.

Appendix D. List of Acronyms

AFIT	Air Force Institute of Technology
CVD.....	Chemical Vapor Deposition
DARPA.....	Defense Advanced Research Projects Agency
ENU.....	East, North, Up
FOG	Fiber-Optic Gyroscope
I-FOG	Interferometric Fiber-Optic Gyroscope
IMU.....	Inertial Measurement Unit
INS.....	Inertial Navigation System
IORS.....	Integrated Optics Rotation Sensor
ISA	Inertial Sensor Assembly
LASER	Light Amplification by Stimulated Emission of Radiation
LIGA.....	Lithographie, Galvanoformung Abformung
MBE.....	Molecular Beam Epitaxy
MEMS.....	Micro Electro-Mechanical Systems
MIDOS.....	Modulated Integrative Differential Optical Sensing
MiG.....	MEMS Interferometric Gyroscope
MIT.....	Massachusetts Institute of Technology
MOSFET.....	Metal Oxide Semiconductor Field Effect Transistors
MOVPE.....	Metal-Organic Vapor-Phase Epitaxy
MUMPS.....	Multi-User MEMS Processes
R-FOG.....	Resonant Fiber-Optic Gyroscope
RLG.....	Ring Laser Gyroscope

SEEMS..... Step Electrochemical Etching for Micro Structures
STO..... Sensor Technology Office
VCSEL..... Vertical Cavity Surface Emitting Laser
WPAFB..... Wright-Patterson Air Force Base

Bibliography

- [1] Ayazi, Farrokh, and Khalil Najafi. Design and Fabrication of A High-Performance Polysilicon Vibrating Ring Gyroscope. Proceedings of the IEEE 1998.
- [2] Barbour, N., Connelly, J., Gilmore, J., Greif, P., Kourepenis, A., and M. Weinberg. Micromechanical Silicon Instrument and Systems Development at Draper Laboratory. AIAA Guidance, Navigation, and Control Conference San Diego CA, July 1996.
- [3] Barbour, Neil, and George Schmidt. Inertial Sensor Technology Trends. IEEE/OES AUV 98 Draper Laboratory MA, August 1998.
- [4] Bochobza-Degani, O., Seter, D. J., Socher, E., Kaldor, S., Scher, E., and Y. Neimirovsky. Comparative Study of Novel Micromachined Accelerometers Employing MIDOS. Proceedings of the IEEE 1999.
- [5] CADENCE Design Systems. CADENCE version 4.3, 1999.
- [6] Burns, William K. Optical Fiber Rotation Sensing. New York: Academic Press, Inc., 1993.
- [7] Fitzpatrick, Colleen and Michael P. Beraducci. Experimental Performance of The Prototype Integrated Optics Rotation Sensor. Proceedings of the 24th Joint Services Data Exchange for Guidance, Navigation and Control Symposium, Anaheim CA, 16-20 November 1996.
- [8] Funk, K., Emmerich, H., Schilp, A., Offenbergl, M., Neul, R., F. Larmer. A Surface Micromachined Silicon Gyroscope Using A Thick Polysilicon Layer. Proceedings of the IEEE 1999.
- [9] Geiger, W., Folkmer, B., Merz, J., Sandmaier, H., and W, Lang. A New Silicon Rate Gyroscope. Proceedings of the IEEE 1998.
- [10] Hartwell, P. G., Bertsch, F. M., Miller, S. A., Turner, K. L., and N. C. MacDonald. Single Mask Lateral Tunneling Accelerometer. Proceedings of the IEEE 1998.
- [11] Hecht, Eugene. Optics, 2nd ed. Wesley: Reading, 1987.
- [12] Hitz, Breck. Understanding Laser Technology. PenWell: Oklahoma, 1985.
- [13] Hulsing, Rand. MEMS Inertial Rate and Acceleration Sensor. IEEE AES Systems Magazine, November 1998.

- [14] Kaspar, Beth M. Lt. Col. The DARPA Micro-Electro Mechanical Sensor (MEMS) Inertial Navigation System (INS) Program. Defense Advanced Research Projects Agency, Sensor Technology Office, 1999.
- [15] Kaplan, Marshall H. Modern Spacecraft Dynamics and Control. Wiley: New York, 1976.
- [16] Klass, Philip J. Tiny Inertial Sensors Made on Silicon Chips. Aviation Week and Space Technology. August 10, 1998.
- [17] Knudson, A. R., Buchner, S., McDonald, P., Stapor, W. J., Campbell, A. B., Grabowski, K. S., Knies, D. L., Lewis, S. and Y. Zhao. The Effects of Radiation on MEMS Accelerometers. IEEE Transactions on Nuclear Science December 1998.
- [18] Koester, David A., Mahadevan, Ramaswamy, Shishkoff, Ales, and Karen W. Markus. MUMPS™ Design Handbook. Rev 4. <http://www.mcnc.org>.
- [19] Kourepenis, A., Borenstein, J., Connelly, J., Elliot, R., Ward, P., and M. Weinberg. Performance of MEMS Inertial Sensors. 24th Joint Services Data Exchange Conference, Anaheim CA, November 1998.
- [20] Kovacs, Gregory T. A. Micromachined Transducers Sourcebook. New York: McGraw Hill, 1998.
- [21] Kruglick, E. J. J., Warneke, B. A., and K. S. J. Pister. CMOS 3-Axis Accelerometers With Integrated Amplifier. Proceedings of the IEEE 1998.
- [22] Lee, C. I, Johnston, A. H. Tang, W. C. Barnes, C. E. and j. Lyke. Total Dose Effects on Microelectromechanical Systems (MEMS): Accelerometers. IEEE Transactions on Nuclear Science December 1998.
- [23] Lefevre, Herve. The Fiber-Optic Gyroscope. Norwood: Artech House, Inc., 1993.
- [24] Leung, A. M., Jones, J., Czyzewska, E., Chen, J., and B. Woods. Micromachined Accelerometers Based on Convection Heat Transfer. Proceedings of the IEEE 1998.
- [25] Math Works Inc, The. MATLAB The Language of Technical Computing. Version 5. The Math Works Inc, 1999.
- [26] McKelvey, John P. Solid State Physics For Engineering and Materials Science. Krieger: Malabar, 1993.

- [27] Oh, Yongsoo, Lee, Byeungleul, Baek, Seogsoon, Kim, Hosuk, Kim, Jeonggon, Kang, Seokjin, and Cimoo Song. A Surface Micromachined Tunable Vibratory Gyroscope. Proceedings of the IEEE 1998.
- [28] Ohji, H., Gennissen, P. T. J., French, P. J., and K. Tsutsumi. Fabrication of Accelerometer Using Single-Step Electrochemical Etching For Micro Structures (SEEMS). Proceedings of the IEEE 1999.
- [29] Park, K. Y., Lee, C. W., Jang, H. S., Oh, Y. S., and B. J. Ha. Capacitive Sensing Type Surface Micromachined Silicon Accelerometer With a Stiffness Tuning Capability. Proceedings of the IEEE 1998.
- [30] Park, K. Y., Lee, C. W., Oh, Y. S., and Y. H. Cho. Laterally Oscillated and Force-Balanced Micro Vibratory Rate Gyroscope Supported By Fish Hook Shaped Springs. Proceedings of the IEEE 1997.
- [31] Sandia National Laboratories. MEMS Overview.
<http://www.mdl.sandia.gov/micromachine/overview.html>
- [32] Sze, S. M. Semiconductor Devices Physics and Technology. Wiley: New York, 1985.
- [33] Valoff, Scott, and William J. Kaiser. Presettable Micromachined MEMS Accelerometers. Proceedings of the IEEE 1999.
- [34] Williams, Kirt R. and Richard S. Muller. "Etch Rates for Micromachining Processing." Journal of Microelectromechanical Systems. 4, December 1996.
- [35] Yazdi, Navid, Ayazi, Farrokh, and Khalil Najafi. Micromachined Inertial Sensors. Proceedings of the IEEE August 1998.
- [36] Yee, Y., Park, M., Lee, S.H., Lee, S., Chun, K., Kim, Y. K., and D. D. Cho. MAMOS-A Novel Displacement Sensitive Transducer for Fully Digital Integrated Accelerometer. Proceedings of the IEEE 1998.

REPORT DOCUMENTATION PAGE

Form Approved
OMB No. 0704-0188

The public reporting burden for this collection of information is estimated to average 1 hour per response, including the time for reviewing instructions, searching existing data sources, gathering and maintaining the data needed, and completing and reviewing the collection of information. Send comments regarding this burden estimate or any other aspect of this collection of information, including suggestions for reducing the burden, to Department of Defense, Washington Headquarters Services, Directorate for Information Operations and Reports (0704-0188), 1215 Jefferson Davis Highway, Suite 1204, Arlington, VA 22202-4302. Respondents should be aware that notwithstanding any other provision of law, no person shall be subject to any penalty for failing to comply with a collection of information if it does not display a currently valid OMB control number.

PLEASE DO NOT RETURN YOUR FORM TO THE ABOVE ADDRESS.

1. REPORT DATE (DD-MM-YYYY) 21-03-2000	2. REPORT TYPE Master's Thesis	3. DATES COVERED (From - To) October 1999 - March 2000
---	-----------------------------------	---

4. TITLE AND SUBTITLE THE AIR FORCE INSTITUTE OF TECHNOLOGY (AFIT) MICRO ELECTRO-MECHANICAL SYSTEMS (MEMS) INTERFEROMETRIC GYROSCOPE (MiG)	5a. CONTRACT NUMBER
	5b. GRANT NUMBER
	5c. PROGRAM ELEMENT NUMBER

6. AUTHOR(S) Jeremy P. Stringer, 2Lt, USAF	5d. PROJECT NUMBER
	5e. TASK NUMBER
	5f. WORK UNIT NUMBER

7. PERFORMING ORGANIZATION NAME(S) AND ADDRESS(ES) Air Force Institute of Technology 2950 P Street Wright-Patterson AFB, OH 45433-7765	8. PERFORMING ORGANIZATION REPORT NUMBER AFIT/GE/ENG/00M-18
---	--

9. SPONSORING/MONITORING AGENCY NAME(S) AND ADDRESS(ES) Mr. James D. Leonard AFRL/SNAR 2241 Avionics Circle (Bldg. 620) Rm. N3-X19 Wright-Patterson AFB, OH 45433 (937) 785-5668, ext. 4137	10. SPONSOR/MONITOR'S ACRONYM(S) AFRL/SNAR
	11. SPONSOR/MONITOR'S REPORT NUMBER(S)

12. DISTRIBUTION/AVAILABILITY STATEMENT
Approved for public release; distribution unlimited

13. SUPPLEMENTARY NOTES

14. ABSTRACT
To try to increase the accuracy of micro-inertial sensors, researchers are turning toward micro-optical gyroscopes. Creating a working micro-optical gyroscope is a difficult proposition as their small size precludes micro-optical gyroscopes from having large enough optical path lengths to sense useful rotation rates. Techniques need to be developed to create micro-optical gyroscopes with optical path lengths long enough to sense navigation grade rotation rates.
This research proposes a new type of MEMS optical gyroscope. The device, called the AFIT MiG, is an open loop Sagnac interferometer on a MEMS die. Mirrors are placed on the die to spiral light inward from the outside to the center of the die, thereby increasing the optical pathlength of the device. When the AFIT MiG was simulated using flight profiles generated in MATLAB(TM), the optical path length of the device was sufficient to sense usable rotation rates, which were greater in strength than the noise inherent in the measurement.
The impact of this research is that it creates a new way to create a micro-optical gyroscope. Further research along this topic could produce a working micro-optical gyroscope capable of providing navigation quality measurements.

15. SUBJECT TERMS
INS, Inertial Navigation System, MEMS, Optical Gyroscope

16. SECURITY CLASSIFICATION OF:			17. LIMITATION OF ABSTRACT SAR	18. NUMBER OF PAGES 160	19a. NAME OF RESPONSIBLE PERSON Mikel M. Miller, Lt Col, USAF
a. REPORT U	b. ABSTRACT U	c. THIS PAGE U			19b. TELEPHONE NUMBER (Include area code) (937) 255-6565, ext. 4278